

# **PLASMON-INDUCED PLASMA SPECTROSCOPY**

**Terefe G. Habteyes, et al.**

**University of New Mexico  
Center for High Technology Materials  
1313 Goddard Street SE  
Albuquerque, NM 87106**

**10 November 2016**

**Final Report**

**APPROVED FOR PUBLIC RELEASE; DISTRIBUTION IS UNLIMITED.**



**AIR FORCE RESEARCH LABORATORY  
Space Vehicles Directorate  
3550 Aberdeen Ave SE  
AIR FORCE MATERIEL COMMAND  
KIRTLAND AIR FORCE BASE, NM 87117-5776**

## DTIC COPY

### NOTICE AND SIGNATURE PAGE

Using Government drawings, specifications, or other data included in this document for any purpose other than Government procurement does not in any way obligate the U.S. Government. The fact that the Government formulated or supplied the drawings, specifications, or other data does not license the holder or any other person or corporation; or convey any rights or permission to manufacture, use, or sell any patented invention that may relate to them.

This report is the result of contracted fundamental research which is exempt from public affairs security and policy review in accordance with AFI 61-201, paragraph 2.3.5.1. This report is available to the general public, including foreign nationals. Copies may be obtained from the Defense Technical Information Center (DTIC) (<http://www.dtic.mil>).

AFRL-RV-PS-TR-2017-0185 HAS BEEN REVIEWED AND IS APPROVED FOR PUBLICATION IN ACCORDANCE WITH ASSIGNED DISTRIBUTION STATEMENT.

//SIGNED//

---

Dr. Christopher Annesley  
Program Manager, AFRL/RVBYC

//SIGNED//

---

Dr. Thomas R. Caudill, Acting Chief  
AFRL Battlespace Environment Division

This report is published in the interest of scientific and technical information exchange, and its publication does not constitute the Government's approval or disapproval of its ideas or findings.

| REPORT DOCUMENTATION PAGE   |                             |                                |   | Form Approved<br>OMB No. 0704-0188                                |   |
|---|-----------------------------|--------------------------------|---|---|---|
| Public reporting burden for this collection of information is estimated to average 1 hour per response, including the time for reviewing instructions, searching existing data sources, gathering and maintaining the data needed, and completing and reviewing this collection of information. Send comments regarding this burden estimate or any other aspect of this collection of information, including suggestions for reducing this burden to Department of Defense, Washington Headquarters Services, Directorate for Information Operations and Reports (0704-0188), 1215 Jefferson Davis Highway, Suite 1204, Arlington, VA 22202-4302. Respondents should be aware that notwithstanding any other provision of law, no person shall be subject to any penalty for failing to comply with a collection of information if it does not display a currently valid OMB control number. <b>PLEASE DO NOT RETURN YOUR FORM TO THE ABOVE ADDRESS.</b> |                             |                                |   |   |   |
| 1. REPORT DATE (DD-MM-YYYY)<br>10-11-2016   |                             | 2. REPORT TYPE<br>Final Report |   | 3. DATES COVERED (From - To)<br>31 Jul 2015 – 10 Aug 2016         |   |
| 4. TITLE AND SUBTITLE<br>Plasmon-Induced Plasma Spectroscopy  |                             |                                |   | 5a. CONTRACT NUMBER<br>FA9453-15-1-0078                           |   |
|   |                             |                                |   | 5b. GRANT NUMBER  |   |
|   |                             |                                |   | 5c. PROGRAM ELEMENT NUMBER<br>62601F                              |   |
| 6. AUTHOR(S)<br>Terefe G. Habteyes, Bijesh Kafle, Tefera E. Tesema, Sharmin Haq, Meron Tadesse, Marisa Poveda, and Claudia Rivera Lebron  |                             |                                |   | 5d. PROJECT NUMBER<br>5018  |   |
|   |                             |                                |   | 5e. TASK NUMBER<br>PPM00035401                                    |   |
|   |                             |                                |   | 5f. WORK UNIT NUMBER<br>EF129612                                  |   |
| 7. PERFORMING ORGANIZATION NAME(S) AND ADDRESS(ES)<br>University of New Mexico<br>Center for High Technology Materials<br>1313 Goddard Street SE<br>Albuquerque, NM 87106   |                             |                                |   | 8. PERFORMING ORGANIZATION REPORT NUMBER                          |   |
| 9. SPONSORING / MONITORING AGENCY NAME(S) AND ADDRESS(ES)<br>Air Force Research Laboratory<br>Space Vehicles Directorate<br>3550 Aberdeen Avenue SE<br>Kirtland AFB, NM 87117-5776  |                             |                                |   | 10. SPONSOR/MONITOR'S ACRONYM(S)<br>AFRL/RVBYC                    |   |
|   |                             |                                |   | 11. SPONSOR/MONITOR'S REPORT NUMBER(S)<br>AFRL-RV-PS-TR-2017-0185 |   |
| 12. DISTRIBUTION / AVAILABILITY STATEMENT<br>Approved for public release; distribution is unlimited.  |                             |                                |   |   |   |
| 13. SUPPLEMENTARY NOTES   |                             |                                |   |   |   |
| 14. ABSTRACT<br>Foundational works that may pave the way for utilizing localized surface plasmon resonances for plasma generation have been carried out. Super-resolved vibrational imaging of thin films has been demonstrated. A far-field microscope that allows correlated dark-field scattering and surface enhanced Raman scattering measurements have been developed. Using methylene blue as model molecular system, chemical transformation induced by plasmon enhanced resonant excitation of adsorbates has been reported for the first time. Surface enhanced Raman scattering spectroscopy reveals that methylene blue is transformed to thionine through plasmon driven demethylation reaction.   |                             |                                |   |   |   |
| 15. SUBJECT TERMS<br>Surface plasmon driven chemical processes  |                             |                                |   |   |   |
| 16. SECURITY CLASSIFICATION OF:   |                             |                                | 17. LIMITATION OF ABSTRACT<br><br>Unlimited | 18. NUMBER OF PAGES<br><br>50                                     | 19a. NAME OF RESPONSIBLE PERSON<br>Dr. Christopher Annesley |
| a. REPORT<br>Unclassified   | b. ABSTRACT<br>Unclassified | c. THIS PAGE<br>Unclassified   |   |   | 19b. TELEPHONE NUMBER (include area code)                   |

This page is intentionally left blank.

|   |     |
|---|-----|
| List of Figures.....  | ii  |
| Abstract .....  | iii |
| Acknowledgments and Disclaimer.....   | iv  |
| 1. Introduction .....   | 1   |
| 2. Results .....  | 2   |
| 2.1 Demonstration of super-resolution vibrational imaging.....                          | 2   |
| 2.2 Correlated dark-field scattering and SERS spectroscopy.....                         | 3   |
| 2.3 Plasmon enhanced resonant excitation and chemical transformation.....               | 4   |
| 2.3.1 Direct excitation of adsorbate states.....  | 6   |
| 2.3.2 Experimental observations and proposed mechanism.....                             | 7   |
| 2.3.2.1 Excitation of MB and plasmon resonances leads to demethylation.....             | 7   |
| 2.3.2.2 Excitation of plasmon resonances but not MB does not lead to demethylation..... | 7   |
| 2.3.2.3 Excitation of MB on non-plasmonic surfaces does not lead to demethylation.....  | 8   |
| 2.3.2.4 The reaction mechanism may involve singlet oxygen....                           | 8   |
| 3. Summary .....  | 9   |
| References .....  | 10  |
| Appendix: Published articles .....  | 13  |
| List of Abbreviations.....  | 41  |

## List of Figures

|                 |  |   |
|-----------------|--|---|
| <b>Figure 1</b> | Apertureless near-field scanning optical microscope experimental setup.....  | 2 |
| <b>Figure 2</b> | Simultaneously recorded topography, infrared optical amplitude and optical phase images of PMMA on silicon wafer .....                                 | 3 |
| <b>Figure 3</b> | Schematic showing excitation and detection layout for elastic (dark-field scattering) and inelastic (Raman scattering) measurements.....               | 4 |
| <b>Figure 4</b> | Temporal evolution of SERS spectra of resonantly excited MB on resonantly excited plasmonic AuNRs.....   | 5 |
| <b>Figure 5</b> | Comparison of (a) Stokes and (b) anti-Stokes Raman intensities of the $449\text{ cm}^{-1}$ band...   | 6 |
| <b>Figure 6</b> | Illustration of the importance of excitation energy overlap with the electronic transition of the molecule for the surface reaction to take place..... | 7 |
| <b>Figure 7</b> | Raman spectra of MB adsorbed on gold film in the absence of plasmonic nanoparticles.....   | 8 |
| <b>Figure 8</b> | Energy diagram of methylene blue.....  | 8 |

## Abstract

Foundational works that may pave the way for utilizing localized surface plasmon resonances for plasma generation have been carried out. Super-resolved vibrational imaging of thin films has been demonstrated. A far-field microscope that allows correlated dark-field scattering and surface enhanced Raman scattering measurements have been developed. Using methylene blue as model molecular system, chemical transformation induced by plasmon enhanced resonant excitation of adsorbates has been reported for the first time. Surface enhanced Raman scattering spectroscopy reveals that methylene blue is transformed to thionine through plasmon driven demethylation reaction. The experimental results suggest that singlet oxygen is involved in the reaction. The involvement of singlet oxygen may have implications in many other plasmon driven chemical processes. The initial results have stimulated new research directions for the coming several years in collaboration with scientists at the Air Force Research Lab, Kirtland Air Force Base, to detect gaseous products, and ultimately plasma formation. Three research articles have been published. Three graduate students and three female undergraduate students have been participating in this research project. The majority of the students are from historically under represented group of society.

## **ACKNOWLEDGMENTS**

This material is based on research sponsored by the Air Force Research Laboratory under agreement number FA9453-15-1-0078. The U.S. Government is authorized to reproduce and distribute reprints for Governmental purposes notwithstanding any copyright notation thereon.

## **DISCLAIMER**

The views and conclusions contained herein are those of the authors and should not be interpreted as necessarily representing the official policies or endorsements, either expressed or implied, of the Air Force Research Laboratory or the U.S. Government.

## 1. Introduction

The generation of plasma from condensed and gaseous phase target materials have been intensively investigated using pulsed lasers with nanosecond ( $10^{-9}$  second) to femtosecond ( $10^{-15}$  second) pulse durations.<sup>1-3</sup> Laser ablation (LA) and laser-induced breakdown spectroscopy (LIBS) are notable processes that involve plasma generation using pulsed laser sources. LA and LIBS have attracted considerable research interest because of applications in materials identification and the fundamental chemistry and physics involved in the process.<sup>4, 5</sup> For example, matrix-assisted laser desorption and ionization (MALDI) is a well-established technique for identification and quantification of molecular solids by analyzing the ionized species using mass spectrometry.<sup>6</sup> LIBS has now become a powerful analytical tool for analysis of materials including on the surface of Mars.<sup>3</sup>

Plasma formation involves ionization of atomic and molecular species that require high laser power ( $>10^8$  W/cm<sup>2</sup>), which is easily attained when nanosecond and shorter pulses are used. As a result, plasma studies to date have been based on pulsed laser sources, which are usually bulky and expensive. The near-field properties of localized surface plasmon resonances may be used to generate plasma using low irradiance of continuous wave (CW) lasers. For example, there have been attempts in the past to enhance high harmonic generation (that involves high field ionization) using plasmonic nanoantennas<sup>7</sup> but the possibility of generating plasma using CW laser sources remains unexplored. In addition, in the past studies, analysis of the photochemical reactions is lacking and the generation of high harmonic signals has been debated.<sup>8</sup>

In this project, we have carried out foundational experiments that have provided important insight into surface plasmon driven surface photochemical processes. Significant technical advances in optical measurements have been achieved. Chemical mapping using super-resolution near-field scanning optical microscopy has been demonstrated. A far-field microscope for correlated dark-field scattering and surface enhanced Raman scattering (SERS) spectroscopic measurements has been developed. Self-assemblies of plasmonic nanoparticles on different substrates have been tested to achieve maximum enhancement of Raman scattering. Using methylene blue (MB) as a model system, we have demonstrated surface plasmon enhanced resonant excitation that leads to N-demethylation reaction under visible light irradiation ( $\lambda = 633$  nm) at low photon flux. The chemical changes are monitored by detecting the vibrational signatures of the reactant and product species in situ using SERS spectroscopy. Drastic temporal evolution of SERS spectra has been observed upon continuous irradiation. While the SERS spectra acquired immediately after irradiation are the same as the Raman spectrum of MB solid powder, the spectra recorded a few seconds later are remarkably similar to that of thionine solid powder, indicating N-demethylation of MB. No demethylation reaction has been observed under resonant excitation ( $\lambda = 633$  nm) of MB adsorbed on non-plasmonic surfaces. Similarly, excitations of plasmon resonances at 532 and 808 nm wavelengths that do not overlap with the MB electronic transition do not lead to transformation of MB to thionine. The reaction mechanism is discussed in terms of resonant excitation of MB and hot electron transfer to adsorbed species. Considering that both MB and thionine have large SERS signal due to the

combination of resonance Raman and electromagnetic enhancement effects that provide high detection sensitivity, the demethylation reaction will likely serve as a convenient model system for future mechanistic studies.

## 2. Results

### 2.1 Demonstration of super-resolution vibrational imaging

Understanding surface chemistry is a longstanding grand challenge with tremendous impact in heterogeneous catalysis and other industrial applications. Plasmon induced surface chemical process is not an exception of this challenge. Understanding these surface processes require detection of species adsorbed on the solid surface and the species gas phase desorbing from the surface. Apertureless near-field scanning optical microscope (ANSOM) (**Figure 1**) allows us to map the topography and vibrational fingerprints of the material simultaneously with the resolution of atomic force microscope (AFM). To this end, we have installed tunable infrared laser, the output which can be tuned to match the vibrational frequency of a specific chemical bond and obtain chemical contrast as demonstrated in **Figure 2**.

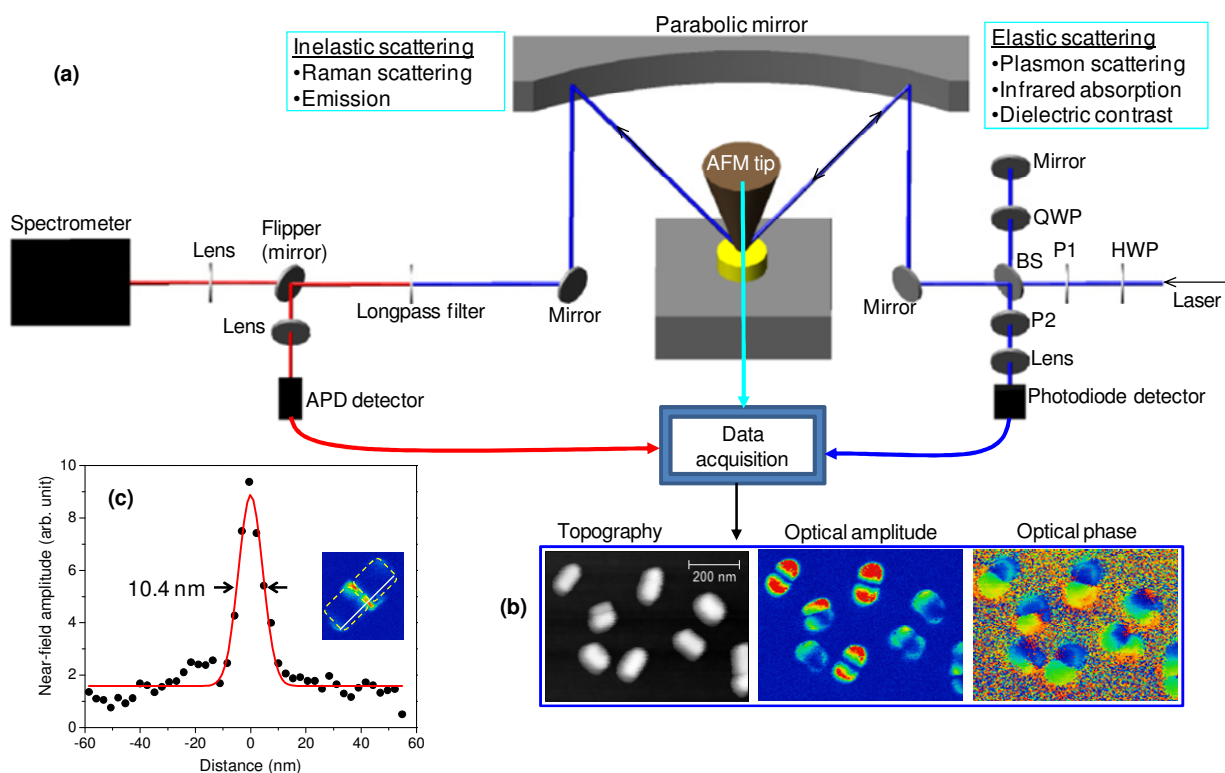


**Figure 1** Apertureless near-field scanning optical microscope experimental setup. (a) Schematics of our ANSOM setup. Linearly polarized laser light is focused at the AFM tip-sample interface using a parabolic mirror. The broadband parabolic mirror collects the scattered light through the right (elastic scattering) and left (inelastic scattering) channels. (b) Simultaneously recorded topography, optical amplitude and optical phase images of gold nanorods obtained at 633 nm excitation wavelength. (c) Optical image plasmon gap mode of coupled gold nanobars, demonstrating optical resolution on the order of 10 nm. Vibrational imaging is accomplished with same optical resolution by using near-infrared laser. Inelastic scattering can be detected simultaneously using single photon counting avalanche photodiode detector (APD). Spectra are recorded by directing the scattered light into the spectrometer. BS  $\equiv$  beamsplitter, P1, P2  $\equiv$  polarizers 1, 2 and HWP, QWP  $\equiv$  half, quarter waveplates.

The mid-infrared quantum cascade laser (QCL, Daylight Solutions Inc.) is broadly tunable with  $\sim 0.1 \text{ cm}^{-1}$  accuracy in important spectral regions covering the carbonyl vibrational frequencies as well as the carbon-oxygen and carbon-nitrogen single bond stretching frequencies. For demonstrating the optical contrast mechanism and sensitivity of the infrared near-field optical imaging technique, we have prepared a poly(methyl methacrylate) (PMMA) film that has thickness variation across the silicon-PMMA boundary and the results obtained at excitation laser line close to the C=O stretching frequency of the carbonyl group of the PMMA are presented in **Figure 2**. Comparing the topographic and optical images as well as the corresponding line profiles, it can be seen that as we cross from bare Si substrate to the PMMA film, (i) the optical amplitude and phase start to decrease and increase, respectively, immediately after the Si surface is covered with very thin film of PMMA, and (ii) the minimum and maximum of the optical amplitude and phase, respectively, coincides with the maximum thickness observed in the topography. In addition, the infrared absorption properties of residual islands of PMMA on Si wafer are discernible on the left portion of the optical amplitude and phase images. The observed optical amplitude and phase contrast is consistent with the resonance and dielectric properties of the vibrational absorptions and it is this principle that will be utilized in the identification of chemical changes by probing the target materials.

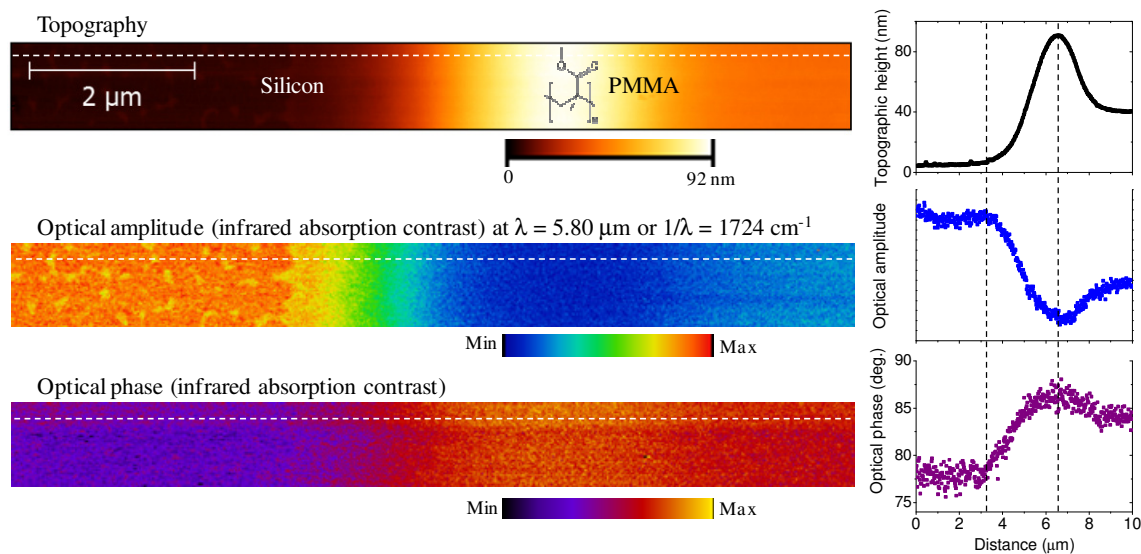


**Figure 2** Simultaneously recorded topography, infrared optical amplitude and optical phase images of PMMA on silicon wafer. Simultaneously recorded topography, infrared optical amplitude and optical phase along with the lineprofiles (across the dash lines drawn on the images) plotted on the right side of the corresponding images. The optical images are obtained at laser line  $1724 \text{ cm}^{-1}$  that is close to the resonance frequency of C=O double bond stretching vibrations of the carbonyl group of poly(methyl methacrylate) (PMMA).

## 2.2 Correlated dark-field scattering and SERS spectroscopy

Considering that plasmon resonance energies are extremely sensitive to their surrounding chemical interfaces, determining the resonances of the plasmonic nanostructures as they are assembled on the SERS substrate is critical to understand and optimize surface chemical processes. To this end, our optical microscope is customized for correlated plasmon resonance

and SERS measurements on any substrate regardless of transparency.<sup>9, 10</sup> Sequential detection of the dark-field scattering and SERS using the same objective (0.9 NA, 100x) is achieved by modifying the GX51F5 Olympus microscope as shown in the schematic in **Figure 3**. For the dark-field scattering measurement, the sample is excited with 100 W halogen white light source. For SERS experiments, the samples are excited with laser lines. More than 90% of the light collected from the sample through the objective is directed to the spectrometer (IsoPlane Spectrograph of Princeton Instruments) that uses a thermoelectrically cooled (-75 °C) and back-illuminated deep depletion CCD camera, while the remaining signal is directed to the Olympus UC30 camera that is attached to the microscope for imaging the dark-field scattering of the sample. The dark-field scattering (bottom-left corner in **Figure 3**) and SERS (top-right corner in **Figure 3**) from the same area are recorded simply by switching the excitation source from the white light to the laser line, while all the optical components and the sample remain stationary.

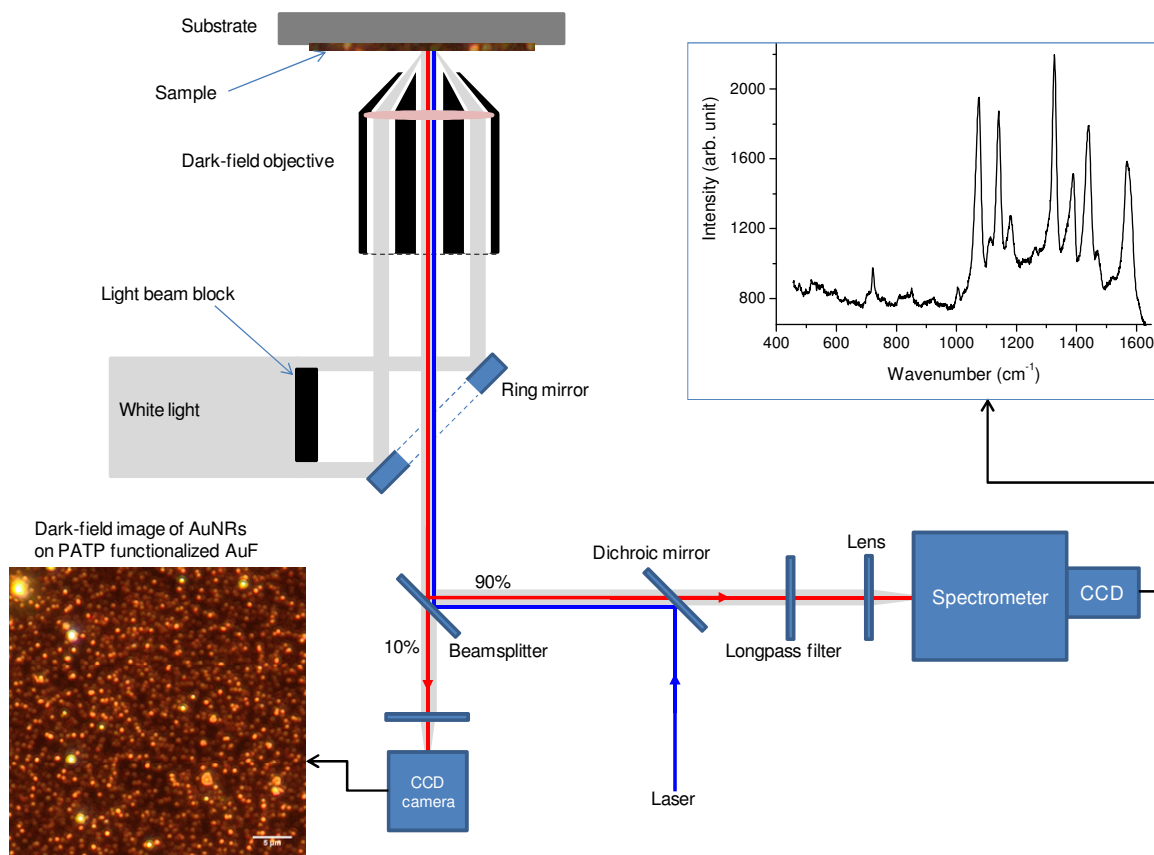


**Figure 3** Schematic showing excitation and detection layout for elastic (dark-field scattering) and inelastic (Raman scattering) measurements. The dark-field image of AuNRs AuF is shown at the bottom-left corner, and the corresponding example SERS spectrum is shown on the top-right corner.

### 2.3 Plasmon enhanced resonant excitation and chemical transformation

Surface enhanced photochemistry was proposed theoretically<sup>11, 12</sup> and demonstrated experimentally<sup>13-19</sup> soon after the discovery of SERS.<sup>20, 21</sup> Examples of plasmon-driven photochemical reactions include decomposition of organic molecules,<sup>16, 18, 22</sup> oxidative azo-

coupling of self-assembled para-aminothiophenol,<sup>9, 23-27</sup> dissociation of hydrogen molecules,<sup>28</sup> conversion of aldehydes to esters,<sup>29</sup> and demethylation of methylene blue,<sup>10</sup> all at room temperature. However, the mechanism of plasmon driven photochemistry remains poorly understood. Although hot plasmon electron transfer to adsorbed species has been proposed as an important step in plasmon driven reaction,<sup>28, 30</sup> determining the chemical identity and electronic state of reactive intermediates is a grand challenge. In addition to hot electron transfer, the surface chemistry can also be induced by electronic excitation of the adsorbate, plasmon heating and surface-molecule interaction, and all of these processes can be interdependent. Systematic study of this complicated surface chemistry can be facilitated by choosing a good model system that is convenient to monitor the progress of the reaction in situ. In particular, reactant and product species with large Raman scattering cross-section provides a convenient platform for probing the reaction in situ using SERS as a sensitive vibrational spectroscopy.

To this end, we have been investigating the photochemistry of methylene blue (MB), and the preliminary results indicate that MB can be used as an excellent model system for mechanistic studies of plasmon driven photochemical processes. The experiment was initiated using 633 nm excitation wavelength by adsorbing MB on plasmonic gold nanorods (AuNRs). The excitation wavelength overlaps with both the electronic transition energy of MB and the plasmon resonance of the AuNRs. Under continuous illumination of the MB-AuNR sample, the SERS spectra evolve as a function of time as shown in **Figures 4a**. That is, new vibrational bands have appeared a few seconds after the excitation laser is turned on as indicated by the vertical dashed lines in **Figure 4a**. The SERS spectrum acquired immediately after illumination (blue line) is the same as the normal Raman spectrum of MB solid powder (black line). On the other hand, the SERS spectra acquired a few seconds after illumination (red line) are similar to the normal Raman spectrum of thionine solid powder (green line). In particular, the peak at 479  $\text{cm}^{-1}$  that is the most intense in the red spectrum is completely absent in the Raman spectrum of MB. Similarly, the peak at 804  $\text{cm}^{-1}$  is attributed to  $\text{NH}_2$  rocking vibration of thionine, and cannot be assigned to MB. The evolution of the spectra is attributed to plasmon driven N-demethylation reaction that transforms MB to thionine as illustrated in **Figure 2b**.

We have recently published the first observation of this demethylation reaction.<sup>10</sup> However, the detail of the mechanism is yet to be explored. The reaction is convenient for systematic

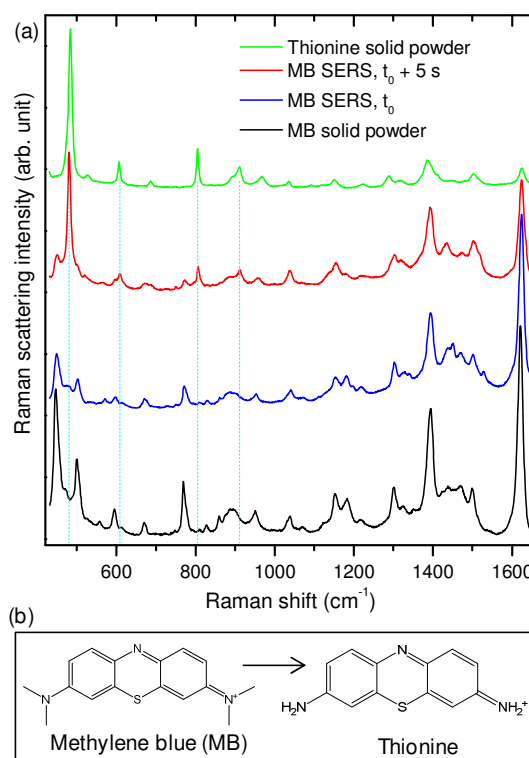


**Figure 4. Temporal evolution of SERS spectra of resonantly excited MB on resonantly excited plasmonic AuNRs.** (a) Representative SERS spectra of MB recorded at the time delays indicated on the plot ( $t_0 \approx 0.5$  s, acquisition time of a single spectrum) compared to the normal Raman spectra of MB (black line) and thionine (green line) solid powders. (b) Proposed chemical transformation responsible for the spectral evolution.

mechanistic studies because both MB and thionine have large Raman scattering signals due to the combination of electromagnetic and resonance enhancement effects in the visible spectral region.<sup>31</sup> As a result, the progress of the reaction can be monitored in situ with high sensitivity using SERS. In the following sections, the plausibility of different mechanisms is rationalized and the involvement of singlet oxygen is hypothesized based on experimental observations and experiments that are relevant to test the hypothesis are proposed.

### 2.3.1 Direct excitation of adsorbate states

Based on excitation wavelength dependent anti-Stokes to Stokes Raman intensity ratio, Linic and co-workers have proposed direct charge excitation in MB adsorbate, where the plasmon electron is directly promoted to unoccupied orbital in the surface-molecule complex.<sup>32, 33</sup> Anti-Stokes to Stokes Raman intensity ratio as high as 34 has been observed at  $\lambda = 785$  nm excitation wavelength, while the ratio is less than one at  $\lambda = 532$  nm.<sup>32</sup> Since none of these excitation wavelengths overlap with the electronic transition energy of MB, the observation of higher anti-Stokes to Stokes intensity ratio at 785 nm has been attributed to resonant excitation of adsorbate states that may have significantly different transition energy from isolated MB molecule.<sup>32, 33</sup> This interpretation is based on an assumption that electron transfer can increase the population of excited vibrational energy level, and it is open for debate. More importantly, no chemical transformation of MB has been observed in the experiments by Linic and co-workers.<sup>32, 33</sup> This indicates that even if there is direct electron injection into the unoccupied adsorbate state, it does not initiate chemical reaction. It should also be noted that the electronic absorption band of MB on surfaces can appear anywhere between 500 nm and 800 nm depending on the cluster size of MB (monomer, dimer, trimer, etc)<sup>34-36</sup> that has to be controlled through careful sample preparation to achieve adsorption of monomers as opposed to aggregates.

We have compared the Stokes and anti-Stokes Raman scattering intensities at 633 nm excitation wavelength as shown in the intensity map of representative vibrational bands of the MB reactant and thionine product signals in **Figure 5**. Clearly, the anti-Stokes to Stokes Raman intensity remains very small and constant during the continuous illumination and acquisition of data for over 200 seconds as shown in **Figure 5c**. This observation confirms that the type of charge excitation proposed by Linic and coworkers has no role in the plasmon N-demethylation of MB.

Experimental observations and theoretical calculations indicate that MB is weakly adsorbed on gold and silver surfaces. Comparing the blue and black spectra in **Figure 4a**, it can be seen that the vibrational frequencies of MB adsorbed on gold surface and regular Raman spectrum of MB solid powder agree within  $\pm 3$   $\text{cm}^{-1}$ . This negligible vibrational frequency shift is characteristic of weak surface-molecule physical interaction.<sup>37</sup> We have also verified that the absorption spectrum of MB adsorbed on gold surface is slightly blue-shifted and broadened

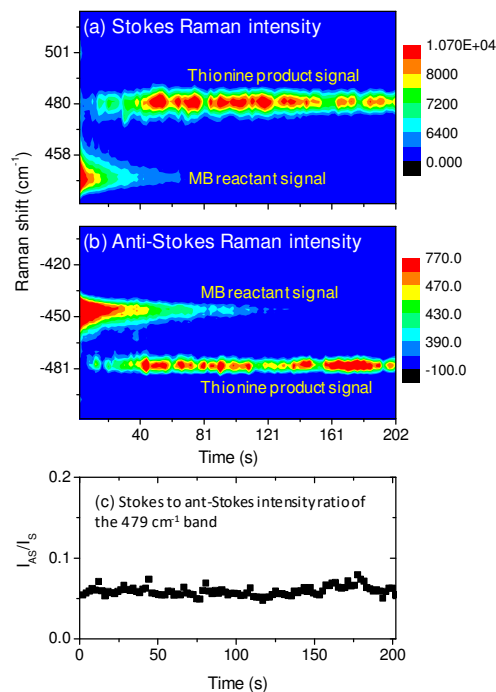


**Figure 5.** Comparison of (a) Stokes and (b) anti-Stokes Raman intensities of the 449  $\text{cm}^{-1}$  band. (c) Stokes to anti-Stokes intensity ratio plotted as a function of time.

compared to the solution phase absorption spectrum but no new bands are observed. Consistent with these experimental observations, recent theoretical calculations by Hua Guo and co-workers<sup>38</sup> show that the adsorption of MB on gold and silver surfaces has little impact on the geometry of MB. The theoretical work also shows that the frontier orbitals of MB on gold surface remains distinct despite some broadening due to the interaction with the metal surface. The center positions of the lowest unoccupied molecular orbital and highest occupied molecular orbital energies of MB are only slightly shifted from the gas phase values. It is well known from extensive studies of chemical enhancement mechanism of SERS that metal to molecule and vice versa charge transfer takes place when the analyte molecules are adsorbed to the surface strongly through chemical interactions, which clearly is not the case for MB.

### 2.3.2 Experimental observations and proposed mechanism

In order to narrow down the possible mechanism for the observed N-demethylation reaction and propose validating experiments, we have tested the photochemistry of MB at different excitation wavelengths, and the results are summarized as follows.

**2.3.2.1 Excitation of MB and plasmon resonances leads to demethylation.** As discussed above, excitation of the MB-AuNR sample with light energy that overlaps with both the electronic transition energy of MB and the plasmon resonance of the AuNR transforms MB to thionine. This conclusion is based on in situ SERS spectra, in which the vibrational signatures evolve from that of MB to that of thionine as a function of time as shown in Figures 2 and 3.

**2.3.2.2 Excitation of plasmon resonances but not MB does not lead to demethylation.** In this experiment, the excitation wavelengths (532 nm and 808 nm) are chosen such that they overlap with the plasmon resonances of the nanoparticles but not with the electronic transition energy of MB. As shown in **Figure 6a**, the plasmon resonances of aggregates of MB treated gold nanospheres (AuNSs, 40 nm diameter) and AuNRs (40 nm diameter and 148 nm length) overlap with the 532 nm and 808 nm excitation wavelengths, respectively, more significantly than with the 633 nm line. Representative SERS spectra acquired 30 seconds after continuous irradiation are compared in **Figure 5b**. The vibrational signatures of thionine are observed in the SERS spectra obtained at  $\lambda = 633$  nm for both the AuNSs (black line) and AuNRs (green line), where the prominent peaks of thionine at  $479\text{ cm}^{-1}$  and  $804\text{ cm}^{-1}$  are indicated by the vertical dashed cyan lines. In contrast, no vibrational signatures of thionine have been observed at the 532 nm (blue line) and 808 nm (red

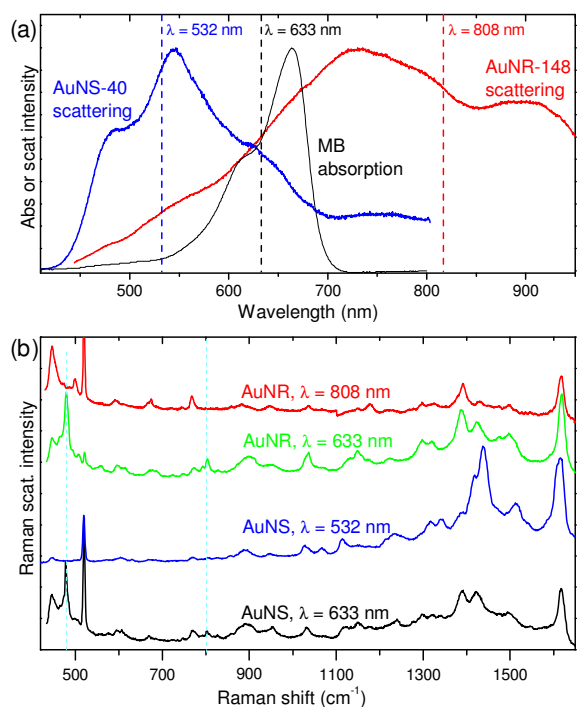


**Figure 6 Illustration of the importance of excitation energy overlap with the electronic transition of the molecule for the surface reaction to take place.** (a) Dark-field scattering spectra of aggregates of AuNSs (blue line) and AuNRs (red line) functionalized with MB and deposited on silica surface. (b) SERS spectra of MB adsorbed on the AuNS and AuNRs recorded 30 s after the excitation lasers are on. The vertical dashed cyan lines indicate the vibrational frequencies of thionine.

line) excitation laser lines despite the more significant spectral overlap of the plasmon resonances with the corresponding wavelengths as illustrated in **Figure 6a**. This wavelength dependent spectral evolution confirms the necessity of the electronic excitation of the molecule for the demethylation reaction to take place.

**2.3.2.3 Excitation of MB on non-plasmonic surfaces does not lead to demethylation.** We have verified that the demethylation reaction does not take place in the absence of plasmon resonances. That is, no new vibrational bands are observed when MB is adsorbed on non-plasmonic surfaces (*e.g.* glass, platinum, aluminum and gold) and excited with the 633 nm excitation laser line that overlaps with the electronic transition energy of MB. An example is shown in **Figure 7**, where the Raman spectra of MB adsorbed on gold film remains essentially the same upon continuous illumination regardless of the incident laser power intensity. The spectra in **Figure 7** were acquired at irradiation intensity of  $\sim 100,000 \text{ W/cm}^2$  at which the demethylation of MB was not observed. In contrast, in the presence of plasmon resonances, the demethylation reaction can be observed at incident laser intensity of  $100 \text{ W/cm}^2$ . This observation underscores the importance of plasmon resonances for the demethylation reaction.

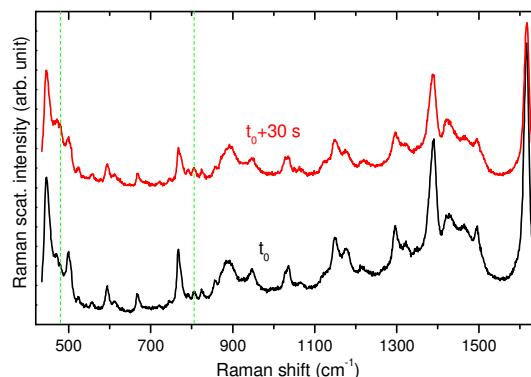


**Figure 7** Raman spectra of MB adsorbed on gold film in the absence of plasmonic nanoparticles.

**2.3.2.4 The reaction mechanism may involve singlet oxygen.** The fact that the N-demethylation reaction does not take place when MB is adsorbed on nonplasmonic surfaces suggests that the mechanism may involve hot plasmon electron transfer to adsorbate species. It has been reported that photocatalytic N-demethylation requires the presence of oxygen.<sup>39-41</sup> In particular Takizawa et al demonstrated systematically that anionic oxygen was responsible for initiating the demethylation of MB and Rhodamine B on CdS catalyst.<sup>39</sup> Transient anionic oxygen created via hot plasmon electron injection has also been implicated in the surface photochemistry of para-aminothiophenol.<sup>25, 26, 42</sup> These past experimental observations suggest that the demethylation of MB in our experiment is likely initiated by anionic oxygen.

On the other hand, electron transfer to triplet oxygen (ground state) can be ruled out based on the observation that the demethylation reaction does not take place at 532 nm and 808 nm excitation wavelengths that overlap with the plasmon resonances but not with the MB electronic transition energy. The requirement of the electronic excitation of the adsorbed molecule clearly indicates that the excited state dynamics of MB are involved in the reaction. The

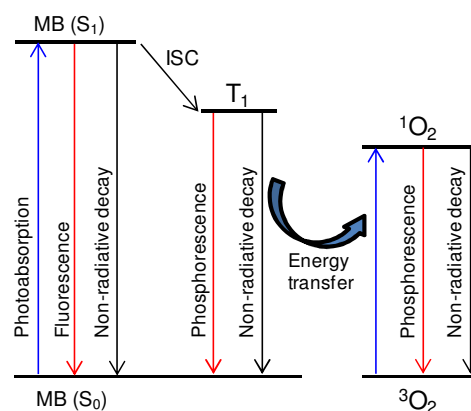


**Figure 8.** Energy diagram of methylene blue. The singlet ground state ( $S_0$ ) to singlet excited state ( $S_1$ ) transition is followed by the inter-system crossing (ISC) to the triplet state. Efficient energy transfer from  $T_1$  state to molecular oxygen ( $^3O_2$ ) creates singlet oxygen ( $^1O_2$ ).

solution phase excited state dynamics of MB is well documented<sup>43, 44</sup> and can be used as important background information in investigating its photochemistry on plasmonic metal surfaces. As shown in **Figure 8**, absorption of visible light (*e.g.*  $\lambda = 633$  nm) promotes MB from singlet ground state ( $S_0$ ) to singlet excited state ( $S_1$ ). After singlet-triplet intersystem crossing (quantum yield  $\sim 0.5$ ),<sup>45</sup> highly efficient energy transfer to triplet molecular oxygen generates singlet oxygen with quantum yield close to unity,<sup>46</sup> a reason for wide use of MB as photosensitizer in photodynamic therapy.<sup>46</sup>

The known excited state behavior of MB combined with our experimental observations summarized above suggests that the demethylation of MB is initiated by hot plasmon electron transfer to singlet oxygen that may form complexes with MB adsorbate. Singlet oxygen is known for its strong reactivity toward surfaces and organic molecules.<sup>46</sup> However, experimental validation of the proposed mechanism requires spectroscopic detection of singlet oxygen. In the future, we wish to provide direct experimental evidence for the generation of singlet oxygen by measuring its phosphorescence, which is known to appear at  $\sim 1270$  nm.

It is important to note that the critical role of singlet oxygen in plasmon driven photochemistry may not be specific to the demethylation of MB. In fact, plasmonic metal nanoparticles can serve as an effective photosensitizer to generate singlet oxygen.<sup>47</sup> On the other hand, typical plasmon driven or assisted photochemical reactions involve molecular oxygen.<sup>26, 48</sup> However, the electronic states of the molecular oxygen (singlet or triplet) that is involved in the chemical transformation have to be explored through further experimental innovations.

### 3. Summary

In summary, this research project has been transformational to Habteyes group to open up new and exciting research directions. Foundational works that may pave the way for utilizing localized surface plasmon resonances for plasma generation have been carried out. Super-resolved vibrational imaging of thin films has been demonstrated. A far-field microscope that allows correlated dark-field scattering and surface enhanced Raman scattering measurements have been developed. Using methylene blue as model molecular system, chemical transformation induced by plasmon enhanced resonant excitation of adsorbates has been reported for the first time. Based on the experimental results, the involvement of singlet oxygen has been proposed. Three research articles have been published. The initial results have stimulated new research directions for the coming several years in collaboration with the scientists at the Air Force Research Lab, Kirtland Air Force Base. Three graduate students and three female undergraduate students have been participating in this research project. The majority of the students are from historically under represented group of society.

## References

1. Russo, R. E.; Mao, X. L.; Yoo, J. H.; Gonzalez, J. J., Laser Ablation. In *Laser-Induced Breakdown Spectroscopy*, Singh, J. P.; Thakur, S. N., Eds. Elsevier: Amsterdam, The Netherlands, 2007.
2. Noll, R., *Laser-Induced Breakdown Spectroscopy*. Springer-Verlag: Berlin Heidelberg, 2012.
3. Fortes, F. J.; Moros, J.; Lucena, P.; Cabalin, L. M.; Laserna, J. J., Laser-Induced Breakdown Spectroscopy. *Anal. Chem.* **2013**, 85, 640-669.
4. Schmitz, T. A.; Koch, J.; Gunther, D.; Zenobi, R., Early Plume and Shock Wave Dynamics in Atmospheric-Pressure Ultraviolet-Laser Ablation of Different Matrix-Assisted Laser Ablation Matrices. *J. Appl. Phys.* **2011**, 109.
5. Hermann, J.; Gerhard, C.; Axente, E.; Dutouquet, C., Comparative Investigation of Laser Ablation Plumes in Air and Argon by Analysis of Spectral Line Shapes: Insights on Calibration-Free Laser-Induced Breakdown Spectroscopy. *Spectrosc. Acta Pt. B-Atom. Spectr.* **2014**, 100, 189-196.
6. Caprioli, R. M.; Farmer, T. B.; Gile, J., Molecular Imaging of Biological Samples: Localization of Peptides and Proteins Using Maldi-Tof Ms. *Anal. Chem.* **1997**, 69, 4751-4760.
7. Kim, S.; Jin, J. H.; Kim, Y. J.; Park, I. Y.; Kim, Y.; Kim, S. W., High-Harmonic Generation by Resonant Plasmon Field Enhancement. *Nature* **2008**, 453, 757-760.
8. Raschke, M. B., High-Harmonic Generation with Plasmonics: Feasible or Unphysical? *Ann. Phys.-Berlin* **2013**, 525, A40-A42.
9. Kafle, B.; Poveda, M.; Habteyes, T. G., Surface Ligand-Mediated Plasmon-Driven Photochemical Reactions. *J. Phys. Chem. Lett.* **2017**, 8, 890-894.
10. Tesema, T. E.; Kafle, B.; Tadesse, M. G.; Habteyes, T. G., Plasmon-Enhanced Resonant Excitation and Demethylation of Methylene Blue. *J. Phys. Chem. C* **2017**, 121, 7421-7428.
11. Nitzan, A.; Brus, L. E., Can Photochemistry Be Enhanced on Rough Surfaces. *J. Chem. Phys.* **1981**, 74, 5321-5322.
12. Nitzan, A.; Brus, L. E., Theoretical-Model for Enhanced Photochemistry on Rough Surfaces. *J. Chem. Phys.* **1981**, 75, 2205-2214.
13. Goncher, G. M.; Harris, C. B., Enhanced Photofragmentation on a Silver Surface. *J. Chem. Phys.* **1982**, 77, 3767-3768.
14. Bunding, K. A.; Durst, R. A.; Bell, M. I., Surface-Enhanced Raman-Spectroscopy of N-Methylpyridinium Cation and Pyridine - Identification of Surface Species. *J. Electroanal. Chem.* **1983**, 150, 437-446.
15. Goncher, G. M.; Parsons, C. A.; Harris, C. B., Photochemistry on Rough Metal-Surfaces. *J. Phys. Chem.* **1984**, 88, 4200-4209.
16. Lu, T.; Birke, R. L.; Lombardi, J. R., Surface Raman-Spectroscopy of the 3 Redox Forms of Methylviologen. *Langmuir* **1986**, 2, 305-309.
17. Wolkow, R. A.; Moskovits, M., Enhanced Photochemistry on Silver Surfaces. *J. Chem. Phys.* **1987**, 87, 5858-5869.
18. Sun, S. C.; Birke, R. L.; Lombardi, J. R.; Leung, K. P.; Genack, A. Z., Photolysis of Para-Nitrobenzoic Acid on Roughened Silver Surfaces. *J. Phys. Chem.* **1988**, 92, 5965-5972.
19. White, J. M., Photochemistry at Adsorbate Metal Interfaces - Issues and Examples. *J. Vac. Sci. Technol. B* **1992**, 10, 191-195.
20. Jeanmaire, D. L.; Vanduyne, R. P., Surface Raman Spectroelectrochemistry .1. Heterocyclic, Aromatic, and Aliphatic-Amines Adsorbed on Anodized Silver Electrode. *J. Electroanal. Chem.* **1977**, 84, 1-20.
21. Moskovits, M., Surface-Roughness and Enhanced Intensity of Raman-Scattering by Molecules Adsorbed on Metals. *J. Chem. Phys.* **1978**, 69, 4159-4161.
22. Suh, J. S.; Jang, N. H.; Jeong, D. H.; Moskovits, M., Adsorbate Photochemistry on a Colloid Surface: Phthalazine on Silver. *J. Phys. Chem.* **1996**, 100, 805-813.

23. Huang, Y.-F.; Zhu, H.-P.; Liu, G.-K.; Wu, D.-Y.; Ren, B.; Tian, Z.-Q., When the Signal Is Not from the Original Molecule to Be Detected: Chemical Transformation of Para-Aminothiophenol on Ag During the SERS Measurement. *J. Am. Chem. Soc.* **2010**, 132, 9244-9246.
24. Fang, Y. R.; Li, Y. Z.; Xu, H. X.; Sun, M. T., Ascertaining P,P'-Dimercaptoazobenzene Produced from P-Aminothiophenol by Selective Catalytic Coupling Reaction on Silver Nanoparticles. *Langmuir* **2010**, 26, 7737-7746.
25. Xu, P.; Kang, L. L.; Mack, N. H.; Schanze, K. S.; Han, X. J.; Wang, H. L., Mechanistic Understanding of Surface Plasmon Assisted Catalysis on a Single Particle: Cyclic Redox of 4-Aminothiophenol. *Sci Rep* **2013**, 3, 2997.
26. Huang, Y. F.; Zhang, M.; Zhao, L. B.; Feng, J. M.; Wu, D. Y.; Ren, B.; Tian, Z. Q., Activation of Oxygen on Gold and Silver Nanoparticles Assisted by Surface Plasmon Resonances. *Angew. Chem.-Int. Edit.* **2014**, 53, 2353-2357.
27. Yan, X. F.; Wang, L. Z.; Tan, X. J.; Tian, B. Z.; Zhang, J. L., Surface-Enhanced Raman Spectroscopy Assisted by Radical Capturer for Tracking of Plasmon-Driven Redox Reaction. *Sci Rep* **2016**, 6.
28. Mukherjee, S.; Libisch, F.; Large, N.; Neumann, O.; Brown, L. V.; Cheng, J.; Lassiter, J. B.; Carter, E. A.; Nordlander, P.; Halas, N. J., Hot Electrons Do the Impossible: Plasmon-Induced Dissociation of H<sub>2</sub> on Au. *Nano Lett.* **2013**, 13, 240-247.
29. Zhang, Y.; Xiao, Q.; Bao, Y.; Zhang, Y.; Bottle, S.; Sarina, S.; Zhaorigetu, B.; Zhu, H., Direct Photocatalytic Conversion of Aldehydes to Esters Using Supported Gold Nanoparticles under Visible Light Irradiation at Room Temperature. *J. Phys. Chem. C* **2014**, 118, 19062-19069.
30. Linic, S.; Aslam, U.; Boerigter, C.; Morabito, M., Photochemical Transformations on Plasmonic Metal Nanoparticles. *Nat. Mater.* **2015**, 14, 567-576.
31. Lombardi, J. R.; Birke, R. L., A Unified Approach to Surface-Enhanced Raman Spectroscopy. *J. Phys. Chem. C* **2008**, 112, 5605-5617.
32. Boerigter, C.; Campana, R.; Morabito, M.; Linic, S., Evidence and Implications of Direct Charge Excitation as the Dominant Mechanism in Plasmon-Mediated Photocatalysis. *Nat. Commun.* **2016**, 7, 10545.
33. Boerigter, C.; Aslam, U.; Linic, S., Mechanism of Charge Transfer from Plasmonic Nanostructures to Chemically Attached Materials. *ACS Nano* **2016**, 10, 6108-6115.
34. Cenens, J.; Schoonheydt, R. A., Visible Spectroscopy of Methylene-Blue on Hectorite, Laponite-B, and Barasym in Aqueous Suspension. *Clay Clay Min.* **1988**, 36, 214-224.
35. Jacobs, K. Y.; Schoonheydt, R. A., Time Dependence of the Spectra of Methylene Blue-Clay Mineral Suspensions. *Langmuir* **2001**, 17, 5150-5155.
36. Rubim, J. C.; Sousa, M. H.; Silva, J. C. O.; Tourinho, F. A., Raman Spectroscopy as a Powerful Technique in the Characterization of Ferrofluids. *Braz. J. Phys.* **2001**, 31, 402-408.
37. Otto, A.; Mrozek, I.; Grabhorn, H.; Akemann, W., Surface-Enhanced Raman-Scattering. *J. Phys.-Condes. Matter* **1992**, 4, 1143-1212.
38. Zhou, L.; Johnson, R.; Habteyes, T.; Guo, H., Adsorption of Methylene Blue and Its N-Demethylated Derivatives on the (111) Face of Coinage Metals: The Importance of Dispersion Interactions. *J. Chem. Phys.* **2017**, 146, 164701.
39. Takizawa, T.; Watanabe, T.; Honda, K., Photocatalysis through Excitation of Adsorbates .2. Comparative-Study of Rhodamine-B and Methylene-Blue on Cadmium-Sulfide. *J. Phys. Chem.* **1978**, 82, 1391-1396.
40. Zhang, T. Y.; Oyama, T.; Aoshima, A.; Hidaka, H.; Zhao, J. C.; Serpone, N., Photooxidative N-Demethylation of Methylene Blue in Aqueous TiO<sub>2</sub> Dispersions under UV Irradiation. *J. Photochem. Photobiol. A-Chem.* **2001**, 140, 163-172.
41. Yogi, C.; Kojima, K.; Wada, N.; Tokumoto, H.; Takai, T.; Mizoguchi, T.; Tamiaki, H., Photocatalytic Degradation of Methylene Blue by TiO<sub>2</sub> Film and Au Particles-TiO<sub>2</sub> Composite Film. *Thin Solid Films* **2008**, 516, 5881-5884.

42. Zhao, L. B.; Liu, X. X.; Zhang, M.; Liu, Z. F.; Wu, D. Y.; Tian, Z. Q., Surface Plasmon Catalytic Aerobic Oxidation of Aromatic Amines in Metal/Molecule/Metal Junctions. *J. Phys. Chem. C* **2016**, 120, 944-955.
43. Chen, J.; Cesario, T. C.; Rentzepis, P. M., Time Resolved Spectroscopic Studies of Methylene Blue and Phenothiazine Derivatives Used for Bacteria Inactivation. *Chem. Phys. Lett.* **2010**, 498, 81-85.
44. Dean, J. C.; Oblinsky, D. G.; Rafiq, S.; Scholes, G. D., Methylene Blue Exciton States Steer Nonradiative Relaxation: Ultrafast Spectroscopy of Methylene Blue Dimer. *J. Phys. Chem. B* **2016**, 120, 440-454.
45. Redmond, R. W.; Gamlin, J. N., A Compilation of Singlet Oxygen Yields from Biologically Relevant Molecules. *Photochem. Photobiol.* **1999**, 70, 391-475.
46. Tardivo, J. P.; Del Giglio, A.; de Oliveira, C. S.; Gabrielli, D. S.; Junqueira, H. C.; Tada, D. B.; Severino, D.; Turchiello, R. D. F.; Baptista, M. S., Methylene Blue in Photodynamic Therapy: From Basic Mechanisms to Clinical Applications. *Photodiagnosis Photodyn. Ther.* **2005**, 2, 175-191.
47. Vankayala, R.; Sagadevan, A.; Vijayaraghavan, P.; Kuo, C. L.; Hwang, K. C., Metal Nanoparticles Sensitize the Formation of Singlet Oxygen. *Angew. Chem.-Int. Edit.* **2011**, 50, 10640-10644.
48. Christopher, P.; Xin, H. L.; Linic, S., Visible-Light-Enhanced Catalytic Oxidation Reactions on Plasmonic Silver Nanostructures. *Nat. Chem.* **2011**, 3, 467-472.

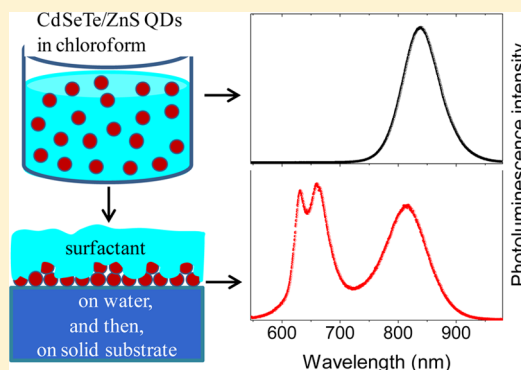
## **Appendix: Published articles**

# Stripping and Transforming Alloyed Semiconductor Quantum Dots via Atomic Interdiffusion

Bijesh Kafle,<sup>†,‡</sup> Tefera E. Tesema,<sup>†,‡</sup> Alireza Kazemi,<sup>‡</sup> and Terefe G. Habteyes\*,<sup>†,‡</sup><sup>†</sup>Department of Chemistry and Chemical Biology and <sup>‡</sup>Center for High Technology Materials, University of New Mexico, Albuquerque, New Mexico 87131, United States

## Supporting Information

**ABSTRACT:** We report the transformation of near-infrared CdSeTe/ZnS quantum dots (QDs) that are exposed to water. When the colloidal QDs with 840 nm emission wavelength and 75 nm spectral line width are self-assembled on water surface and transferred to an oxide-coated silicon wafer using a Langmuir–Blodgett (LB) procedure, two prominent relatively sharp photoluminescence (PL) bands are observed at ~630 and ~660 nm peak wavelengths with line width of ~23 and ~39 nm, respectively. On the other hand, the PL spectrum of the QDs as they are assembled on the water surface is essentially the same as that of the solution phase. Structural analysis of the LB films shows that the QDs are stripped off the stabilizing excess surfactant molecules by the preferential interaction at the water–air interface. After the film is transferred, the QDs are interfaced with each other and with the substrate directly, while covered with the stack of surfactant molecules from the top. Based on analysis of the chemical composition using X-ray photoelectron spectroscopy of the LB film, the transformation of the CdSeTe/ZnS nanocrystals is attributed to a diffusion of Te atoms from the core to the shell that can initiate inward diffusion of S atoms. This atomic interdiffusion minimizes lattice mismatch as the larger Te atoms are replaced by the smaller S atoms and can lead to formation of either CdSe/CdS or CdSeS nanocrystals that emit at 630 and 660 nm wavelengths, respectively.



## INTRODUCTION

As the synthesis of semiconductor nanocrystals is advancing, understanding their behavior under different environmental conditions is critically important for many applications including biological imaging,<sup>1</sup> solar cells,<sup>2–4</sup> and detection.<sup>5–7</sup> To date, chemical, photochemical, and photophysical studies of semiconductor nanocrystals have been focused on binary nanocrystals such as CdSe,<sup>8–18</sup> CdTe,<sup>19–22</sup> PbS,<sup>23–27</sup> and PbSe<sup>28–30</sup> quantum dots (QDs). In general, for these binary QDs, the expected changes in optoelectronic properties are related to chemical modification of the crystal surfaces that can be passivated by growing higher band gap materials<sup>31–33</sup> and surface chemical treatments.<sup>34–38</sup> One of the attractive characteristic of semiconductor QDs is tunability of their band gap energy or emission wavelength simply by changing their size for a fixed material composition.<sup>39</sup> However, the tunability afforded by size variation is limited and does not allow covering the NIR spectral region, for example, using the most common CdSe and CdTe nanocrystals. QDs that absorb and emit NIR photons are needed for both biological imaging (due to the deeper penetration of NIR radiation into tissues than visible wavelengths)<sup>40,41</sup> and for solar cell applications as the NIR region covers a significant portion of the solar spectrum. Alloyed ternary nanocrystals such as CdSe<sub>1–x</sub>Te<sub>x</sub> provide broader band gap tunability to cover the 700–900 nm spectral region via variation of the composition  $x$ .<sup>42–44</sup> This has

been the motivation for the continual advancement of chemical synthesis of alloyed nanocrystals.<sup>43,45–49</sup> However, the behavior and stability of alloyed nanocrystals can differ from the binary nanocrystals drastically because of the lattice mismatch between the binary components, and yet postgrowth studies of physical and chemical properties is lacking. Understanding their stability and behavior under different environmental exposure is critically important for any technological application.<sup>50</sup>

In this work, using CdSe<sub>1–x</sub>Te<sub>x</sub> QDs as model systems, we study the transformation of alloyed nanocrystals self-assembled on water surface. The formation free energy ( $\Delta A$ ) of an alloyed CdSe<sub>1–x</sub>Te<sub>x</sub> nanocrystal at its equilibrium configuration  $\sigma$  can be written as<sup>42,51</sup>

$$\Delta A(\sigma) = A(x, \sigma) - [(1-x)A_{\text{CdSe}}(a_{\text{CdSe}}) + xA_{\text{CdTe}}(a_{\text{CdTe}}) + E(x)] \quad (1)$$

where  $A$ ,  $A_{\text{CdSe}}$ , and  $A_{\text{CdTe}}$  are the Helmholtz free energies of the alloy, pure CdSe, and pure CdTe, respectively, containing the same number of Cd atoms;  $a_{\text{CdSe}}$  and  $a_{\text{CdTe}}$  are the equilibrium lattice constants of the binary compounds; and  $E(x)$  is the strain energy cost to maintain lattice coherence at

Received: March 22, 2016

Revised: May 21, 2016

Published: May 25, 2016

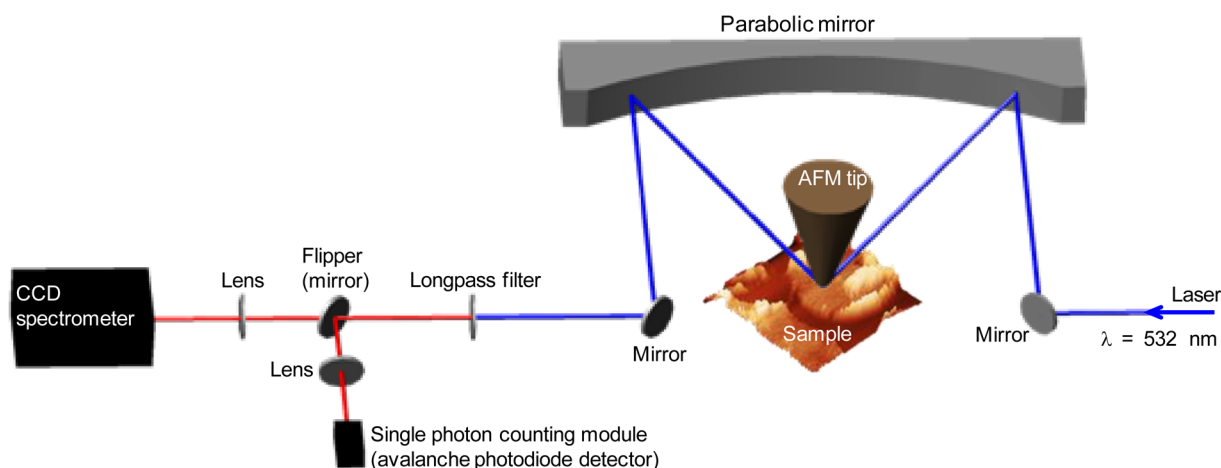


**Figure 1.** Schematic of the microscopy and spectroscopy setup. Collimated laser beam is focused at the tip–sample junction using a parabolic mirror and collected on the opposite side using the same parabolic mirror. The emitted light is detected using the single photon counting module (SPCM) or the CCD spectrometer to obtain spectral information. Photoluminescence (PL) intensity images are obtained by recording the output of the SPCM, while the sample is raster scanned. The PL intensity and AFM images of the same sample area are obtained simultaneously or sequentially so that structural and optical information are correlated. After scan images are obtained spectral information on a specific area is recorded by centering the region of interest in the laser focus and directing the light to the spectrometer.

the interface.<sup>51</sup> For solids, where the volume change is negligible, the changes in the internal energy ( $\Delta U$ ) and enthalpy ( $\Delta H$ ) can be assumed equal, and the Gibbs free energy change ( $\Delta G = \Delta H - T\Delta S$ ) can be used in place of  $\Delta A = \Delta U - T\Delta S$ , where  $T$  is temperature and  $\Delta S$  is entropy change. Generally,  $\Delta H$  is positive that results in large miscibility gap in the  $x$ – $T$  phase diagram, where the binary components phase separate and exist at their equilibrium lattice constants. Extensive theoretical studies by Zunger and co-workers show that the interfacial strain energy can lower  $\Delta H$  to an extent that it can be negative, resulting in growth conditions in which ordered alloyed and superlattice crystal structures can be formed even at room temperature.<sup>51,52</sup> However, depending on the thermodynamic and kinetic conditions, atomic interdiffusion can transform the fabricated alloyed nanocrystals to different crystal forms and compositions.

Atomic interdiffusion in epitaxially grown semiconductor heterostructures has been observed for various systems including GeSi/Si,<sup>53,54</sup> and InGaAs/GaAs.<sup>55,56</sup> Interfacial structures at much lower temperature than expected according to the activation energy required for atomic diffusion. Although the reason for the low temperature interdiffusion has been debated<sup>57</sup> following the first report,<sup>53</sup> it is likely that the lattice strain enhances crystal defect concentration that is known to facilitate atomic diffusion.<sup>55</sup> Interfacial diffusion has also been observed in colloidal nanorods with CdTe/CdSe heterojunction, where the diffusion of Te and Se atoms across the junctions results in nanorods with reduced length-to-width aspect ratio and uniform composition across its length and width.<sup>58</sup>

This work is focused on providing experimental evidence for the transformation of NIR CdSeTe/ZnS core/shell QDs to red-emitting nanocrystals when the NIR QDs self-assembled on water surface and transferred to a solid substrate. The crystal transformation is studied by analyzing the photoluminescence (PL) spectral characteristics as it has been successfully applied in previous studies of interdiffusion in epitaxially grown semiconductor heterostructures.<sup>56</sup> The interpretation of the PL data is supported by analysis of the chemical composition using XPS as well as structural and size analysis using atomic

force microscope (AFM) and transmission electron microscope (TEM). When the alloyed QDs that emit at 840 nm are assembled on water surface, transferred to an oxide coated silicon wafer, and photoexcited, two new emission peaks at  $\sim 630$  and  $\sim 660$  nm are observed, which are assigned to CdSe and CdSeS core nanocrystals, respectively. A plausible mechanism is suggested for the crystal transformation. The alloyed CdSeTe/ZnS core/shell QDs are likely to be in metastable state due to lattice mismatch and the strain energy cost as well as concentration of point defects. There is about 6% lattice mismatch between CdSe and CdTe and 17% between ZnS and CdTe.<sup>59</sup> Lattice strain is believed to increase concentration of point defects<sup>55</sup> that reduces the resistance for diffusion compared to in a perfect crystal.<sup>60</sup> On the other hand, the lattice mismatch is minimized if the relatively larger Te atoms are replaced by S atoms through the process of atomic interdiffusion.

## EXPERIMENTAL SECTION

**Sample Preparation.** The CdSeTe/ZnS core/shell QDs suspended in toluene were obtained from the NanoOptical Materials Inc. To make the solution suitable for LB procedure, the toluene solvent was evaporated in vacuum, and the QDs were resuspended in chloroform to attain concentration of 10 mg/mL. The LB films were prepared on oxide coated silicon wafer that was cleaned by sonicating in acetone, isopropanol, and ultrapure water for 5 min each, followed by 5 min ultraviolet ozone treatment (Novascan Technologies, Inc.). After the substrate was rinsed with ultrapure water and blow-dried with nitrogen, it was immersed in the ultrapure water subphase in the LB trough (KSV NIMA). The QD solution was gently applied to the water surface using Hamiltonian microliter syringe and was allowed to stabilize for different duration depending on the target exposure time of the QDs to the water surface. The film was then compressed at a typical speed of 10 mm/min until a target pressure of 20–35 mN/m was attained. The compressed film was stabilized for about 5 min and transferred to the substrate by pulling the substrate out at a speed of 5 mm/min at a constant compression surface pressure. The transfer was also carried out by scooping the compressed

film manually holding the substrate at  $5^{\circ}$ – $10^{\circ}$  from the water surface and gently pulling out, which resulted in more continuous film.

**Structural and Optical Characterization.** Schematic of the experimental setup used for the optical characterization of the QD films is shown in Figure 1. The excitation laser is focused at the AFM tip–sample junction using a parabolic mirror (numerical aperture, NA = 0.46). The AFM (Neaspec GmbH) is operated by scanning the sample, while the tip is stationary. The topography and PL intensity images can be obtained simultaneously but to avoid PL quenching by the tip, the images are obtained sequentially without losing the center of the scan. That is, during the PL scan, the tip is retracted up vertically, and intensity images are obtained detecting the emitted photons using a single photon counting module (Excelitas Technologies Corp.). The PL spectra of an area of interest are acquired by directing the emitted light to the spectrometer (IsoPlane Spectrograph of Princeton Instruments) that uses thermoelectrically cooled ( $-75^{\circ}\text{C}$ ) and back-illuminated deep depletion CCD camera. The results obtained at 532 nm excitation wavelength are used in our subsequent discussion. However, the results are also reproduced at 405 and 633 nm excitation wavelengths. In addition, the PL spectra of the QDs were recorded as the QDs were assembled on water surface. For this part of the experiment, a transparent 2 in. wafer holder was used to contain the water so that illumination and collection could be performed through the bottom of the container.

The size of the QDs has been analyzed using a JEOL 2010 TEM operated at 200 kV acceleration voltages. A significant amount of the excess surfactant molecules (mixture of trioctylphosphine oxide and hexadecylamine) was removed to improve the image contrast. The chemical composition of the QD film was analyzed using X-ray photoelectron spectrometer (Kratos Ultra DLD spectrometer, Al K $\alpha$  source at 225 mW). Three areas per sample were analyzed. Low and high resolution spectra were acquired at 80 and 20 eV pass energies, respectively. Charge neutralizer was utilized for charge compensation at bias voltage of 3.1 V, filament voltage of  $-1.0$  V, and filament current of 2.1 A. Data analysis and quantification were performed using the CasaXPS software, and a Shirley background was used. All the spectra were charge referenced to the C 1s at 285.0 eV.

## RESULTS AND DISCUSSION

A representative TEM image of the QDs is presented in Figure 2a, and the size distribution is plotted in Figure 2b. The average diameter is determined as  $6.7 \pm 0.8$  nm, where the uncertainty represents one standard deviation. The PL spectra of the QDs in solution (Figure 2c) confirm that replacing the toluene solvent with chloroform as described in the Experimental Section has no effect on the emission property of the QDs as can be seen from the overlap of the blue and green curves with peak position at  $\lambda = 840$  nm and full width at half-maximum (fwhm) of  $\sim 75$  nm. The QDs have also similar spectral characteristics when they are assembled on the water surface as shown by the red curve. The AFM height (Figure 3a) and phase (Figure 3b) images show the packing of the QDs, where the thickness of the excess surfactant deposited on top of the QDs is minimal. In this region, the thickness of the QD film ranges from 10 to 25 nm compared to  $\sim 6.7$  nm average diameter of the QDs determined from the TEM images. Assuming about 1.5 nm thickness of surface ligands, the

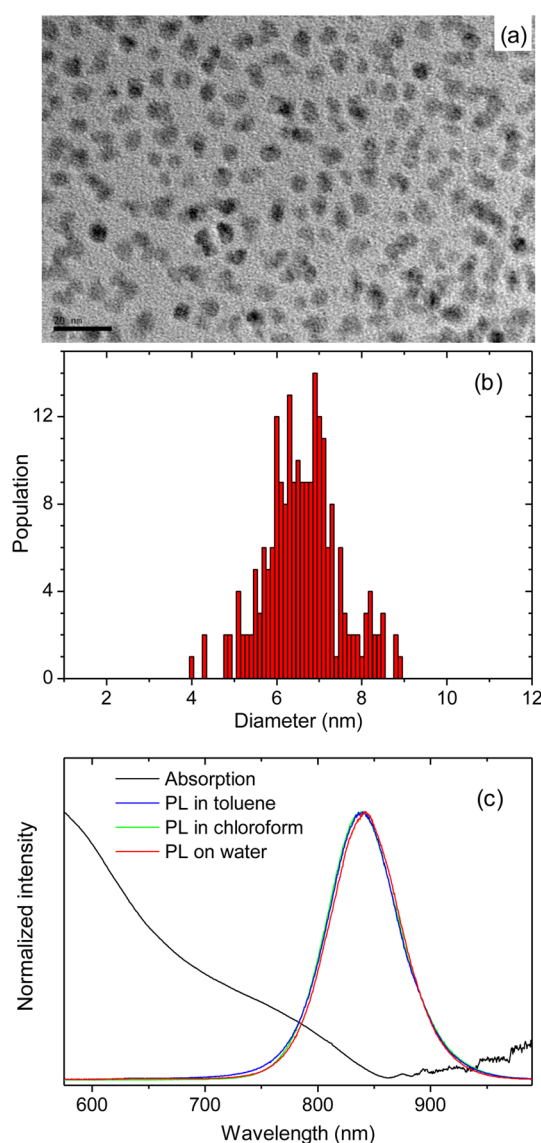


**Figure 2.** (a) TEM image of the NIR CdSeTe/ZnS QDs used in this study. (b) Size distribution of the QDs. (c) Absorption and PL spectra of the QDs suspended in toluene (blue line), suspended in chloroform (green line), and assembled on water (red line).

smallest film thickness ( $\sim 10$  nm) determined from the AFM images agrees with the TEM data. However, the film thickness is much larger than 10 nm in the significant portion of the film, indicating aggregation of the QDs (while on the water surface during the LB procedure) that produces thicker than a monolayer film. In the overwhelmingly large portion of the film, the QDs are covered with thick layer of excess surfactant as shown in Figure 3c–e. The stabilizing excess surfactant can be removed at a risk of introducing destabilizing effects, but it is not necessary for the present study. When the solution is spread over water, the QDs and the stabilizing excess surfactant form separate layers as a result of different favorable interaction at the water–air interface. In effect, the QDs are confined between the water surface and the excess surfactant for the duration of the LB procedure. After the transfer, the naked surfaces of QDs are interfaced with the substrate directly and covered by the blanket of surfactant layer from the top. In this regard, the presence of the excess surfactant is beneficial for the present study because it minimizes exposure of the QDs to air

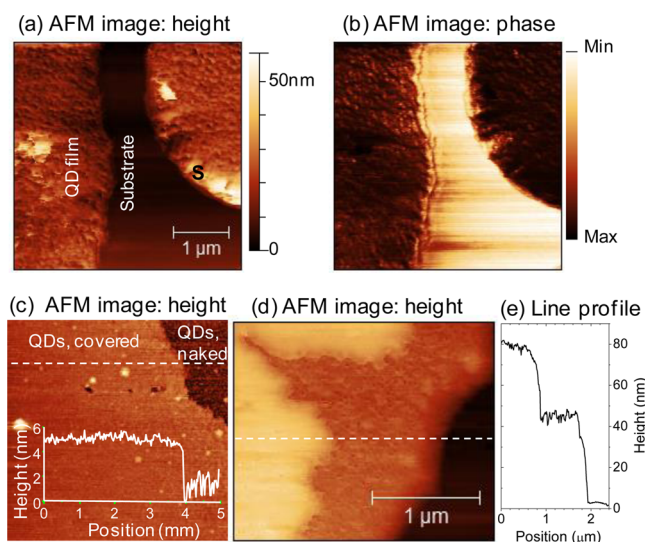


**Figure 3.** AFM height (a) and phase (b) images of the LB film of QDs, where coverage with surfactant (S) molecules is minimal. (c) AFM image of the QD film coated with thin layer of surfactant layer. (d) AFM image of the QD film coated with stack of surfactant layer (representative of large portion of the film). (e) Line profile across the dashed line in (d) shows the thickness of the surfactant layers.

(oxygen) during and after the film preparation, prolonging their stability at ambient condition.

The results obtained on the QD film that is exposed to water for about 7 min are presented in Figure 4. In the topographic AFM image displayed in Figure 4a, stacks of surfactant molecules are evident but the PL intensity image (Figure 4b) obtained at  $\lambda = 532$  nm excitation wavelength reveals that the QDs are present underneath the thick surfactant layer. The variation of the PL intensity across the scan area ( $90 \times 90 \mu\text{m}^2$ ) confirms that the QD film is not uniform throughout. The relatively high intensity in some areas is indicative of aggregation of the QDs. This type of nonuniformity of LB film has not been observed for CdSe/ZnS and CdSeS/ZnS core/shell QDs, where uniformly close-packed monolayer films are obtained, consistent with previous studies.<sup>61</sup> Nevertheless, for the alloyed QDs exposed to water for 7 min, the PL spectra (Figure 4c) acquired from different areas are similar apart from the intensity variation that is also evident in the intensity image. The PL peak observed at 840 nm in solution is blue-shifted to  $\sim 820$  nm, and the line width is broadened from 75 to  $\sim 83$  nm, which may indicate significant changes in the surface chemical properties and introduction of defects when the film is transferred to the substrate. In contrast, for CdSe/ZnS and CdSeS/ZnS QD films, the spectral characteristics of the QDs in the solid film are the same as that of the QDs suspended in solution. This stability difference can be attributed to the reactivity of the CdSeTe QDs and the ZnS coating is less likely to be a continuous shell. The more striking effect of exposing the alloyed QDs to water and transferring to the solid surface is the observation of weak peaks at 630 and 660 nm that do not appear in the solution phase PL spectra (see Figure 2c) and in the spectra of the QDs as they are assembled on the water subphase before the film transfer. As can be seen in the inset figure in Figure 4c, the relative intensity of the two new peaks varies when the spectra are acquired at different locations but the peak wavelengths are consistently within the ranges of

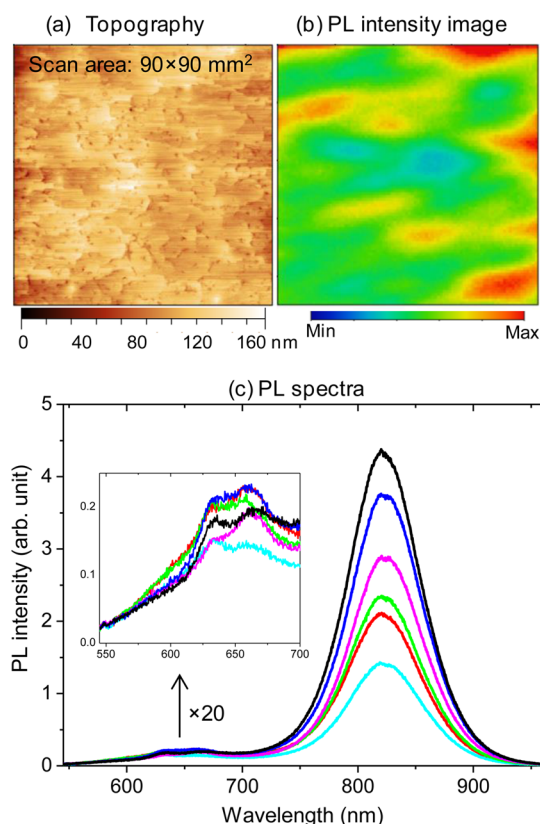


**Figure 4.** Results on the QD film exposed to water for  $\sim 7$  min. (a) AFM and (b) PL scan images of the same area ( $90 \times 90 \mu\text{m}^2$ ) of the QD film coated with excess surfactant. (c) Representative PL spectra obtained at different locations on the film. The variation of the PL at different locations is due to the nonuniformity of the film, which can also be seen in the PL intensity image in (b). Enlarging the intensity scale by a factor of 20, two weak peaks are observed at  $\sim 630$  and  $\sim 660$  nm with different relative intensity at different locations as seen in the inset of (c).

630–633 and 660–665 nm (for simplicity, these peaks will be referred as 630 and 660 nm peaks from now on).

The results on the QD film exposed to water for  $\sim 20$  min are presented in Figure 5. As discussed above, the QDs are covered with excess surfactant layer (Figure 5a), and the PL image (Figure 5b) shows intensity variation within the scan area. Five regions are numbered in the PL intensity image for further analysis. The representative PL spectra shown in Figure 5c are drastically different from that of the solution phase shown in Figure 2c. The weak intensity peaks at 630 and 660 nm observed in Figure 4 ( $\sim 7$  min exposure time) are now dramatically enhanced to the extent that they are comparable to or stronger than the original peak at 820 nm. The new peaks have characteristically much narrower line widths ( $\sim 23$  nm for the 630 nm and  $\sim 39$  nm for the 660 nm) than the peak at 820 nm that has a line width of  $\sim 83$  nm. Clearly, these short wavelength peaks with narrow line widths cannot be assigned to emissive deep trap surface states, which usually have very broad spectral features and appear at longer wavelengths than the main core emission resonances.<sup>62,63</sup> As mentioned above, the preferential interaction at the water–air interface pushes the surfactant molecules up and leaves QDs on the water surface. The fact that the relative intensity of the 630 and 660 nm peaks is higher for films exposed to water for longer time suggests that the origin of the new peaks is related to interfacial

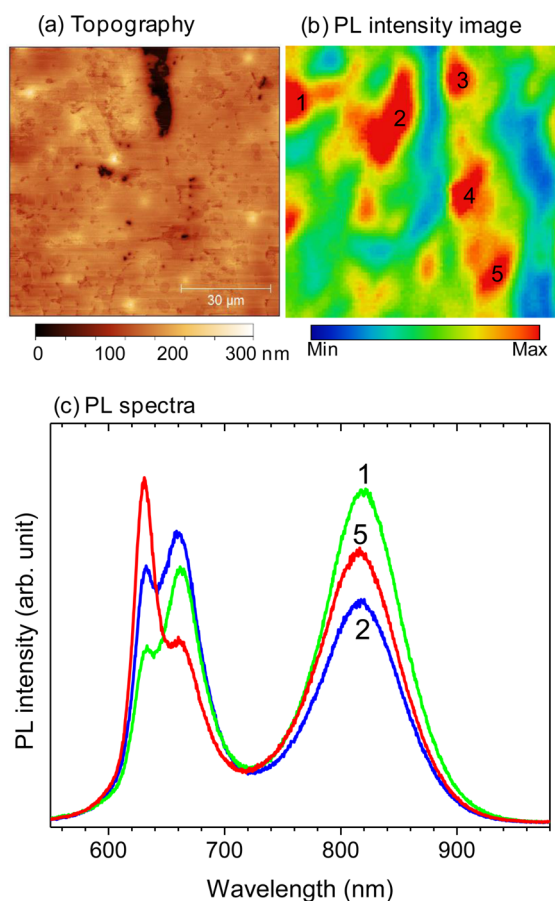


**Figure 5.** Results on the QD film exposed to water for  $\sim 20$  min. (a) AFM and (b) PL scan images of the same area ( $90 \times 90 \mu\text{m}^2$ ). (c) Representative PL spectra obtained by centering selected regions [marked 1, 2, and 5 in (b)] in the laser focus.

interaction on the substrate that is possible when the QDs are stripped off the stabilizing excess surfactant molecules, and complete stripping of the surface ligands by the preferential interaction at the water–air interface takes longer than 10 min.

For understanding the origin of the new emission peaks, the spatial distribution of the emitters has been analyzed using spatio-spectral imaging as demonstrated in Figure 6a–c. That is, using short-pass and long-pass spectral filters, the emission peaks in the red and near-infrared spectral regions are selectively mapped as shown in Figures 6b and 6c. Comparing the short ( $\lambda < 695$  nm, Figure 6b) and long ( $\lambda > 750$  nm, Figure 6c) wavelength intensity images, significant differences can be observed in the spatial distribution of the emitters. For example, the regions labeled 2 and 4 are the brightest spots when shorter wavelength photons are detected as seen in Figure 6b. But when the longer wavelength photons are detected, these regions have about average PL intensity as seen in Figure 6c. On the other hand, region 1 has the highest intensity when the longer wavelength photons are detected but only average intensity for short wavelength photon detection (similar results obtained on a different sample are compared in Figure S1). The stark difference in the spatio-spectral images clearly indicate that the emission peaks in the red ( $\lambda \sim 630$  and  $660$  nm) and near-infrared ( $\lambda \sim 820$  nm) spectral regions do not originate from the same nanocrystals and therefore cannot be assigned to an interface or deep trap surface states within the alloyed CdSeTe/ZnS quantum dots. Hence, the 630 and 660

nm peaks must be due to new nanocrystals that are formed when the alloyed NIR QDs are exposed to water and transferred to a solid substrate.

The relative photostability of the nanocrystals is studied by monitoring the PL intensity at 630, 660, and 820 nm wavelengths as a function of time, while keeping the laser focus at the region labeled 3 in Figures 6b and 6c, where the PL intensities in the two images are comparable. The photobleaching trend can be seen in the representative spectra (Figure 6d) acquired at different times. For more quantitative comparison, the peak intensities are plotted as a function of time in Figure 6e, after normalization of the intensities such that the initial value is unity for each peak. Rapid exponential decay is observed for the 820 nm peak intensity. In contrast, the 630 nm peak intensity first increases during the first  $\sim 50$  s and decreases monotonically for the longer illumination time. The 660 nm peak intensity decays at a slower rate than the 820 nm peak but faster than that of the 630 nm. The peak intensity decays at different rates when monitored at different locations, but the relative order of the photostability remains the same. The relative photostability of the 630 and 660 nm peaks suggests that the new nanocrystals have more stable surface chemical properties than the original NIR QDs. This may suggest that the larger and more reactive Te atom has diffused out of the core of the nanocrystals. This process can lead to the formation of CdSe based nanocrystals that can emit at 630 nm. The outward diffusion of Te can also result in an inward diffusion of S atom from the ZnS shell, which can plausibly result in the formation of CdSeS alloyed nanocrystals that emit at 660 nm. This proposed mechanism is supported by analyzing the effect of water medium as follows.

The role of water medium in facilitating the crystal transformation can be understood by comparing the spectra of the LB films to that of the films prepared by drop-casting (DC) the quantum dot solution directly on the substrate and to the spectra of the QDs as they are assembled on the water surface as demonstrated in Figures 7. As it can be seen in Figure 7, the 630 and 660 nm peaks are completely absent for the QDs on the water surface (black line) and are hardly noticeable in the PL spectrum of the film prepared by the DC procedure (blue line). For the DC film, signatures of the two peaks become apparent when the intensity scale is enlarged by a factor of  $>20$  (see Figure S2), suggesting that spreading the QD–surfactant mixture on the substrate has similar but negligible effect as on the water surface in the LB procedure. Unlike on the water surface, when the solution is directly spread on the substrate, the QDs are not effectively separated from the surfactant molecules, and therefore they are dried as they are embedded in the stabilizing molecules. Exposing the DC film to air for extended time does not result in the growth of peaks at 630 and 660 nm. In contrast, when the QD solution is spread on water surface during the LB procedure, the QDs and stabilizing surfactant molecules are separated, forming water–QDs–surfactant–air interface as discussed above. When the film is transferred, the naked side of the QDs is directly interfaced with the substrate, which may create a chemical potential gradient to facilitate outward diffusion of Te atom and minimize lattice mismatch in the crystal.

The composition of the nanocrystals has been studied by analyzing the X-ray photoelectron spectra of the DC and LB QD films. Representative results are compared in Figure 8. The overall spectra are in good agreement with published results,<sup>8,21</sup> and the discussion here primarily focuses on the comparison of

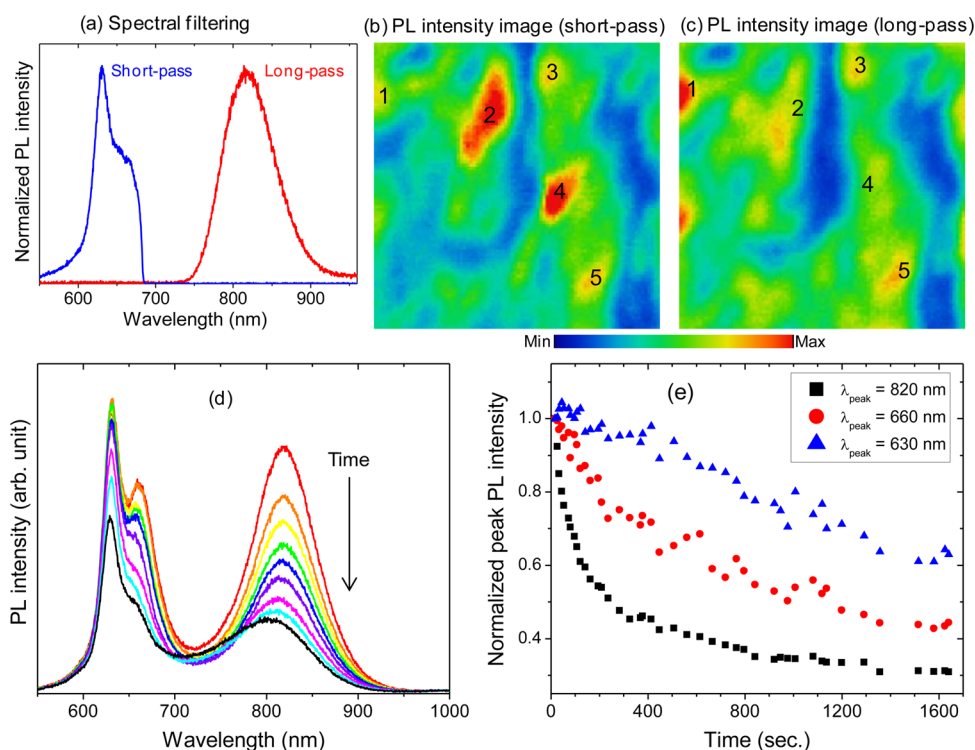


**Figure 6.** Spatospectral analysis of the sample region imaged in Figure 5. (a) Application of short-pass and long-pass filters to selectively map the different spectral regions. The PL scan obtained with short-pass (b) and long-pass (c) reveals different spatial localization of the red-emitting and NIR-emitting quantum dots (compare the areas marked 1, 2, and 4 in the two PL intensity images). (d) PL spectra obtained by centering the region marked 3 (b, c) in the laser focus and monitoring the PL spectra as a function of time. (e) Peak PL intensity extracted from (d) plotted as a function of time.

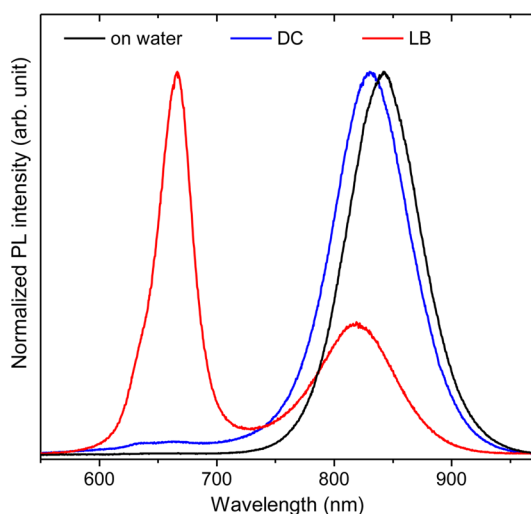


**Figure 7.** Representative PL spectra (normalized to the same maximum) obtained on QD films prepared by LB (red line) and drop-casting (DC) (blue line) procedures compared to the spectra of the QDs as they are assembled on the water surface (black line). The DC film is prepared by applying the solution (QDs in chloroform) directly onto the substrate, avoiding the exposure to water.

the spectra for the DC and LB films. Analysis of the spectra indicates that the Te to Se composition ratio is 0.18 for the DC film, which corresponds to  $\text{CdSe}_{0.85}\text{Te}_{0.15}$  approximate composition. The composition of Zn and S are determined as  $\sim 8.5\%$  each, which correspond to a slightly less than a monolayer thickness of ZnS shell and a 6.3 nm core diameter of CdSeTe. The experiment has been performed on two sets of

samples, and reproducibly significant broadening of peaks has been observed for the LB films with respect to the corresponding transitions for the DC films as illustrated in Figure 8a–c for Cd, Se, and Te 3d bands. For example, the fwhm of the  $\text{Cd}_{3/2}$  transition band is 0.97 eV for the DC film, which is in good agreement with the literature value of 0.98 eV for CdSe/ZnS QDs,<sup>64</sup> and it increases to 1.28 eV for the LB film. Closely inspecting all the spectra presented in Figure 8, greater degree of asymmetry can be seen on the higher energy side for the LB film than for the DC film. This may be attributed to significant changes of surface properties and increased contribution of surface atoms.<sup>64</sup> The weak peak at 406.6 eV in Figure 8a is reproducible, which may be indicative of Cd–S bond in the crystal.<sup>65</sup> We note that the spectra in Figure 8 are for the case in which prominent oxidation peaks (e.g.,  $\text{TeO}_2$  that we have observed at  $\sim 576.0$  eV for samples exposed to air for longer times) are completely absent, and therefore none of the spectral features can be attributed to oxidation effects.

The LB and DC films have also been compared by calculating the ratio of the respective compositions for each atom as plotted in Figure 8d. Ideally, the ratio should be 1.0 for all of the atoms as long as the crystals remain intact. The significant deviation for zinc (ratio of 0.24) from unity can be due to two possible reasons: (i) a loss of Zn from the ZnS shell during the LB procedure or (ii) a change in the overlayer (surfactant) thickness. The loss of zinc is expected to introduce surface defects that should change the spectral characteristics of the QDs significantly. However, as shown in Figure 2c, the peak wavelength and fwhm of the PL spectra of the QDs assembled on water surface are essentially the same as that of the original

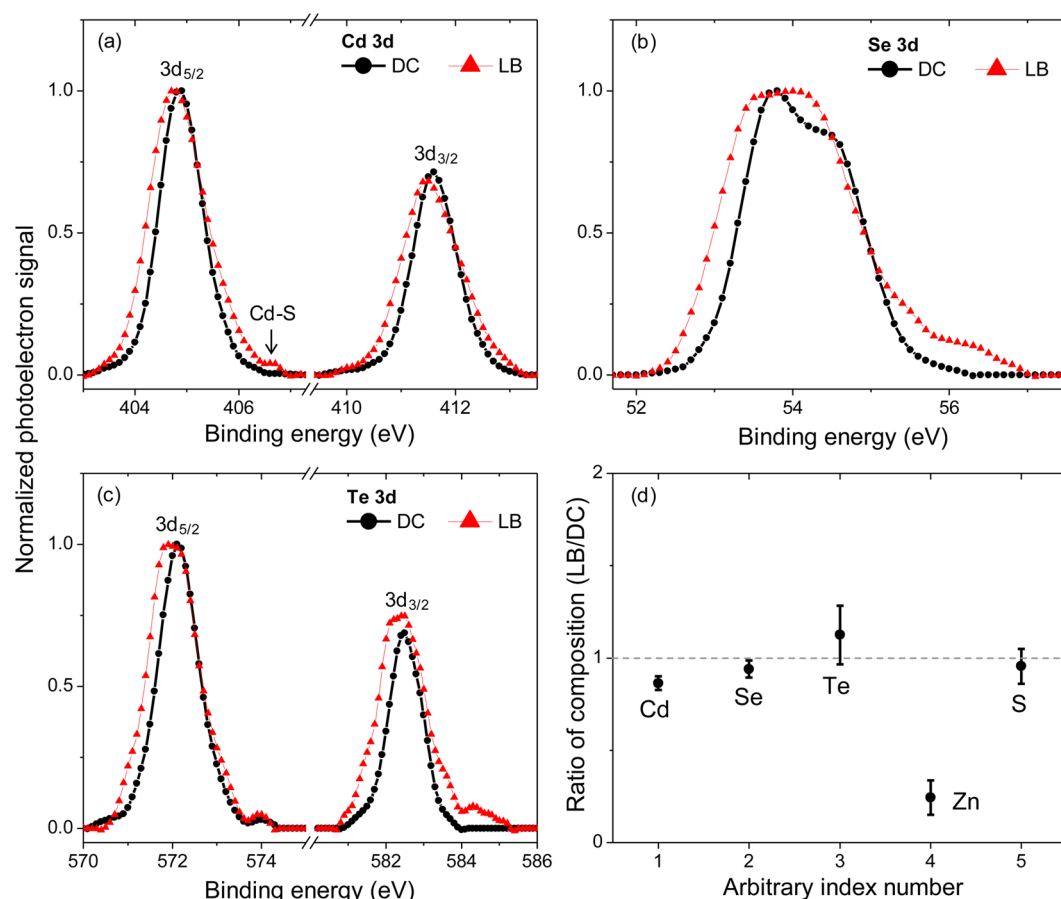


**Figure 8.** (a–c) Comparison of X-ray photoelectron spectra of QD films prepared through drop-casting DC (black curves) and LB (red curves) procedures. (d) Ratio of composition of LB to DC for Cd 3d, Se 3d, Te 3d, Zn 2p, and S 2p electrons.

solution. Therefore, we conclude that the ZnS shell remains intact while the QDs are on the water surface (until the film is transferred to the substrate). On the other hand, as shown in Figure 3 and discussed above, the interfacial interaction at the water–air interface creates a thick surfactant layer that covers the quantum dots. As a result, on average the QDs in the LB film are covered by a thicker surfactant layer than in the DC film, which results in weaker signal for all the atoms in the LB film because the electron signal is proportional to  $\exp(-(t/L) \cos \theta)$ , where  $t$  is the thickness of the overlayer,  $L$  is the inelastic mean free path of the electron at a given energy, and  $\theta$  is the signal collection angle (the angle of photoelectrons with respect to the surface normal).<sup>66</sup> With a binding energy of 1022 eV, the Zn 2p<sub>3/2</sub> electrons have the lowest kinetic energy (465 eV) and the shortest  $L$  (1.6 nm), compared to the kinetic energy of 1323 eV and  $L \approx 3.5$  nm for S 2p electrons, for example.<sup>67</sup> Therefore, the signal attenuation is expected to be most pronounced for zinc with increasing overlayer thickness, resulting in the observed deviation of composition ratio from an ideal value of 1.0.

For Te, the LB to DC composition ratio is slightly higher than 1.0 despite the fact that for Te 3d electrons the effective attenuation length is shorter than that of the Cd 3d and Se 3d electrons.<sup>67</sup> In addition, with respect to the composition of the DC film, there is significant increase of ratio of Te 3d signal to the other signals for the LB film: an increase of  $\sim 16\%$ ,  $\sim 20\%$ , and  $\sim 17\%$  with respect to Cd 3d, Se 3d, and S 2p, respectively. This observation of relative increase of Te 3d signal indicates that the relative concentration of Te on the surface of the

nanocrystals has increased, which is a direct evidence of diffusion of Te from the core to the shell. This outward diffusion of Te can lead to an inward diffusion of S to fill the vacant sites. This process minimizes the lattice mismatch and the strain energy cost as the larger Te atoms are replaced by the smaller S atoms. This observation is in agreement with the appearance of CdS signature in the Cd 3d band (Figure 8a), and the atomic interdiffusion can result in the transformation of CdSeTe/ZnS either to CdSe/CdS nanocrystals that emit at 630 nm or to alloyed CdSeS nanocrystals that emit at 660 nm. At the same time, it is likely that the ZnS shell is transformed to ZnTe.

LB films of CdSe/ZnS and CdSeS/ZnS core/shell QDs have been prepared and the spectral characteristics of the film are essentially the same as that of the solution phase. This observation further confirms that the transformation of CdSeTe/ZnS nanocrystals is due to the large lattice mismatch and strain energy that can be minimized when the bigger Te atoms in the crystal core are replaced by the smaller S atoms through the process of interdiffusion of atoms. Since the spectral changes (appearance of the 630 and 660 nm peaks) have been observed after the QDs are transferred from the water surface to the substrate, interfacial interactions and/or exposure to air (oxygen) can be proposed as possible factors that facilitate the atomic interdiffusion process. The 630 and 660 nm peaks have been observed in the PL spectra of freshly prepared LB films for which signatures of TeO<sub>2</sub> are absent in the XPS spectra. On the other hand, significant blue-shift and spectral broadening are observed for the fresh samples

including those prepared by drop-casting. These significant spectral changes cannot be attributed to a difference of the refractive index of the solution and the film as this is not the case for the CdSe/ZnS and CdSeS/ZnS QDs. The spectral blue-shift and broadening can be indicative of subtle changes (e.g., increased defect concentration) on the surface of the nanocrystals. Defect concentration is known to speed up atomic interdiffusion.<sup>60</sup> In addition, the diffusion process can be facilitated by interfacial interactions (QD–QD and QD–substrate) that can create chemical potential gradient and may also lower the activation energy barrier of the diffusion process.<sup>60</sup> Under this favorable condition, the strain energy cost that is specified in eq 1 can be sufficient to drive the atomic interdiffusion process.

Depending on the favorability of the thermodynamic and kinetic conditions, the atomic interdiffusion can lead to the formation of CdSe/CdS core/shell or alloyed CdSeS nanocrystals coated with ZnTe as mentioned above. Considering all the samples we have prepared and analyzed, it is clear that the relative intensity of the peak at 660 nm (due to CdSeS QDs) is higher than that of the 630 nm (due to CdSe/CdS QDs). In fact, in some areas, the emission peak at 660 nm is the only prominent peak observed in the visible region as demonstrated by the red line in Figure 7. This observation may suggest that the conditions are favorable to result in complete miscibility to form alloyed CdSeS QDs. It should also be noted that the fact that the emission peak at ~820 nm (resonance of the original alloyed nanocrystals on the substrate) is observed in almost all areas for all the samples may suggest that only some of the alloyed QDs (that are metastable) transform into more stable crystal composition.

Consistent with the above-proposed mechanism, the 630 nm emission wavelength and 23 nm fwhm are in agreement with corresponding spectral characteristics of the CdSe/ZnS QDs with similar core diameter as confirmed in a separate measurement. On the other hand, if all the S atom of the ZnS shell diffuse into the crystal to fill in the lattice sites of Te, the resulting CdSeS nanocrystal is expected to emit around 660 nm which is in agreement with the longest emission wavelength of commercially available CdSeS/ZnS nanocrystals, which we have characterized separately. The 660 nm wavelength is also within the range of CdTe QD emission wavelengths. However, for CdTe QDs to emit at 660 nm, the diameter has to be ~4.5 nm, which is significantly larger than the diameter (~3.4 nm) that can be obtained from the transformation of individual CdSe<sub>0.85</sub>Te<sub>0.15</sub> nanocrystals to the binary CdSe and CdTe nanocrystals. In addition, this crystal transformation requires drastic change of lattice structures that is not plausible. Transformation of individual alloyed nanocrystals into type II QDs may also be considered as an alternative mechanism, which is less likely for the following reasons. This mechanism will result either in CdSe/CdTe/ZnS or CdTe/CdSe/ZnS core/shell/shell type II QDs. The former does not emit because of the lower band gap energy of CdTe shell than the core.<sup>43</sup> The latter is expected to emit at much longer wavelength than 660 nm, and the line width would be broader than that of the observed peak.<sup>68</sup>

## CONCLUSION

In summary, using near-infrared CdSeTe/ZnS QDs as model systems, we have demonstrated the transformation of metastable alloyed nanocrystals to more stable forms. When the ZnS coated alloyed CdSeTe QDs with 840 nm emission

wavelength and 75 nm spectral line width are self-assembled on water and transferred to a silica substrate using a Langmuir–Blodgett procedure, two new prominent sharp emission peaks are observed at ~630 and ~660 nm emission wavelengths that have ~23 and ~39 nm fwhm's, respectively. On the basis of analysis of the crystal composition using X-ray photoelectron, we conclude that the relative concentration of Te atoms on the surface of the nanocrystals has increased significantly, which clearly indicates the diffusion of Te atoms from the core to the shell. This outward diffusion of Te atoms can then initiate inward diffusion of S, which can lead to the formation of either CdSe/CdS or CdSeS quantum dots. Based on size analysis, these new nanocrystals are expected to emit at 630 and 660 nm wavelengths, respectively. Since no spectral changes have been observed for the QDs as they are assembled on the water surface, surface defect concentration and interfacial interactions that create chemical potential gradient and lower the activation energy barrier of the diffusion process are suggested as possible mechanisms that facilitate the outward diffusion of Te atom to minimize the strain energy cost. This work emphasizes the importance of postsynthesis characterization of alloyed nanocrystals, which have potential applications in biological imaging and optoelectronic devices.

## ASSOCIATED CONTENT

### Supporting Information

The Supporting Information is available free of charge on the ACS Publications website at DOI: 10.1021/acs.jpcc.6b02988.

Spatiospectral images of PL intensity (Figure S1) and photographic view of drop-casted quantum dot film and the corresponding PL spectra (Figure S2) (PDF)

## AUTHOR INFORMATION

### Corresponding Author

\*(T.G.H.) E-mail [habteyes@unm.edu](mailto:habteyes@unm.edu); phone 505-272-7504.

### Notes

The authors declare no competing financial interest.

## ACKNOWLEDGMENTS

This research has been supported by the U.S. Air Force Office of Scientific Research, Grant No. FA9550-15-1-0305, and the Air Force Research Laboratory, Grant No. FA9453-15-1-0078.

## REFERENCES

- (1) Michalet, X.; Pinaud, F. F.; Bentolila, L. A.; Tsay, J. M.; Doose, S.; Li, J. J.; Sundaresan, G.; Wu, A. M.; Gambhir, S. S.; Weiss, S. Quantum Dots for Live Cells, in Vivo Imaging, and Diagnostics. *Science* **2005**, *307*, 538–544.
- (2) Luther, J. M.; Law, M.; Beard, M. C.; Song, Q.; Reese, M. O.; Ellingson, R. J.; Nozik, A. J. Schottky Solar Cells Based on Colloidal Nanocrystal Films. *Nano Lett.* **2008**, *8*, 3488–3492.
- (3) Ma, W.; Luther, J. M.; Zheng, H. M.; Wu, Y.; Alivisatos, A. P. Photovoltaic Devices Employing Ternary PbS<sub>x</sub>Se<sub>1-x</sub> Nanocrystals. *Nano Lett.* **2009**, *9*, 1699–1703.
- (4) Chuang, C. H. M.; Brown, P. R.; Bulovic, V.; Bawendi, M. G. Improved Performance and Stability in Quantum Dot Solar Cells through Band Alignment Engineering. *Nat. Mater.* **2014**, *13*, 796–801.
- (5) Konstantatos, G.; Howard, L.; Fischer, A.; Hoogland, S.; Clifford, J.; Klem, E.; Levina, L.; Sargent, E. H. Ultrasensitive Solution-Cast Quantum Dot Photodetectors. *Nature* **2006**, *442*, 180–183.
- (6) Im, S. H.; Chang, J. A.; Kim, S. W.; Seok, S. I. Near-Infrared Photodetection Based on PbS Colloidal Quantum Dots/Organic Hole Conductor. *Org. Electron.* **2010**, *11*, 696–699.

- (7) Wang, H. W.; Li, Z. X.; Fu, C. J.; Yang, D.; Zhang, L.; Yang, S. Y.; Zou, B. S. Solution-Processed PbSe Colloidal Quantum Dot-Based Near-Infrared Photodetector. *IEEE Photonics Technol. Lett.* **2015**, *27*, 612–615.
- (8) Katari, J. E. B.; Colvin, V. L.; Alivisatos, A. P. X-Ray Photoelectron Spectroscopy of CdSe Nanocrystals with Applications to Studies of the Nanocrystal Surface. *J. Phys. Chem.* **1994**, *98*, 4109–4117.
- (9) Nirmal, M.; Dabbousi, B. O.; Bawendi, M. G.; Macklin, J. J.; Trautman, J. K.; Harris, T. D.; Brus, L. E. Fluorescence Intermittency in Single Cadmium Selenide Nanocrystals. *Nature* **1996**, *383*, 802–804.
- (10) Cordero, S. R.; Carson, P. J.; Estabrook, R. A.; Strouse, G. F.; Buratto, S. K. Photo-Activated Luminescence of CdSe Quantum Dot Monolayers. *J. Phys. Chem. B* **2000**, *104*, 12137–12142.
- (11) Aldana, J.; Wang, Y. A.; Peng, X. Photochemical Instability of CdSe Nanocrystals Coated by Hydrophilic Thiols. *J. Am. Chem. Soc.* **2001**, *123*, 8844–8850.
- (12) Wang, X.; Zhang, J.; Nazzal, A.; Xiao, M. Photo-Oxidation-Enhanced Coupling in Densely Packed CdSe Quantum-Dot Films. *Appl. Phys. Lett.* **2003**, *83*, 162–164.
- (13) Kimura, J.; Uematsu, T.; Maenosono, S.; Yamaguchi, Y. Photoinduced Fluorescence Enhancement in CdSe/ZnS Quantum Dot Submonolayers Sandwiched between Insulating Layers: Influence of Dot Proximity. *J. Phys. Chem. B* **2004**, *108*, 13258–13264.
- (14) Nazzal, A. Y.; Wang, X.; Qu, L.; Yu, W.; Wang, Y.; Peng, X.; Xiao, M. Environmental Effects on Photoluminescence of Highly Luminescent CdSe and CdSe/ZnS Core/Shell Nanocrystals in Polymer Thin Films. *J. Phys. Chem. B* **2004**, *108*, 5507–5515.
- (15) Müller, J.; Lupton, J. M.; Rogach, A. L.; Feldmann, J.; Talapin, D. V.; Weller, H. Air-Induced Fluorescence Bursts from Single Semiconductor Nanocrystals. *Appl. Phys. Lett.* **2004**, *85*, 381–383.
- (16) Gia-Wei, S.; Wan-Zhen, L.; Shu, I. J.; Ji-Lin, S.; James Cheng-An, L.; Chang, W. H.; Ruoh-Chyu, R.; Wu Ching, C. Photoluminescence of Colloidal CdSe/ZnS Quantum Dots under Oxygen Atmosphere. *IEEE Trans. Nanotechnol.* **2005**, *4*, 632–636.
- (17) Uematsu, T.; Maenosono, S.; Yamaguchi, Y. Photoinduced Fluorescence Enhancement in Mono- and Multilayer Films of CdSe/ZnS Quantum Dots: Dependence on Intensity and Wavelength of Excitation Light. *J. Phys. Chem. B* **2005**, *109*, 8613–8618.
- (18) Pechstedt, K.; Whittle, T.; Baumberg, J.; Melvin, T. Photoluminescence of Colloidal CdSe/ZnS Quantum Dots: The Critical Effect of Water Molecules. *J. Phys. Chem. C* **2010**, *114*, 12069–12077.
- (19) Bao, H.; Gong, Y.; Li, Z.; Gao, M. Enhancement Effect of Illumination on the Photoluminescence of Water-Soluble CdTe Nanocrystals: Toward Highly Fluorescent CdTe/CdS Core–Shell Structure. *Chem. Mater.* **2004**, *16*, 3853–3859.
- (20) Zhang, Y.; He, J.; Wang, P. N.; Chen, J. Y.; Lu, Z. J.; Lu, D. R.; Guo, J.; Wang, C. C.; Yang, W. L. Time-Dependent Photoluminescence Blue-Shift of the Quantum Dots in Living Cells: Effect of Oxidation by Singlet Oxygen. *J. Am. Chem. Soc.* **2006**, *128*, 13396–13401.
- (21) Lobo, A.; Borchert, H.; Talapin, D. V.; Weller, H.; Möller, T. Surface Oxidation of CdTe Nanocrystals - a High Resolution Core-Level Photoelectron Spectroscopy Study. *Colloids Surf., A* **2006**, *286*, 1–7.
- (22) Patra, S.; Samanta, A. Effect of Capping Agent and Medium on Light-Induced Variation of the Luminescence Properties of CdTe Quantum Dots: A Study Based on Fluorescence Correlation Spectroscopy, Steady State and Time-Resolved Fluorescence Techniques. *J. Phys. Chem. C* **2014**, *118*, 18187–18196.
- (23) Peterson, J. J.; Krauss, T. D. Photobrightening and Photodarkening in PbS Quantum Dots. *Phys. Chem. Chem. Phys.* **2006**, *8*, 3851–3856.
- (24) Luther, J. M.; Gao, J. B.; Lloyd, M. T.; Semonin, O. E.; Beard, M. C.; Nozik, A. J. Stability Assessment on a 3% Bilayer PbS/ZnO Quantum Dot Heterojunction Solar Cell. *Adv. Mater.* **2010**, *22*, 3704–3707.
- (25) Ihly, R.; Tolentino, J.; Liu, Y.; Gibbs, M.; Law, M. The Photothermal Stability of PbS Quantum Dot Solids. *ACS Nano* **2011**, *5*, 8175–8186.
- (26) Sun, X. L.; Dai, R.; Chen, J. J.; Zhou, W.; Wang, T. Y.; Kost, A. R.; Tsung, C. K.; An, Z. S. Enhanced Thermal Stability of Oleic-Acid-Capped PbS Quantum Dot Optical Fiber Amplifier. *Opt. Express* **2014**, *22*, 519–524.
- (27) Cant, D. J. H.; Syres, K. L.; Lunt, P. J. B.; Radtke, H.; Treacy, J.; Thomas, P. J.; Lewis, E. A.; Haigh, S. J.; O'Brien, P.; Schulte, K.; Bondino, F.; Magnano, E.; Flavell, W. R. Surface Properties of Nanocrystalline PbS Films Deposited at the Water-Oil Interface: A Study of Atmospheric Aging. *Langmuir* **2015**, *31*, 1445–1453.
- (28) Dai, Q. Q.; Wang, Y. N.; Zhang, Y.; Li, X. B.; Li, R. W.; Zou, B.; Seo, J.; Wang, Y. D.; Liu, M. H.; Yu, W. W. Stability Study of PbSe Semiconductor Nanocrystals over Concentration, Size, Atmosphere, and Light Exposure. *Langmuir* **2009**, *25*, 12320–12324.
- (29) Sykora, M.; Koposov, A. Y.; McGuire, J. A.; Schulze, R. K.; Tretiak, O.; Pietryga, J. M.; Klimov, V. I. Effect of Air Exposure on Surface Properties, Electronic Structure, and Carrier Relaxation in PbSe Nanocrystals. *ACS Nano* **2010**, *4*, 2021–2034.
- (30) Zhang, Z. L.; Yang, J. F.; Wen, X. M.; Yuan, L.; Shrestha, S.; Stride, J. A.; Conibeer, G. J.; Patterson, R. J.; Huang, S. J. Effect of Halide Treatments on PbSe Quantum Dot Thin Films: Stability, Hot Carrier Lifetime, and Application to Photovoltaics. *J. Phys. Chem. C* **2015**, *119*, 24149–24155.
- (31) Hines, M. A.; Guyot-Sionnest, P. Synthesis and Characterization of Strongly Luminescing ZnS-Capped CdSe Nanocrystals. *J. Phys. Chem.* **1996**, *100*, 468–471.
- (32) Dabbousi, B. O.; Rodriguez-Viejo, J.; Mikulec, F. V.; Heine, J. R.; Mattoussi, H.; Ober, R.; Jensen, K. F.; Bawendi, M. G. (CdSe)/ZnS Core–Shell Quantum Dots: Synthesis and Characterization of a Size Series of Highly Luminescent Nanocrystallites. *J. Phys. Chem. B* **1997**, *101*, 9463–9475.
- (33) Peng, X. G.; Schlamp, M. C.; Kadavanich, A. V.; Alivisatos, A. P. Epitaxial Growth of Highly Luminescent CdSe/CdS Core/Shell Nanocrystals with Photostability and Electronic Accessibility. *J. Am. Chem. Soc.* **1997**, *119*, 7019–7029.
- (34) Jiong, M.; Ji-Yao, C.; Jia, G.; Chang-Chun, W.; Wu-Li, Y.; Nai-Ho, C.; Pei-Nan, W. Improvement of the Photostability of Thiol-Capped CdTe Quantum Dots in Aqueous Solutions and in Living Cells by Surface Treatment. *Nanotechnology* **2006**, *17*, 5875–5881.
- (35) Dai, Q.; Zhang, Y.; Wang, Y.; Wang, Y.; Zou, B.; Yu, W. W.; Hu, M. Z. Ligand Effects on Synthesis and Post-Synthetic Stability of PbSe Nanocrystals. *J. Phys. Chem. C* **2010**, *114*, 16160–16167.
- (36) Bae, W. K.; Joo, J.; Padilha, L. A.; Won, J.; Lee, D. C.; Lin, Q.; Koh, W.-k.; Luo, H.; Klimov, V. I.; Pietryga, J. M. Highly Effective Surface Passivation of PbSe Quantum Dots through Reaction with Molecular Chlorine. *J. Am. Chem. Soc.* **2012**, *134*, 20160–20168.
- (37) Zherebetskyy, D.; Scheele, M.; Zhang, Y. J.; Bronstein, N.; Thompson, C.; Britt, D.; Salmeron, M.; Alivisatos, P.; Wang, L. W. Hydroxylation of the Surface of PbS Nanocrystals Passivated with Oleic Acid. *Science* **2014**, *344*, 1380–1384.
- (38) Woo, J. Y.; Ko, J. H.; Song, J. H.; Kim, K.; Choi, H.; Kim, Y. H.; Lee, D. C.; Jeong, S. Ultrastable PbSe Nanocrystal Quantum Dots Via in Situ Formation of Atomically Thin Halide Adlayers on PbSe(100). *J. Am. Chem. Soc.* **2014**, *136*, 8883–8886.
- (39) Alivisatos, A. P. Semiconductor Clusters, Nanocrystals, and Quantum Dots. *Science* **1996**, *271*, 933–937.
- (40) Weissleder, R. A Clearer Vision for in Vivo Imaging. *Nat. Biotechnol.* **2001**, *19*, 316–317.
- (41) Frangioni, J. V. In Vivo Near-Infrared Fluorescence Imaging. *Curr. Opin. Chem. Biol.* **2003**, *7*, 626–634.
- (42) Chen, A.-B.; Sher, A. *Semiconductor Alloys*; Springer: 1995.
- (43) Bailey, R. E.; Nie, S. M. Alloyed Semiconductor Quantum Dots: Tuning the Optical Properties without Changing the Particle Size. *J. Am. Chem. Soc.* **2003**, *125*, 7100–7106.
- (44) Swafford, L. A.; Weigand, L. A.; Bowers, M. J.; McBride, J. R.; Rapaport, J. L.; Watt, T. L.; Dixit, S. K.; Feldman, L. C.; Rosenthal, S. J. Homogeneously Alloyed CdS<sub>x</sub>Se<sub>1-x</sub> Nanocrystals: Synthesis,

Characterization, and Composition/Size-Dependent Band Gap. *J. Am. Chem. Soc.* **2006**, *128*, 12299–12306.

(45) Jang, E.; Jun, S.; Pu, L. High Quality CdSeS Nanocrystals Synthesized by Facile Single Injection Process and Their Electroluminescence. *Chem. Commun.* **2003**, 2964–2965.

(46) Jiang, W.; Singhal, A.; Zheng, J. N.; Wang, C.; Chan, W. C. W. Optimizing the Synthesis of Red- to Near-IR-Emitting CdS-Capped CdTe<sub>x</sub>Se<sub>1-x</sub> Alloyed Quantum Dots for Biomedical Imaging. *Chem. Mater.* **2006**, *18*, 4845–4854.

(47) Allen, P. M.; Bawendi, M. G. Ternary I-III-VI Quantum Dots Luminescent in the Red to Near-Infrared. *J. Am. Chem. Soc.* **2008**, *130*, 9240–9241.

(48) Liang, G. X.; Li, L. L.; Liu, H. Y.; Zhang, J. R.; Burda, C.; Zhu, J. J. Fabrication of Near-Infrared-Emitting CdSeTe/ZnS Core/Shell Quantum Dots and Their Electrogenenerated Chemiluminescence. *Chem. Commun.* **2010**, *46*, 2974–2976.

(49) Kim, S.; Kang, M.; Heo, J. H.; Noh, J. H.; Im, S. H.; Seok, S. I.; Kim, S. W. Fabrication of CuInTe<sub>2</sub> and CuInTe<sub>2-x</sub>Se<sub>x</sub> Ternary Gradient Quantum Dots and Their Application to Solar Cells. *ACS Nano* **2013**, *7*, 4756–4763.

(50) MacDonald, B. I.; Martucci, A.; Rubanov, S.; Watkins, S. E.; Mulvaney, P.; Jasieniak, J. J. Layer-by-Layer Assembly of Sintered CdSe<sub>x</sub>Te<sub>1-x</sub> Nanocrystal Solar Cells. *ACS Nano* **2012**, *6*, 5995–6004.

(51) Liu, J. Z.; Zunger, A. Thermodynamic States and Phase Diagrams for Bulk-Incoherent, Bulk-Coherent, and Epitaxially-Coherent Semiconductor Alloys: Application to Cubic (Ga,In)N. *Phys. Rev. B: Condens. Matter Mater. Phys.* **2008**, *77*, 205201.

(52) Liu, J. Z.; Trimarchi, G.; Zunger, A. Strain-Minimizing Tetrahedral Networks of Semiconductor Alloys. *Phys. Rev. Lett.* **2007**, *99*, 145501.

(53) Iyer, S. S.; Legoues, F. K. Thermal Relaxation of Pseudomorphic Si-Ge Superlattices by Enhanced Diffusion and Dislocation Multiplication. *J. Appl. Phys.* **1989**, *65*, 4693–4698.

(54) Kuan, T. S.; Iyer, S. S. Strain Relaxation and Ordering in SiGe Layers Grown on (100), (111), and (110) Si Surfaces by Molecular-Beam Epitaxy. *Appl. Phys. Lett.* **1991**, *59*, 2242–2244.

(55) Ryu, S. W.; Kim, I.; Choe, B. D.; Jeong, W. G. The Effect of Strain on the Interdiffusion in InGaAs/GaAs Quantum-Wells. *Appl. Phys. Lett.* **1995**, *67*, 1417–1419.

(56) Leon, R.; Kim, Y.; Jagadish, C.; Gal, M.; Zou, J.; Cockayne, D. J. H. Effects of Interdiffusion on the Luminescence of InGaAs/GaAs Quantum Dots. *Appl. Phys. Lett.* **1996**, *69*, 1888–1890.

(57) Gillin, W. P.; Dunstan, D. J. Strain and Interdiffusion in Semiconductor Heterostructures. *Phys. Rev. B: Condens. Matter Mater. Phys.* **1994**, *50*, 7495–7498.

(58) Koo, B.; Korgel, B. A. Coalescence and Interface Diffusion in Linear CdTe/CdSe/CdTe Heterojunction Nanorods. *Nano Lett.* **2008**, *8*, 2490–2496.

(59) Li, L. L.; Chen, Y.; Lu, Q.; Ji, J.; Shen, Y. Y.; Xu, M.; Fei, R.; Yang, G. H.; Zhang, K.; Zhang, J. R.; Zhu, J. J. Electrochemiluminescence Energy Transfer-Promoted Ultrasensitive Immunoassay Using Near-Infrared-Emitting CdSeTe/CdS/ZnS Quantum Dots and Gold Nanorods. *Sci. Rep.* **2013**, *3*, 1529.

(60) Kittel, C. *Introduction of Solid State Physics*, 8th ed.; John Wiley & Sons, Inc.: New York, 2005.

(61) Xu, J. M.; Ji, X. J.; Gattas-Asfura, K. M.; Wang, C. S.; Leblanc, R. M. Langmuir and Langmuir-Blodgett Films of Quantum Dots. *Colloids Surf., A* **2006**, *284*, 35–42.

(62) Babentsov, V.; Sizov, F. Defects in Quantum Dots of IIb-VI Semiconductors. *Opto-Electron. Rev.* **2008**, *16*, 208–225.

(63) Baker, D. R.; Kamat, P. V. Tuning the Emission of CdSe Quantum Dots by Controlled Trap Enhancement. *Langmuir* **2010**, *26*, 11272–11276.

(64) Borchert, H.; Talapin, D. V.; McGinley, C.; Adam, S.; Lobo, A.; de Castro, A. R. B.; Möller, T.; Weller, H. High Resolution Photoemission Study of CdSe and CdSe/ZnS Core-Shell Nanocrystals. *J. Chem. Phys.* **2003**, *119*, 1800–1807.

(65) Winkler, U.; Eich, D.; Chen, Z. H.; Fink, R.; Kulkarni, S. K.; Umbach, E. Detailed Investigation of CdS Nanoparticle Surfaces by

High-Resolution Photoelectron Spectroscopy. *Chem. Phys. Lett.* **1999**, *306*, 95–102.

(66) Powell, C. J.; Jablonski, A. Surface Sensitivity of X-Ray Photoelectron Spectroscopy. *Nucl. Instrum. Methods Phys. Res., Sect. A* **2009**, *601*, 54–65.

(67) Powell, C. J.; Jablonski, A. *Nist Electron Effective-Attenuation-Length Database - Version 1.3*; National Institute of Standards and Technology: Gaithersburg, MD, 2011.

(68) Kim, S.; Fisher, B.; Eisler, H. J.; Bawendi, M. Type-II Quantum Dots: CdTe/CdSe (Core/Shell) and CdSe/ZnTe (Core/Shell) Heterostructures. *J. Am. Chem. Soc.* **2003**, *125*, 11466–11467.

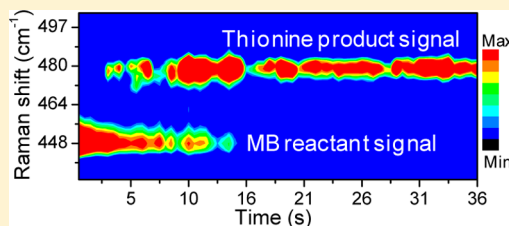
# Plasmon-Enhanced Resonant Excitation and Demethylation of Methylene Blue

Tefera E. Tesema, Bijesh Kafle, Meron G. Tadesse, and Terefe G. Habteyes\*

Departments of Chemistry and Chemical Biology, and Center for High Technology Materials, University of New Mexico, Albuquerque, New Mexico 87131, United States

## S Supporting Information

**ABSTRACT:** Using methylene blue (MB) as a model system, we demonstrate surface plasmon-enhanced resonant excitation that leads to N-demethylation reaction under visible light irradiation ( $\lambda = 633$  nm) at low photon flux. The chemical changes are monitored by detecting the vibrational signatures of the reactant and product species in situ using surface-enhanced Raman scattering (SERS) spectroscopy. Drastic temporal evolution of SERS spectra has been observed upon continuous irradiation. While the SERS spectra acquired immediately after irradiation are the same as the Raman spectrum of MB solid powder, the spectra recorded a few seconds later are remarkably similar to that of thionine solid powder, indicating N-demethylation of MB. No demethylation reaction has been observed under resonant excitation ( $\lambda = 633$  nm) of MB adsorbed on nonplasmonic surfaces. Similarly, excitations of plasmon resonances at 532 and 808 nm wavelengths that do not overlap with the MB electronic transition do not lead to transformation of MB to thionine. The reaction mechanism is discussed in terms of resonant excitation of MB and hot electron transfer to adsorbed species. Considering that both MB and thionine have large SERS signal due to the combination of resonance Raman and electromagnetic enhancement effects that provide high detection sensitivity, we suggest that this demethylation reaction serves as a convenient model system for future mechanistic studies.



## INTRODUCTION

Soon after the discovery of surface-enhanced Raman scattering (SERS) spectroscopy,<sup>1,2</sup> surface-enhanced photochemistry was proposed theoretically<sup>3,4</sup> and demonstrated experimentally.<sup>5–11</sup> In particular, the work by Moskovits and co-workers revealed the ambiguity in the interpretations of earlier SERS data due to vibrational peaks of reaction products that could be wrongly assigned to the reactants.<sup>12</sup> More recent examples of plasmon driven photochemical reactions include the azo-coupling of self-assembled *para*-aminothiophenol (PATP),<sup>13–15</sup> ethylene epoxidation,<sup>16</sup> dissociation of hydrogen molecules,<sup>17</sup> and conversion of aldehydes to esters.<sup>18</sup> The dual action of surface plasmons to enhance Raman scattering and photochemistry provides a unique technical convenience for investigating surface chemistry using SERS as a highly sensitive in situ vibrational spectroscopy.<sup>19–21</sup> However, there are limited model reaction systems, notably the conversion of self-assembled PATP to *p,p'*-dimercaptazobenzene (DMAB) that can be studied by monitoring the vibrational bands of reactants and products using SERS. In addition, studies of plasmon driven photochemical reactions to date have been based on excitation wavelengths that match the plasmon resonances but not the molecular resonances. Resonant electronic excitation where the excitation wavelength overlaps with the molecular and plasmon resonances provides high SERS detection sensitivity due to the combination of resonance Raman and electromagnetic enhancement effects.<sup>22</sup>

In this work, we discuss the first systematic study on the N-demethylation of MB initiated by plasmon-enhanced resonant excitation of MB at 633 nm laser wavelength. We propose that this demethylation reaction would be an excellent model system for mechanistic studies in plasmon driven photochemistry because of the high detection sensitivity and the availability of background information. The photocatalytic degradation of MB has been investigated using different catalytic materials such as TiO<sub>2</sub>,<sup>23</sup> Au–TiO<sub>2</sub> composite,<sup>24</sup> Cr–Ti binary oxide,<sup>24</sup> and Ag–In–Ni–S nanocomposites.<sup>25</sup> The solution phase excited-state dynamics of MB is well documented.<sup>26,27</sup> MB is also a common model system in SERS related studies<sup>28–33</sup> as well as in strong exciton–plasmon coupling,<sup>34</sup> and yet systematic investigation of its plasmon driven surface photochemistry is lacking. Here, we demonstrate that irradiation of MB adsorbed on resonant plasmonic gold nanorods (AuNRs) with visible light induces chemical transformation of MB as it is revealed in the dramatic temporal evolution of the SERS spectra. While the vibrational signatures observed immediately after irradiation are the same as that of MB solid powder, the spectra recorded after a few seconds are similar to that of thionine solid powder, indicating a demethylation reaction at low incident photon flux.

Received: January 26, 2017

Revised: March 11, 2017

Published: March 15, 2017

## ■ EXPERIMENTAL SECTION

**Sample Preparation.** Gold film (AuF) of thickness  $\sim 40$  nm was deposited on oxide coated silicon wafer using electron-beam evaporation. Methylene blue (obtained from Sigma-Aldrich) was immobilized on the gold film by keeping the substrate overnight ( $\sim 8$  h) in freshly prepared  $1.5 \times 10^{-5}$  mol  $L^{-1}$  MB in ethanol solution. As the substrate is pulled out of the solution, it was washed with ethanol so that loosely attached molecules are removed from the substrate. The substrate was then dried by blowing dry  $N_2$  gas. An aqueous solution of gold nanorods (AuNRs) with cetyltrimethylammonium bromide (CTAB) stabilizing surface ligand was obtained from Nanopartz, Inc. The excess CTAB surfactant was removed through two rounds of centrifugation (at 5000 rpm for 5 min) and disposal of the supernatant solution. The AuNRs were then resuspended in ultrapure water and deposited on MB-functionalized AuF by drop-casting and allowing drying at ambient condition. This sample preparation sandwiches MB between the AuF and the AuNRs, where the electric field is localized.<sup>35</sup>

While the AuF-MB-AuNR sample provides clarity about the location of the molecule, the strong dipole–metal surface interaction does not allow us to tune the plasmon resonance outside the MB absorption band regardless of the size and shape of the plasmonic nanoantennas. As a result, for studying the role of resonant excitation of MB, the molecule was adsorbed on AuNRs by replacing CTAB through the following procedures. First, the excess CTAB was removed as described above by centrifuging 1.8 mL of diluted aqueous AuNR solution and removing the supernatant solution. The solid residue was then resuspended in 1.0 mL of  $1.5 \times 10^{-5}$  M MB in ethanol solution and kept overnight. To remove the MB molecules that were not adsorbed to the AuNR surfaces, the solution was centrifuged, and the supernatant solution was removed. The solid residue was then resuspended in ethanol and drop-casted on oxide coated silicon wafer.

**Optical and Topographic Characterization.** The absorption spectra of MB were recorded using a UV–vis spectrometer (Shimadzu UV-2450) by dissolving MB in ethanol and adsorbing on acrylic cuvette. A dilute solution of MB ( $1.5 \times 10^{-5}$  M) in ethanol was kept in the cuvette for several hours to achieve the adsorption, after which the solution was discarded and the absorbance from the adsorbate was recorded. All other optical measurements (dark-field scattering, SERS and fluorescence) on the solid samples were carried out using a modified inverted dark-field microscope (Olympus GX51F5) illuminating and collecting through a dark-field objective (0.9 NA, 100 $\times$ ). For the dark-field scattering measurement, the sample is excited with a 100 W halogen lamp white light source. The SERS measurements are performed by exciting the sample with laser line that overlaps with both molecular and plasmon resonances ( $\lambda = 633$  nm) and with laser lines that overlap only with the plasmon resonance ( $\lambda = 532$  or 808 nm). More than 90% of the light collected from the sample through the objective is directed to the spectrometer (IsoPlane Spectrograph of Princeton Instruments) that uses thermoelectrically cooled ( $-75$  °C) and back-illuminated deep depletion CCD camera, while the remaining signal is directed to the Olympus UC30 camera that is attached to the microscope for imaging the dark-field scattering of the sample. This optical setup allows us to obtain the dark-field scattering and SERS data from a fixed area using

the same objective simply by switching the excitation source from white light source to laser line, while all of the optical components and the sample remain stationary. The comparison of Stokes and anti-Stokes Raman intensities was carried out using our atomic force/near-field microscope that has been described elsewhere,<sup>36,37</sup> but the same spectrometer mentioned above is used for detection. The fluorescence of MB solution was measured using a home-built setup where a 0.7 NA objective is used for illuminating the solution contained in a cuvette. The fluorescence light is collected through the same objective and directed to the spectrometer mentioned above.

## ■ RESULTS AND DISCUSSION

The optical measurement was initiated on AuF-MB-AuNR samples at ambient conditions. The orientation of the molecules is believed to be parallel to the substrate,<sup>38,39</sup> and the gap between the AuNR and the AuF is estimated as  $\sim 1$  nm after accounting for the MB and the CTAB surface ligands on the AuNRs. The interaction of the AuNR with the AuF creates an enhanced field that is localized in the AuF–AuNR gap.<sup>35,40</sup> The spectral overlap of the 633 nm laser line with the molecular and plasmon resonances is illustrated in Figure 1. The absorption peak of MB adsorbed on acrylic surface (blue line in Figure 1a) has blue-shifted by about 5 nm with respect to the absorption peak in solution (black line), which is consistent with a previous report.<sup>41</sup> Similarly, the fluorescence (FL) peak (green line) of MB adsorbed on silica surface has blue-shifted by about 15 nm with respect to that of MB in solution phase (red line). Depending on the strength of the surface–molecule interaction, a similar blue-shift is expected for MB adsorbed on gold surfaces, improving the overlap of the absorption band with the 633 nm excitation wavelength. We note that no FL signal was detected for MB adsorbed on the AuF as shown by the pink line in Figure 1a due to effective quenching of excitation energy of the molecule by the metal surface.

In solution, the absorption spectrum of the AuNRs peaks at  $\sim 680$  nm (black line in Figure 1b). A representative single particle spectrum of a gold nanorod on gold film is shown by the cyan line in Figure 1b. However, all of the studies presented here are based on aggregates of the AuNRs that have very broad resonances as shown by the red curve in Figure 1b. Representative dark-field scattering and topographic images are shown in Figures S1–S3. Comparing the black spectrum in Figure 1a with the red spectrum in Figure 1b, it can be seen that the entire absorption band of MB lies within the broad plasmon resonance of the AuNR aggregates. This spectral overlap between the molecular and plasmon resonances provides enormous enhancement of Raman scattering for monitoring the photochemistry using SERS for in situ detection of chemical transformation.

The intensity map of a series of 80 SERS spectra (acquired continuously with 500 ms acquisition time and 17 ms interval) is displayed in Figure 2a. It can be seen that new vibrational bands have appeared a few seconds after the excitation laser is on. In particular, a new strong band appears at  $479\text{ cm}^{-1}$  within a few seconds upon continuous irradiation. The temporal evolution can be observed more clearly by comparing the first spectrum (recorded within 0.5 s acquisition time immediately after the excitation light is on) and the spectrum acquired after  $\sim 5$  s as shown in Figure 2b with blue and red lines, respectively. The first spectrum (blue line) is essentially the same as the spectrum of the MB solid powder (black line). On the other hand, new vibrational bands that cannot be attributed to MB

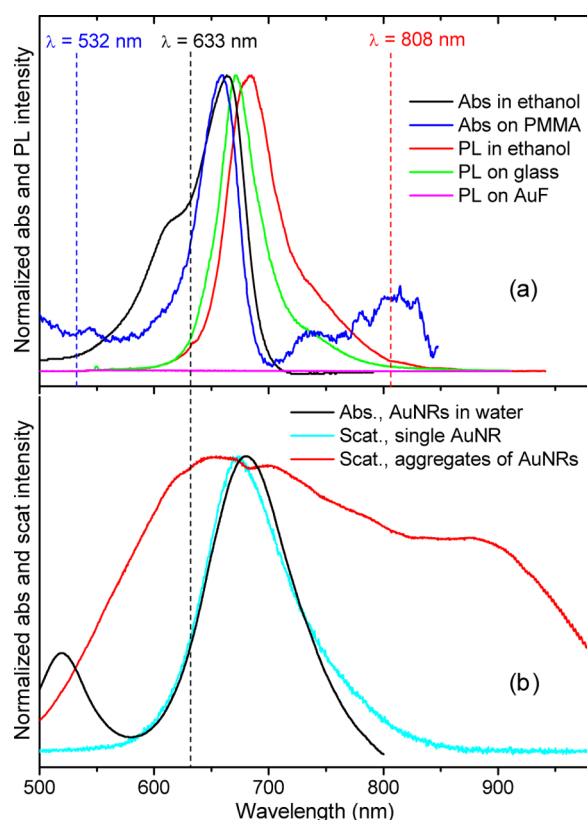


**Figure 1.** Spectral overlap of the molecular and plasmon resonances with respect to the laser lines (dashed vertical lines). (a) The absorption spectrum of  $10^{-6}$  M methylene blue in ethanol solution (black line) and the corresponding fluorescence (FL) spectrum (red line). The blue line is the absorption spectrum of MB adsorbed on the inside wall of acrylic [poly(methyl methacrylate, PMMA)] cuvette. With respect to the solution phase FL (red line), the FL peak of MB adsorbed on a silica substrate (green line) is blue-shifted by about 15 nm. (b) The absorption (black line) and scattering (cyan and red lines) of AuNRs with nominal diameter of 40 nm and length 92 nm. The scattering spectra of a single (cyan line) and aggregates (red line) of AuNRs are obtained as the nanorods are adsorbed on MB treated gold film.

are observed in the red spectrum. In addition to the strong peak at  $479\text{ cm}^{-1}$ , several other new peaks are observed as marked by the vertical dashed lines. With the exception of some residual vibrational peaks of MB, the SERS spectra acquired after some time delay are remarkably similar to the Raman spectrum of thionine solid powder (green line). We note that the regular Raman spectrum of thionine solid powder shown in Figure 2b (green line) is in good agreement with published data,<sup>42</sup> and with the corresponding SERS spectra of thionine as compared in Figure S4.

The  $479\text{ cm}^{-1}$  band was observed in electrochemical experiments by Nicolai and Rubim, and was attributed to thiazine ring in-plane bending of MB adsorbed on the electrode as a monomer.<sup>30</sup> This assignment was based on the observation that the relative intensity of the band decreases with increasing number of multilayer on the silver electrode.<sup>30</sup> However, this trend is also consistent with the conversion of MB to thionine because only the molecules that are in very close proximity to the metal surface are expected to be transformed as the mechanism may involve surface–molecule interaction. In our measurement, a large number of additional peaks are observed that have not been observed before, and all of these bands

match the vibrational bands of thionine perfectly as marked by the vertical dashed lines in Figure 2b. In particular, the peak at  $804\text{ cm}^{-1}$ , which has been assigned to  $\text{NH}_2$  rocking vibrational motion of thionine by Hutchinson and Hester,<sup>42</sup> cannot be attributed to any vibrational features of methylene blue. Our spectral assignment is also supported by theoretical calculation as shown in Figure S5. Therefore, we attribute the spectral evolution to N-demethylation reaction that converts methylene blue to thionine. This plasmon driven N-demethylation reaction is consistent with the observation in the photocatalytic decomposition of methylene blue in solution on semiconductor catalysts such as  $\text{TiO}_2$ <sup>23,43</sup> with UV-radiation and on other semiconductor catalysts.<sup>44</sup>

The significant time delay for the appearance of the product signals observed in Figure 2a is in contrast to other plasmon driven photochemical reactions such as the azo-coupling of PATP (in which the DMAB product signals appear instantly) as we have confirmed in our recent report.<sup>35</sup> However, the drastic intensity fluctuation observed in Figure 2a does not allow us to draw a conclusion on the basis of the temporal profile of the vibrational signals of a small number of molecules within a single focus area ( $\sim 4 \times 10^{-7}\text{ cm}^2$ ) on the sample. The intensity fluctuation can be minimized by repeating the time-dependent measurement on multiple areas so that mechanistic understanding may be obtained on the basis of the trend of the average data. To this end, 400 spectra have been acquired within  $\sim 207\text{ s}$  of irradiation time from at least 10 different random locations on the sample, and the procedure is repeated at different incident laser powers. The intensity map of the average spectra obtained at 0.16 and 0.73 mW incident laser powers is displayed in Figure 3a and b, including only the prominent peaks for clarity. Clearly, the delay of the product signals is evident in the average data, and with increasing incident laser power, the delay becomes shorter as can be seen by comparing the intensity maps of the  $479\text{ cm}^{-1}$  band in Figure 3a and b. The time delay may indicate that laser-induced adsorption is a prerequisite for the photochemical reaction.<sup>45</sup> Unlike molecules such as PATP that are chemically attached to the surface through a Au–S bond, MB may be weakly adsorbed mainly through physical interactions. The fact that the vibrational frequencies in the SERS and regular Raman spectrum of the solid agree within  $\pm 3\text{ cm}^{-1}$  as can be seen by comparing the blue and black spectra in Figure 2b is characteristic of physisorption.<sup>46</sup> The heat released following the plasmon-enhanced resonant excitation may increase the molecule–surface interaction that facilitates the photochemistry.

The average spectra plotted in Figure 3c (time average of the 400 average spectra) show that increasing the laser power increases the intensity of the vibrational signal as well as that of the background. For further quantitative analysis of the vibrational intensities, we used a relatively flat spectral region at  $\sim 707\text{ cm}^{-1}$  (marked with a vertical dashed line in Figure 3c) as a reference to correct for time-dependent background intensity. That is, at any time, the vibrational intensity  $[I_v(t)]$  of a given vibrational mode is adjusted as  $[I_v(t) - I_b(t)]/I_b(t)$ , where  $I_b(t)$  is the background intensity at time  $t$ . This approach provides the relative change of the vibrational intensity with respect to the background. The stronger background at higher laser power can scale down the amplitude change, but will not affect the rate of signal decay or rise. The background corrected intensities of the bands at  $1621$  and  $479\text{ cm}^{-1}$  are extracted from the data presented in Figure 3a and b, and the results are

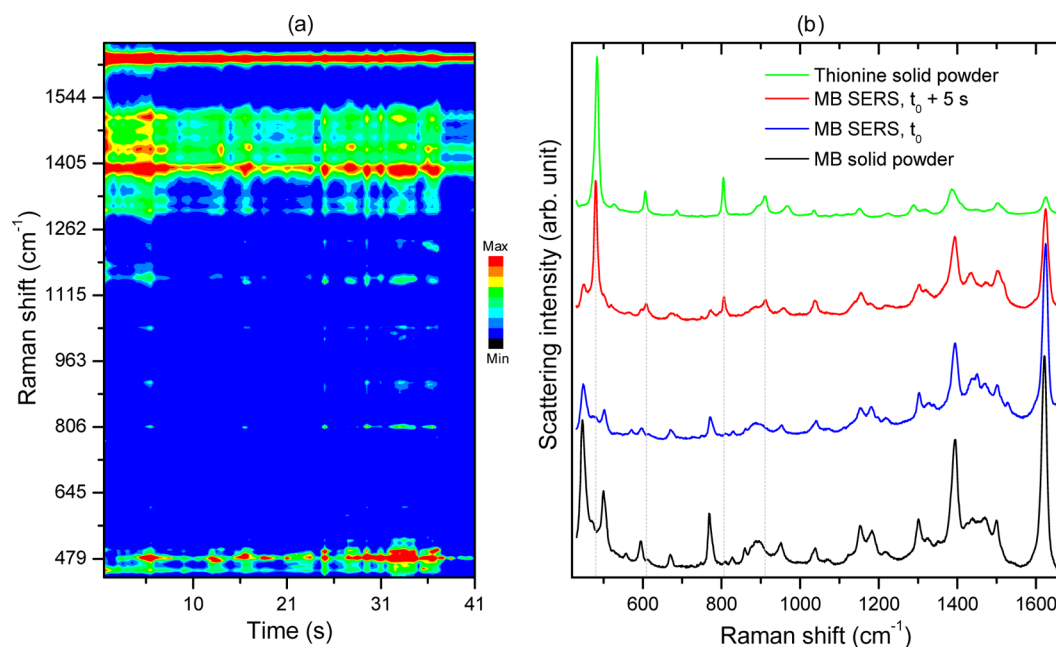


**Figure 2.** Temporal evolution of the SERS signal of methylene blue molecules in plasmonic nanocavities (AuF–AuNR gaps). (a) Intensity map representing 80 spectra acquired at different time delays after continuous irradiation with the excitation source ( $\lambda = 633$  nm). (b) Representative SERS spectra of MB recorded at the time delays indicated on the plot ( $t_0 \approx 0.5$  s, acquisition time of a single spectrum) as compared to the normal Raman spectra of methylene blue (black line) and thionine (green line) solid powders.

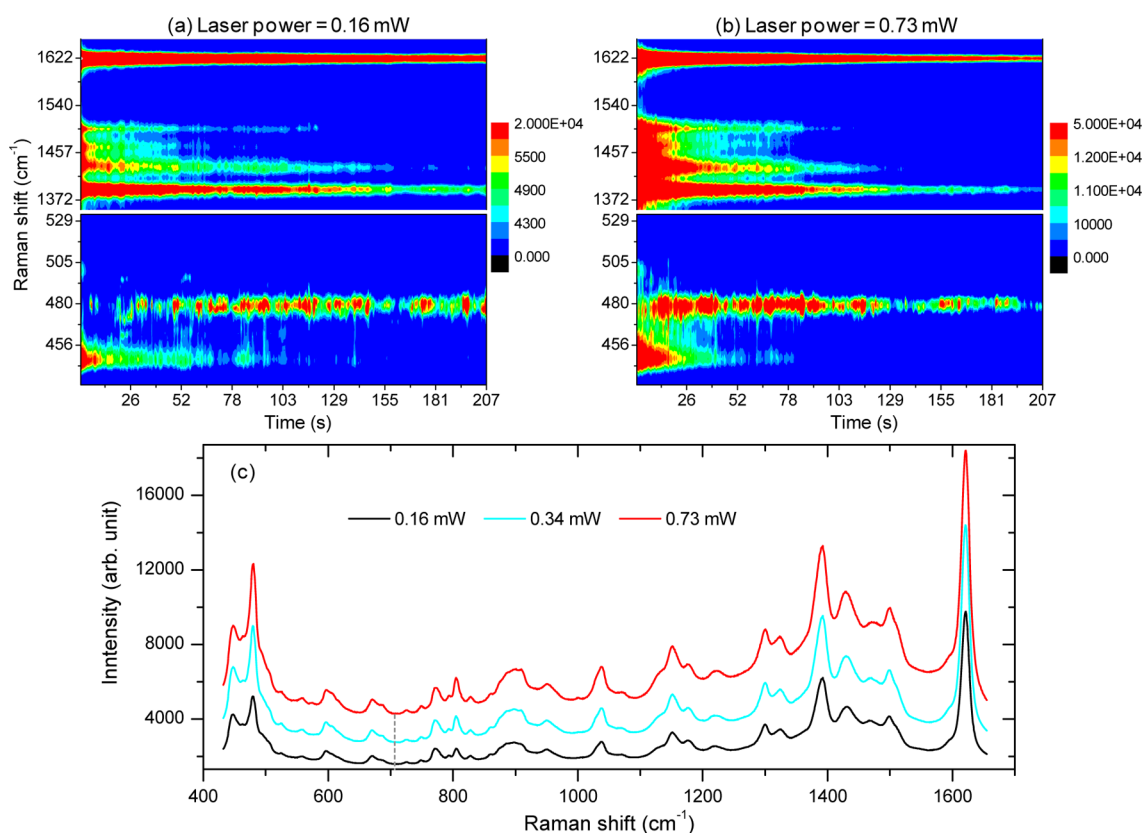


**Figure 3.** Average SERS spectra of AuF-MB-AuNR obtained at 633 nm excitation wavelength and incident laser power of (a) 0.16 mW and (b) 0.73 mW. Each intensity map represents 400 spectra acquired within 207 s, and the spectra at each time point are the average of at least 10 spectra that represent different locations on the sample. (c) Time average of the spectra acquired within 207 s at incident laser power of 0.16 mW (black line), 0.34 mW (cyan line), and 0.73 mW (red line). Note that with increasing laser power, both the background and the vibrational band intensities increase. The flat region at  $\sim 707$   $\text{cm}^{-1}$  marked with a vertical dashed line is used for background correction and for studying the temporal evolution of the vibrational band intensities.

plotted in Figure 4a and b. The  $1621\text{ cm}^{-1}$  band intensity is further normalized by the corresponding average value at time  $t_0$ . We note that both MB and thionine have the  $1621\text{ cm}^{-1}$  band, but its relative intensity is much weaker for thionine as can be seen in Figure 2. This results in a rapid decline of the  $1621\text{ cm}^{-1}$  band intensity as the MB is converted to thionine.

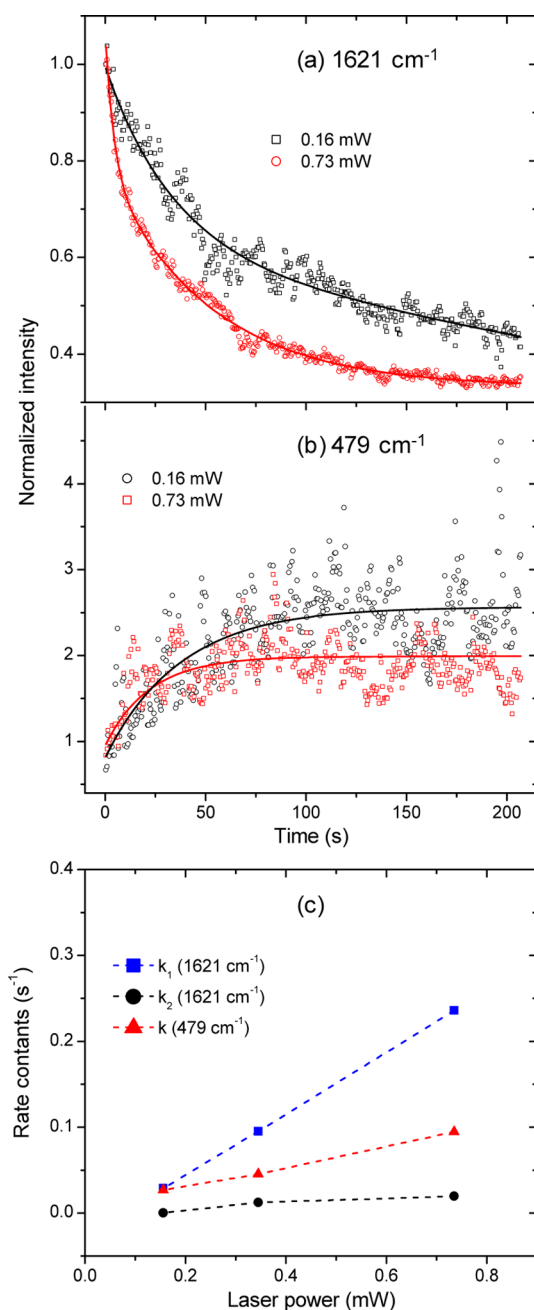


**Figure 4.** Quantitative analysis of the temporal evolution of the SERS signals using representative vibrational bands of reactant and product species. (a) The peak intensity of the  $1621\text{ cm}^{-1}$  band (after background correction and normalized as described in the text) plotted as a function of time. The solid lines represent a biexponential function ( $y = a + b e^{-t/\tau_1} + c e^{-t/\tau_2}$ , where  $\tau_1$  and  $\tau_2$  are time constants) fit to the data obtained at incident laser power of 0.16 mW (black line) and 0.73 mW (red line). (b) The same as (a) but for  $479\text{ cm}^{-1}$  band, and a single exponential function ( $y = a - b e^{-t/\tau}$ ) is fit to the data. (c) The rate constants ( $k_i = 1/\tau_i$ ) extracted from the fitting procedure in (a) and (b) are plotted as a function of laser power.

For laser power above 0.16 mW, the decay has fast and slow components, and the relevant rate constants can be extracted by fitting a biexponential function of the form  $y = a + b e^{-t/\tau_1} + c e^{-t/\tau_2}$ , where  $\tau_1$  and  $\tau_2$  are the time constants for the fast and slow dynamics, respectively. A single exponential function of the form  $y = a - b e^{-t/\tau}$  fits the rising signal of the product reasonably as shown by the solid lines in Figure 4b. The linear dependence of the rate constants ( $k = 1/\tau$ ) on laser power as shown in Figure 4c indicates that the photochemical reaction is initiated by a single photon process. The constants  $k_1$  and  $k$  have approximately equal value at 0.16 mW, and then  $k_1$  increases at a faster rate with laser power than  $k$ . This divergence of rate constants for the reactant signal decay and product signal rise with incident photon flux indicates contribution of additional processes such as desorption and gradual photobleaching of reactant molecules. These additional processes may be accounted for by the constant  $k_2$  that increases slowly with laser power.

The mechanism of plasmon driven photochemical reactions is believed to involve hot electron transfer from the plasmonic nanocrystal to adsorbed species.<sup>1,8,19–22</sup> However, several specific mechanisms that are consistent with the charge transfer process can be proposed including (i) direct excitation of the metal–MB system that involves electronic transition from occupied to unoccupied adsorbate states,<sup>32</sup> and (ii) hot electron transfer to other species such as adsorbed oxygen molecules that then initiate the reaction.<sup>47</sup> Direct charge excitation has been implied on the basis of SERS results on MB that show an excitation wavelength-dependent anti-Stokes to Stokes Raman intensity ratio.<sup>32,48</sup> An anti-Stokes to Stokes Raman intensity ratio as high as 34 has been observed at  $\lambda = 785\text{ nm}$  excitation wavelength, while the ratio is less than unity at  $\lambda = 532\text{ nm}$  excitation wavelength.<sup>32</sup> On the basis of this observation and the positive dependence of the ratio on the 785 nm photon flux, Boerigter et al. have proposed a direct resonant charge excitation mechanism that populates the excited vibrational energy levels of adsorbed MB.<sup>32,48</sup> However, no chemical transformation of MB has been observed in the experiments by Boerigter et al.<sup>32,48</sup> It should also be noted that the resonant excitation wavelengths of adsorbed MB can range from 520 to 800 nm depending on the nature of the surface–molecule interaction and on the cluster size of MB (monomer, dimer, trimer, etc.).<sup>29,49,50</sup> Our sample is prepared so that MB is adsorbed on the gold film as a monomer, and at 633 nm excitation wavelength, the anti-Stokes to Stokes Raman intensity remains very small and constant during the continuous illumination and acquisition of data for over 200 s as shown in Figure 5.

For understanding the role of the MB resonant excitation in the demethylation reaction, we have measured the SERS spectra at 532 and 808 nm excitation wavelengths such that the excitation energy overlaps with the plasmon resonances but not with the electronic transition energy of MB. In Figure 6a, the dark-field scattering spectra for MB functionalized aggregates of gold nanospheres (AuNSs) and AuNRs (longer than the NRs used to obtain the results in Figures 1–5) deposited on oxide coated silicon wafer are presented. It can be seen that the plasmon resonances of the AuNSs overlap more significantly with the 532 nm excitation wavelength than with the 633 nm. Similarly, the plasmon resonances of the AuNRs overlap more significantly with the 808 nm wavelength than with the 633 nm laser line. The vibrational signatures of thionine are observed in the SERS spectra (Figure 6b) obtained at 633 nm excitation

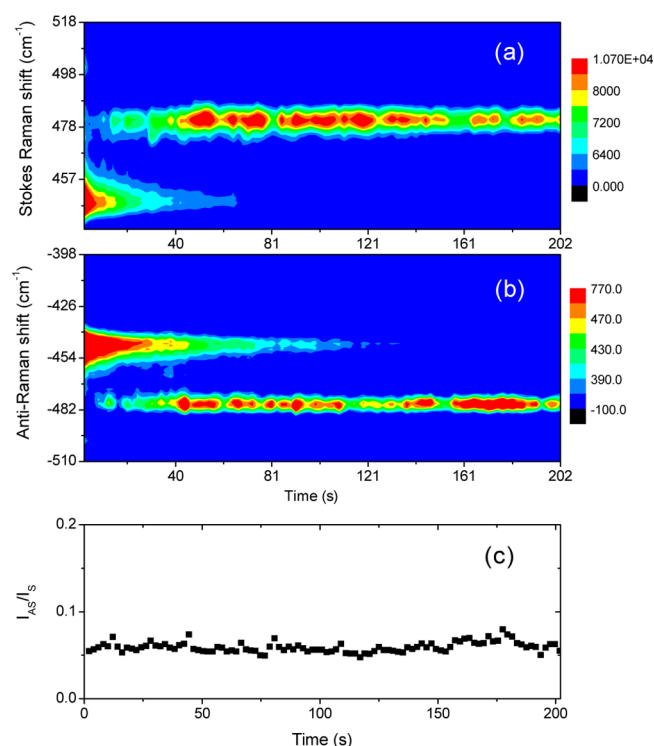


**Figure 5.** Comparison of the temporal evolution of the (a) Stokes and (b) anti-Stokes Raman intensities of the 448 and 479  $\text{cm}^{-1}$  bands. (c) Stokes to anti-Stokes intensity ratio of the 479  $\text{cm}^{-1}$  band plotted as a function of time.

wavelength for both the AuNSs (black line) and the AuNRs (green line) as indicated by the vertical dashed cyan lines where prominent bands of thionine are expected at 479 and 804  $\text{cm}^{-1}$  vibrational frequencies. In contrast, no vibrational signatures of thionine have been observed at the 532 nm (blue line) and 808 nm (red line) excitation wavelengths despite the more significant spectral overlap of the plasmon resonances with the corresponding wavelengths as illustrated in Figure 6a. On the other hand, resonant excitation of MB on nonplasmonic surfaces (glass, platinum, aluminum, and gold) does not show vibrational signatures of thionine. An example is shown in Figure 7, where MB is adsorbed on gold film, and the Raman spectra obtained immediately after the 633 nm laser is on are compared to the spectra obtained after 30 s of continuous irradiation. Clearly, the observations in Figures 6 and 7 indicate that excitation of both the molecular and the plasmon resonances is important for the demethylation reaction.

It has been reported that photocatalytic N-demethylation requires the presence of oxygen.<sup>23,43,44</sup> In particular, Takizawa et al. demonstrated systematically that anionic oxygen was responsible for initiating the demethylation of MB and Rhodamine B on CdS catalyst.<sup>44</sup> Transient anionic oxygen created via hot plasmon electron injection has also been implicated in the surface photochemistry of PATP.<sup>47,51,52</sup> These past experimental observations suggest that the demethylation of MB in our experiment is likely initiated by anionic oxygen. The anionic oxygen can interact with the terminal nitrogen atoms of MB, and hydrogen abstraction from water can lead to the transformation of methylene blue to thionine and another side product, possibly formaldehyde.<sup>44</sup> However, it is very important to emphasize that a detailed description of the mechanism requires understanding the excited-state dynamics

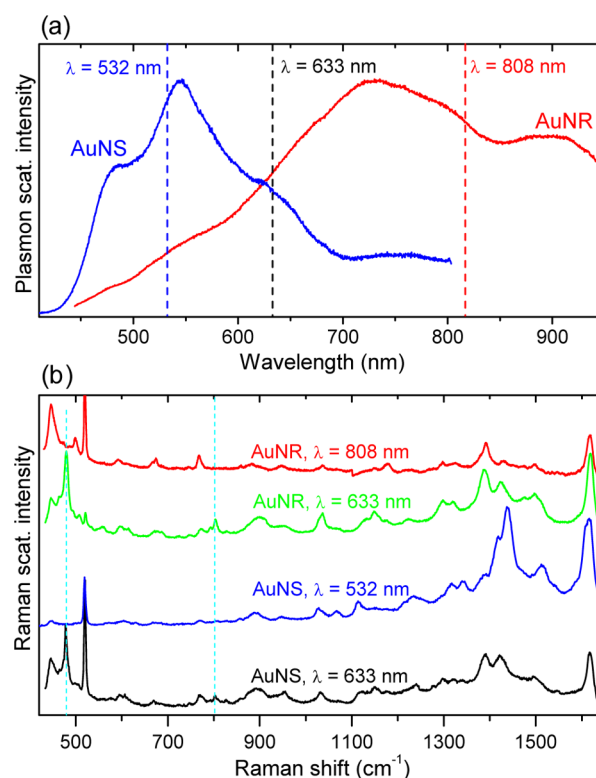


**Figure 6.** Excitation wavelength and plasmon resonance effects. (a) Dark-field scattering spectra of aggregates of gold nanospheres (AuNSs, diameter 40 nm) (blue line) and gold nanorods (AuNRs, 40 nm  $\times$  148 nm) (red line) functionalized with MB and deposited on silica surface. (b) SERS spectra of MB adsorbed on the AuNS and AuNRs recorded 30 s after the excitation lasers are on. The vertical dashed cyan lines indicate the vibrational frequencies of thionine at 479 and 804  $\text{cm}^{-1}$ . The vibrational signatures of thionine are observed at 633 nm excitation wavelength for both the AuNSs (black line) and the AuNRs (green line), but not at 532 and 808 nm excitation wavelengths despite the more significant spectral overlap of the laser lines with the corresponding plasmon resonances as shown in (a). The peak at 520  $\text{cm}^{-1}$  in all the spectra in (b) is due to silicon.

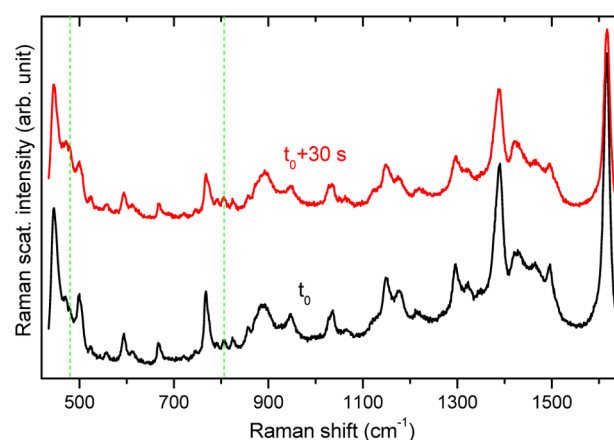


**Figure 7.** Raman spectra of MB adsorbed on gold film in the absence of any plasmonic nanoparticles. The gold substrate was kept inside  $1.5 \times 10^{-5}$  M MB in ethanol solution overnight, and the substrate was not washed as it was pulled out of the solution so that thicker than a monolayer of MB sample was obtained to improve the signal-to-noise ratio. The spectra were recorded with an acquisition time of 1 s at the 633 nm excitation wavelength and intensity of  $\sim 100$   $\text{kW}/\text{cm}^2$ .

of MB adsorbed on metal surfaces. As shown in Figure S6, initial excitation of MB can be followed by singlet to triplet intersystem crossing (quantum yield  $\sim 0.5$ )<sup>53</sup> that can lead to generation of singlet oxygen through efficient energy transfer from the triplet MB to triplet molecular oxygen,<sup>54</sup> a reason for wide use of MB as photosensitizer in photodynamic therapy. The fact that the demethylation of MB is observed at 633 nm excitation wavelength (that can promote MB from ground to excited electronic state) but not at 532 and 808 nm is consistent with the involvement of singlet oxygen in the photochemical transformation. On the other hand, the demethylation reaction does not take place on nonplasmonic surfaces, indicating the importance plasmon resonance excitation. Understanding these excited-state dynamics of molecules in the proximity of metal surfaces is a grand challenge that may invite future experiments.

## CONCLUSION

In summary, we have presented the first systematic study of plasmon driven demethylation reaction that transforms MB to thionine under visible light irradiation at room temperature without the use of any semiconductor catalysts. Upon continuous irradiation, the SERS spectra evolve from that of methylene blue to thionine as a function of time. Irradiation of MB adsorbed on nonplasmonic surfaces at 633 nm excitation wavelength does not lead to the demethylation reaction. Similarly, excitation wavelengths (532 and 808 nm) that overlap with plasmon resonances but not with the electronic absorption band of MB do not transform MB to thionine. These observations suggest that excitations of both the molecular and the plasmon resonances are important for observing the reaction. The photochemical transformation is likely initiated by transient hot plasmon electron transfer to adsorbed species. However, identifying transient intermediates and a detailed understanding of the mechanism require further experiments under controlled atmosphere as well as elucidating the potential energy landscape of MB adsorbed on metal surfaces. At visible excitation wavelengths, both MB and thionine have large SERS cross sections due to the combination of resonance Raman and electromagnetic enhancement effects, and therefore we suggest that this demethylation reaction serves as a convenient model system for future mechanistic studies in plasmon driven photochemical reactions.

## ASSOCIATED CONTENT

### Supporting Information

The Supporting Information is available free of charge on the ACS Publications website at DOI: 10.1021/acs.jpcc.7b00864.

Dark-field scattering image of gold nanorods (Figures S1 and S2); AFM topographic image of gold nanorods (Figure S3); comparison of the surface-enhanced Raman spectrum of thionine with the normal Raman spectrum of thionine solid powder (Figure S4); calculated Raman spectra (Figure S5); and energy diagram of methylene blue (Figure S6) (PDF)

## AUTHOR INFORMATION

### Corresponding Author

\*E-mail: habteyes@unm.edu.

### ORCID

Terefe G. Habteyes: 0000-0001-5978-6464

## Notes

The authors declare no competing financial interest.

## ACKNOWLEDGMENTS

This research has been supported by the U.S. Air Force Office of Scientific Research, grant no. FA9550-15-1-0305, and the Air Force Research Laboratory, grant no. FA9453-15-1-0078.

## REFERENCES

- (1) Jeanmaire, D. L.; Vanduyne, R. P. Surface Raman Spectroelectrochemistry 0.1. Heterocyclic, Aromatic, and Aliphatic-Amines Adsorbed on Anodized Silver Electrode. *J. Electroanal. Chem. Interfacial Electrochem.* **1977**, *84*, 1–20.
- (2) Moskovits, M. Surface-Roughness and Enhanced Intensity of Raman-Scattering by Molecules Adsorbed on Metals. *J. Chem. Phys.* **1978**, *69*, 4159–4161.
- (3) Nitzan, A.; Brus, L. E. Can Photochemistry Be Enhanced on Rough Surfaces? *J. Chem. Phys.* **1981**, *74*, 5321–5322.
- (4) Nitzan, A.; Brus, L. E. Theoretical-Model for Enhanced Photochemistry on Rough Surfaces. *J. Chem. Phys.* **1981**, *75*, 2205–2214.
- (5) Goncher, G. M.; Harris, C. B. Enhanced Photofragmentation on a Silver Surface. *J. Chem. Phys.* **1982**, *77*, 3767–3768.
- (6) Bunding, K. A.; Durst, R. A.; Bell, M. I. Surface-Enhanced Raman-Spectroscopy of N-Methylpyridinium Cation and Pyridine - Identification of Surface Species. *J. Electroanal. Chem. Interfacial Electrochem.* **1983**, *150*, 437–446.
- (7) Goncher, G. M.; Parsons, C. A.; Harris, C. B. Photochemistry on Rough Metal-Surfaces. *J. Phys. Chem.* **1984**, *88*, 4200–4209.
- (8) Lu, T.; Birke, R. L.; Lombardi, J. R. Surface Raman-Spectroscopy of the 3 Redox Forms of Methylviologen. *Langmuir* **1986**, *2*, 305–309.
- (9) Wolkow, R. A.; Moskovits, M. Enhanced Photochemistry on Silver Surfaces. *J. Chem. Phys.* **1987**, *87*, 5858–5869.
- (10) Sun, S. C.; Birke, R. L.; Lombardi, J. R.; Leung, K. P.; Genack, A. Z. Photolysis of Para-Nitrobenzoic Acid on Roughened Silver Surfaces. *J. Phys. Chem.* **1988**, *92*, 5965–5972.
- (11) White, J. M. Photochemistry at Adsorbate Metal Interfaces - Issues and Examples. *J. Vac. Sci. Technol., B: Microelectron. Process. Phenom.* **1992**, *10*, 191–195.
- (12) Suh, J. S.; Jang, N. H.; Jeong, D. H.; Moskovits, M. Adsorbate Photochemistry on a Colloid Surface: Phthalazine on Silver. *J. Phys. Chem.* **1996**, *100*, 805–813.
- (13) Huang, Y.-F.; Zhu, H.-P.; Liu, G.-K.; Wu, D.-Y.; Ren, B.; Tian, Z.-Q. When the Signal Is Not from the Original Molecule to Be Detected: Chemical Transformation of Para-Aminothiophenol on Ag During the SERS Measurement. *J. Am. Chem. Soc.* **2010**, *132*, 9244–9246.
- (14) Fang, Y. R.; Li, Y. Z.; Xu, H. X.; Sun, M. T. Ascertaining P,P'-Dimercaptoazobenzene Produced from P-Aminothiophenol by Selective Catalytic Coupling Reaction on Silver Nanoparticles. *Langmuir* **2010**, *26*, 7737–7746.
- (15) Yan, X. F.; Wang, L. Z.; Tan, X. J.; Tian, B. Z.; Zhang, J. L. Surface-Enhanced Raman Spectroscopy Assisted by Radical Capturer for Tracking of Plasmon-Driven Redox Reaction. *Sci. Rep.* **2016**, *6*, 30193.
- (16) Christopher, P.; Xin, H. L.; Linic, S. Visible-Light-Enhanced Catalytic Oxidation Reactions on Plasmonic Silver Nanostructures. *Nat. Chem.* **2011**, *3*, 467–472.
- (17) Mukherjee, S.; Libisch, F.; Large, N.; Neumann, O.; Brown, L. V.; Cheng, J.; Lassiter, J. B.; Carter, E. A.; Nordlander, P.; Halas, N. J., Hot Electrons Do the Impossible: Plasmon-Induced Dissociation of H<sub>2</sub> on Au. *Nano Lett.* **2013**, *13*, 240–247.
- (18) Zhang, Y.; Xiao, Q.; Bao, Y.; Zhang, Y.; Bottle, S.; Sarina, S.; Zhaorigetu, B.; Zhu, H. Direct Photocatalytic Conversion of Aldehydes to Esters Using Supported Gold Nanoparticles under Visible Light Irradiation at Room Temperature. *J. Phys. Chem. C* **2014**, *118*, 19062–19069.

- (19) Nie, S.; Emory, S. R. Probing Single Molecules and Single Nanoparticles by Surface-Enhanced Raman Scattering. *Science* **1997**, *275*, 1102–1106.
- (20) Kneipp, K.; Wang, Y.; Kneipp, H.; Perelman, L. T.; Itzkan, I.; Dasari, R. R.; Feld, M. S. Single Molecule Detection Using Surface-Enhanced Raman Scattering (SERS). *Phys. Rev. Lett.* **1997**, *78*, 1667.
- (21) Kleinman, S. L.; Ringe, E.; Valley, N.; Wustholz, K. L.; Phillips, E.; Scheidt, K. A.; Schatz, G. C.; Van Duyne, R. P. Single-Molecule Surface-Enhanced Raman Spectroscopy of Crystal Violet Isotopologues: Theory and Experiment. *J. Am. Chem. Soc.* **2011**, *133*, 4115–4122.
- (22) Lombardi, J. R.; Birke, R. L. A Unified Approach to Surface-Enhanced Raman Spectroscopy. *J. Phys. Chem. C* **2008**, *112*, 5605–5617.
- (23) Zhang, T. Y.; Oyama, T.; Aoshima, A.; Hidaka, H.; Zhao, J. C.; Serpone, N. Photooxidative N-Demethylation of Methylene Blue in Aqueous TiO<sub>2</sub> Dispersions under Uv Irradiation. *J. Photochem. Photobiol., A* **2001**, *140*, 163–172.
- (24) Rauf, M. A.; Meetani, M. A.; Khaleel, A.; Ahmed, A. Photocatalytic Degradation of Methylene Blue Using a Mixed Catalyst and Product Analysis by LC/MS. *Chem. Eng. J.* **2010**, *157*, 373–378.
- (25) Molla, A.; Sahu, M.; Hussain, S. Under Dark and Visible Light: Fast Degradation of Methylene Blue in the Presence of Ag-In-Ni-S Nanocomposites. *J. Mater. Chem. A* **2015**, *3*, 15616–15625.
- (26) Chen, J.; Cesario, T. C.; Rentzepis, P. M. Time Resolved Spectroscopic Studies of Methylene Blue and Phenothiazine Derivatives Used for Bacteria Inactivation. *Chem. Phys. Lett.* **2010**, *498*, 81–85.
- (27) Dean, J. C.; Oblinsky, D. G.; Rafiq, S.; Scholes, G. D. Methylene Blue Exciton States Steer Nonradiative Relaxation: Ultrafast Spectroscopy of Methylene Blue Dimer. *J. Phys. Chem. B* **2016**, *120*, 440–454.
- (28) Naujok, R. R.; Duevel, R. V.; Corn, R. M. Fluorescence and Fourier-Transform Surface-Enhanced Raman-Scattering Measurements of Methylene-Blue Adsorbed onto a Sulfur-Modified Gold Electrode. *Langmuir* **1993**, *9*, 1771–1774.
- (29) Rubim, J. C.; Sousa, M. H.; Silva, J. C. O.; Tourinho, F. A. Raman Spectroscopy as a Powerful Technique in the Characterization of Ferrofluids. *Braz. J. Phys.* **2001**, *31*, 402–408.
- (30) Nicolai, S. H. A.; Rubim, J. C. Surface-Enhanced Resonance Raman (SERR) Spectra of Methylene Blue Adsorbed on a Silver Electrode. *Langmuir* **2003**, *19*, 4291–4294.
- (31) Xiao, G. N.; Man, S. Q. Surface-Enhanced Raman Scattering of Methylene Blue Adsorbed on Cap-Shaped Silver Nanoparticles. *Chem. Phys. Lett.* **2007**, *447*, 305–309.
- (32) Boerigter, C.; Campana, R.; Morabito, M.; Linic, S. Evidence and Implications of Direct Charge Excitation as the Dominant Mechanism in Plasmon-Mediated Photocatalysis. *Nat. Commun.* **2016**, *7*, 10545.
- (33) Fazio, B.; D'Andrea, C.; Bonaccorso, F.; Irrera, A.; Calogero, G.; Vasi, C.; Gucciard, P. G.; Allegrini, M.; Toma, A.; Chiappe, D.; Martella, C.; de Mongeot, F. B. Re-Radiation Enhancement in Polarized Surface-Enhanced Resonant Raman Scattering of Randomly Oriented Molecules on Self-Organized Gold Nanowires. *ACS Nano* **2011**, *5*, 5945–5956.
- (34) Chikkaraddy, R.; de Nijs, B.; Benz, F.; Barrow, S. J.; Scherman, O. A.; Rosta, E.; Demetriadou, A.; Fox, P.; Hess, O.; Baumberg, J. J. Single-Molecule Strong Coupling at Room Temperature in Plasmonic Nanocavities. *Nature* **2016**, *535*, 127–130.
- (35) Kafle, B.; Poveda, M.; Habteyes, T. G. Surface Ligand-Mediated Plasmon-Driven Photochemical Reactions. *J. Phys. Chem. Lett.* **2017**, *8*, 890–894.
- (36) Habteyes, T. G.; Dhuey, S.; Kiesow, K. I.; Vold, A. Probe-Sample Optical Interaction: Size and Wavelength Dependence in Localized Plasmon near-Field Imaging. *Opt. Express* **2013**, *21*, 21607.
- (37) Kafle, B.; Tesema, T. E.; Kazemi, A.; Habteyes, T. G. Stripping and Transforming Alloyed Semiconductor Quantum Dots Via Atomic Interdiffusion. *J. Phys. Chem. C* **2016**, *120*, 12850–12859.
- (38) Anderson, S. Orientation of Methylene Blue Molecules Adsorbed on Solids. *J. Opt. Soc. Am.* **1949**, *39*, 49–56.
- (39) Greathouse, J. A.; Geatches, D. L.; Pike, D. Q.; Greenwell, H. C.; Johnston, C. T.; Wilcox, J.; Cygan, R. T. Methylene Blue Adsorption on the Basal Surfaces of Kaolinite: Structure and Thermodynamics from Quantum and Classical Molecular Simulation. *Clays Clay Miner.* **2015**, *63*, 185–198.
- (40) Mock, J. J.; Hill, R. T.; Degiron, A.; Zauscher, S.; Chilkoti, A.; Smith, D. R. Distance-Dependent Plasmon Resonant Coupling between a Gold Nanoparticle and Gold Film. *Nano Lett.* **2008**, *8*, 2245–2252.
- (41) Planas, O.; Bresoli-Obach, R.; Nos, J.; Gallavardin, T.; Ruiz-Gonzalez, R.; Agut, M.; Nonell, S. Synthesis, Photophysical Characterization, and Photoinduced Antibacterial Activity of Methylene Blue-Loaded Amino- and Mannose-Targeted Mesoporous Silica Nanoparticles. *Molecules* **2015**, *20*, 6284–6298.
- (42) Hutchinson, K.; Hester, R. E.; Albery, W. J.; Hillman, A. R. Raman-Spectroscopic Studies of a Thionine-Modified Electrode. *J. Chem. Soc., Faraday Trans. 1* **1984**, *80*, 2053–2071.
- (43) Yogi, C.; Kojima, K.; Wada, N.; Tokumoto, H.; Takai, T.; Mizoguchi, T.; Tamiaki, H. Photocatalytic Degradation of Methylene Blue by TiO<sub>2</sub> Film and Au Particles-TiO<sub>2</sub> Composite Film. *Thin Solid Films* **2008**, *516*, 5881–5884.
- (44) Takizawa, T.; Watanabe, T.; Honda, K. Photocatalysis through Excitation of Adsorbates 0.2. Comparative-Study of Rhodamine-B and Methylene-Blue on Cadmium-Sulfide. *J. Phys. Chem.* **1978**, *82*, 1391–1396.
- (45) Fox, M. A.; Dulay, M. T. Heterogeneous Photocatalysis. *Chem. Rev.* **1993**, *93*, 341–357.
- (46) Otto, A.; Mrozek, I.; Grabhorn, H.; Akemann, W. Surface-Enhanced Raman-Scattering. *J. Phys.: Condens. Matter* **1992**, *4*, 1143–1212.
- (47) Xu, P.; Kang, L. L.; Mack, N. H.; Schanze, K. S.; Han, X. J.; Wang, H. L. Mechanistic Understanding of Surface Plasmon Assisted Catalysis on a Single Particle: Cyclic Redox of 4-Aminothiophenol. *Sci. Rep.* **2013**, *3*, 2997.
- (48) Boerigter, C.; Aslam, U.; Linic, S. Mechanism of Charge Transfer from Plasmonic Nanostructures to Chemically Attached Materials. *ACS Nano* **2016**, *10*, 6108–6115.
- (49) Cenens, J.; Schoonheydt, R. A. Visible Spectroscopy of Methylene-Blue on Hectorite, Laponite-B, and Barasym in Aqueous Suspension. *Clays Clay Miner.* **1988**, *36*, 214–224.
- (50) Jacobs, K. Y.; Schoonheydt, R. A. Time Dependence of the Spectra of Methylene Blue-Clay Mineral Suspensions. *Langmuir* **2001**, *17*, 5150–5155.
- (51) Huang, Y. F.; Zhang, M.; Zhao, L. B.; Feng, J. M.; Wu, D. Y.; Ren, B.; Tian, Z. Q. Activation of Oxygen on Gold and Silver Nanoparticles Assisted by Surface Plasmon Resonances. *Angew. Chem., Int. Ed.* **2014**, *53*, 2353–2357.
- (52) Zhao, L. B.; Liu, X. X.; Zhang, M.; Liu, Z. F.; Wu, D. Y.; Tian, Z. Q. Surface Plasmon Catalytic Aerobic Oxidation of Aromatic Amines in Metal/Molecule/Metal Junctions. *J. Phys. Chem. C* **2016**, *120*, 944–955.
- (53) Redmond, R. W.; Gamlin, J. N. A Compilation of Singlet Oxygen Yields from Biologically Relevant Molecules. *Photochem. Photobiol.* **1999**, *70*, 391–475.
- (54) Tardivo, J. P.; Del Giglio, A.; de Oliveira, C. S.; Gabrielli, D. S.; Junqueira, H. C.; Tada, D. B.; Severino, D.; Turchiello, R. D. F.; Baptista, M. S. Methylene Blue in Photodynamic Therapy: From Basic Mechanisms to Clinical Applications. *Photodiagn. Photodyn. Ther.* **2005**, *2*, 175–191.

# SCIENTIFIC REPORTS

OPEN

## Active Mediation of Plasmon Enhanced Localized Exciton Generation, Carrier Diffusion and Enhanced Photon Emission

Sharmin Haq<sup>3,4</sup>, Sadhvikas Addamane<sup>2,4</sup>, Bijesh Kafle<sup>1,4</sup>, Danhong Huang<sup>5</sup>, Ganesh Balakrishnan<sup>2,3,4</sup> & Terefe G. Habteyes<sup>1,3,4</sup>

Understanding the enhancement of charge carrier generation and their diffusion is imperative for improving the efficiency of optoelectronic devices particularly infrared photodetectors that are less developed than their visible counterpart. Here, using gold nanorods as model plasmonic systems, InAs quantum dots (QDs) embedded in an InGaAs quantum well as an emitter, and GaAs as an active mediator of surface plasmons for enhancing carrier generation and photon emission, the distance dependence of energy transfer and carrier diffusion have been investigated both experimentally and theoretically. Analysis of the QD emission enhancement as a function of distance reveals a Förster radius of  $3.85 \pm 0.15$  nm, a near-field decay length of  $4.8 \pm 0.1$  nm and an effective carrier diffusion length of  $64.0 \pm 3.0$  nm. Theoretical study of the temporal-evolution of the electron-hole occupation number of the excited states of the QDs indicates that the emission enhancement trend is determined by the carrier diffusion and capture rates.

Excitons and localized surface plasmons are the two fundamental excitation characteristics of nanoscale materials. The coupling between excitonic and plasmonic materials promises control of photon emission<sup>1–3</sup> and creation of new metamaterial properties<sup>4,5</sup> that do not exist in nature. Fundamental understanding of exciton-plasmon interaction can lead to development of efficient photovoltaics<sup>6–8</sup>, photodetectors<sup>9,10</sup>, photocatalysis<sup>11,12</sup> and other optoelectronic devices. Classic experiments on exciton-plasmon interactions have often used optically transparent spacer materials between the plasmonic metal and excitonic semiconductor materials<sup>1,3,13,14</sup>. Coupling through optically transparent spacers does not allow studying charge transport process. On the other hand, studies on plasmon enhanced near-infrared photo-detectors are focused on coupling metallic two-dimensional-hole-arrays with layered semiconductor materials such as InAs/InGaAs/GaAs dot-in-a-well (DWELL) structures<sup>9,15</sup>. This enhancement mechanism exploits the extraordinary optical transmission effect<sup>16</sup>, where the transmitted field extends to about  $1 \mu\text{m}$  length covering the whole active region<sup>15</sup>, and does not allow fundamental understanding of localized exciton generation, charge carrier diffusion and recombination.

In this work, energy transfer and charge carrier diffusion are investigated systematically taking advantage of the tight electric field localization at the interfaces of plasmonic gold nanorods (AuNRs) and semiconductor GaAs that is grown over the InAs/InGaAs DWELL with accurate control of the GaAs thickness. When excitation energy that is above the GaAs band gap is chosen, the localized electric field enhances generation of electron-hole pairs (excitons) in a defined spatial region away from the InAs QDs so that carrier diffusion and capture rates are studied by monitoring the emission intensity of the QDs. The fact that the GaAs thickness can be controlled with sub-nanometer accuracy allows us to study the distance dependencies of near-field confinement, carrier diffusion and excitation energy transfer to the metal surface that leads to quenching of photoluminescence (PL) at short AuNR-InAs separation distances.

<sup>1</sup>Department of Chemistry & Chemical Biology, University of New Mexico, Albuquerque, NM, 87131, United States.

<sup>2</sup>Electrical & Computer Engineering, University of New Mexico, Albuquerque, NM, 87131, United States. <sup>3</sup>Optical Science & Engineering Program, University of New Mexico, Albuquerque, NM, 87131, United States. <sup>4</sup>Center for High Technology Materials, University of New Mexico, Albuquerque, NM, 87131, United States. <sup>5</sup>Space Vehicles Directorate, Air Force Research Laboratory, Kirtland AFB, NM, 87117, United States. Correspondence and requests for materials should be addressed to T.G.H. (email: [habteyes@unm.edu](mailto:habteyes@unm.edu))

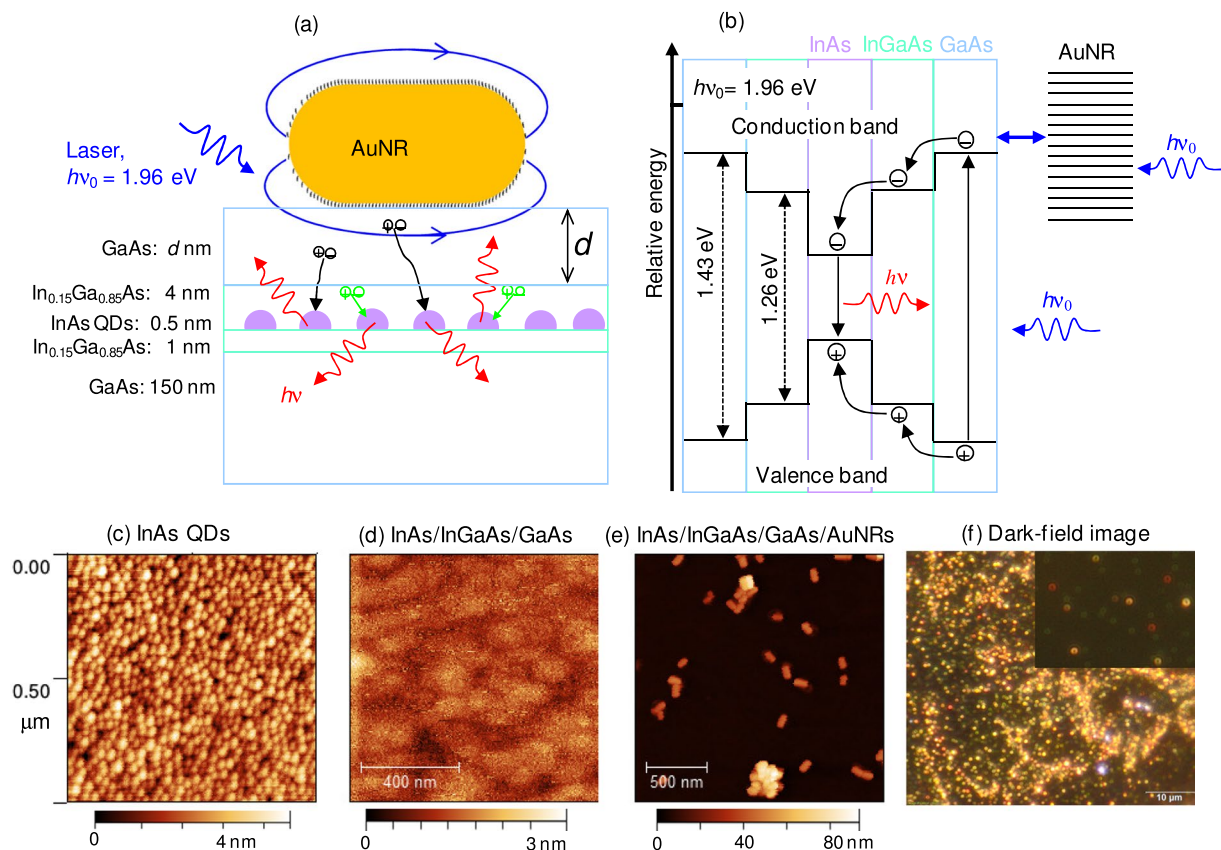


**Figure 1.** Integration of semiconductor and plasmonic materials for the studies of plasmon enhanced exciton generation and photon emission. **(a)** Schematic showing the InAs quantum dots (QDs) confined in an InGaAs quantum well, capped with GaAs of variable thickness ( $d$ ) and coupled to a single gold nanorod (AuNR). The short lines around the colloidal AuNR represent the surface ligands (cetyltrimethylammonium bromide). The plasmon near-field enhances electron-hole pair generation in the GaAs and InGaAs layers and the enhancement of photon emission by the InAs QDs depends on the carrier capture rates from the GaAs (black arrow) and from the InGaAs well (green arrow) by the QDs. **(b)** The energy level diagram shows that the excitation energy (1.96 eV) is high enough to promote electron from the valence band to the conduction band in any of the materials including the GaAs that has the highest band gap energy. **(c–e)** Topographic AFM scan images obtained before the InGaAs and GaAs layers are grown **(d)**, after the InGaAs and GaAs layers are grown **(e)**, and after the AuNRs are drop-casted on the GaAs surface. **(f)** Dark-field image of AuNRs on GaAs surface. The color of the dark-field images of the individual AuNRs varies from red to green, depending on the proximity of the AuNRs to the GaAs surface.

The choice of the QDs as opposed to InGaAs/GaAs quantum well as model system is motivated by the more efficient excitation of the QDs with in-plane polarized electric field of light at normal incidence<sup>17–19</sup>. In addition, QDs can facilitate the theoretical comparison as they can be treated as point dipoles. We note that the AuNR plasmon resonances that overlaps with the excitation wavelength ( $\lambda = 633$  nm) are far from the emission wavelength ( $\lambda \approx 1200$  nm) of the QDs. Therefore, the PL enhancement originates purely from the enhancement of photoabsorption and exciton generation inside the GaAs and InGaAs layers. All the optical measurements have been carried out at room temperature at which the thermal energy is larger than the exciton binding energy. As a result, the excitons generated at the plasmonic hot spots of the AuNR-GaAs interface can dissociate, and the PL enhancement can be attributed to the diffusion of charge carriers (electrons and holes) to the InAs QDs. When the GaAs thickness is comparable to the near-field decay length, the near-field directly enhances the exciton generation inside the InAs/InGaAs, where electron-hole recombination may dominate over exciton dissociation because of the proximity to the emitting QDs.

## Results and Discussion

The interfacial and energetic structures of the integrated plasmonic and semiconductor materials are illustrated in the schematic shown in Fig. 1 (see Method for the details of the fabrication and integration procedures). The spacing between the GaAs and the AuNR surfaces can vary depending on the amount of surface ligands (represented by short lines in Fig. 1a) on the colloidal AuNRs. The size of the AuNRs (nominal size: 40 nm diameter and 80 nm length; see ref. 20 for the size distribution) is chosen so that the plasmon resonances overlap with the 633 nm excitation wavelength. As illustrated in Fig. 1b, the excitation energy of the laser ( $hc/\lambda = 1.96$  eV, where  $h$  is Planck's constant and  $c$  is the speed of light) is above the interband electronic transition energies of both

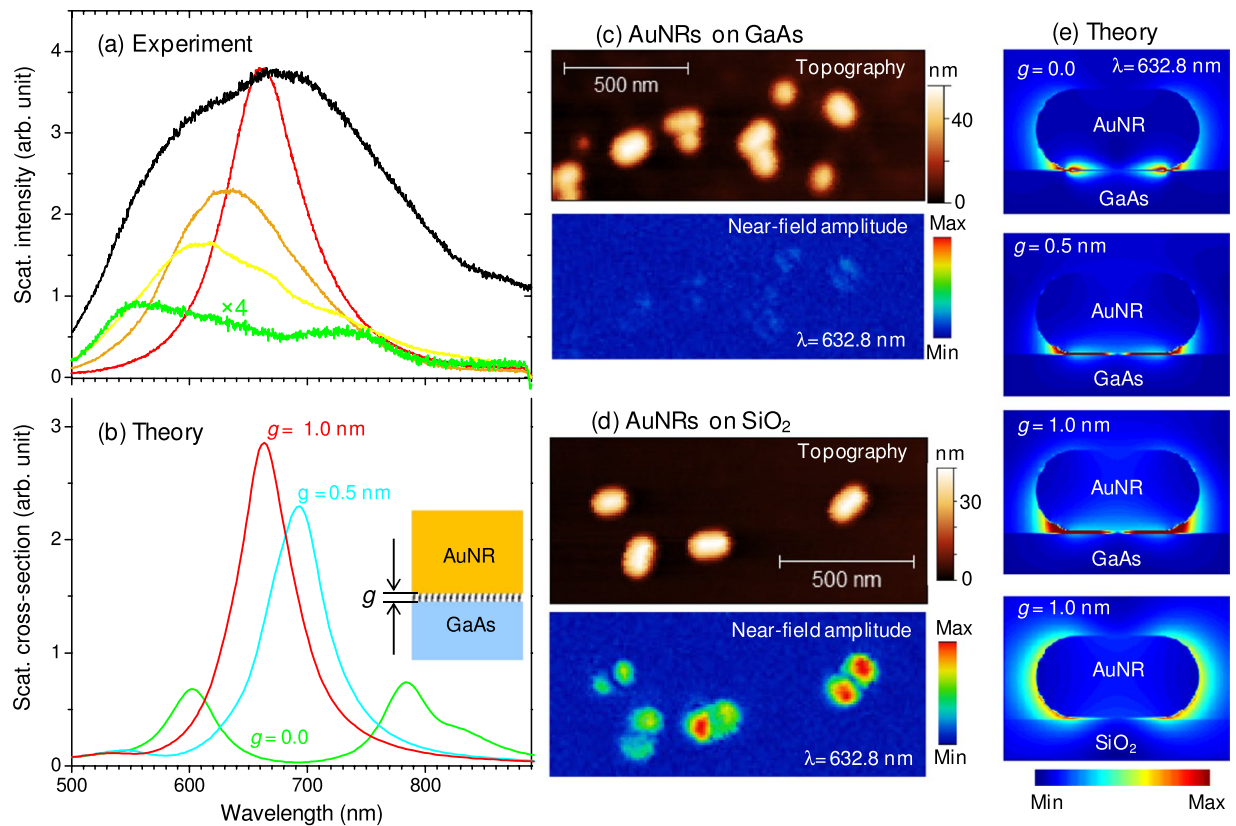


**Figure 2.** Optical properties of colloidal AuNRs deposited on GaAs surface. **(a)** Scattering spectra of individual AuNRs that appear red, orange, yellow and green in the dark-field image (shown with the corresponding colors) along with the scattering spectrum of collection of AuNRs (black curve). The black curve is recorded at lower acquisition time to avoid detector saturation and the intensity is adjusted to match its maximum to that of the red spectrum. **(b)** The calculated scattering cross-section of AuNR (40 nm × 80 nm) when the AuNR-GaAs gap is 0 (green line), 0.5 nm (cyan line) and 1.0 nm (red line). **(c)** Topography and measured near-field amplitude of AuNRs on GaAs surface. **(d)** Similar to **(c)** but the AuNRs are supported on silica surface. The results in **(c)** and **(d)** are obtained with the same experimental conditions and the near-field amplitudes are scaled to the same maximum. **(e)** The near-field amplitude calculated on a plane that cuts the AuNR through its center vertically for AuNR-GaAs separation distances of 0.0, 0.5 and 1.0 nm as labeled, compared to the field distribution when the AuNR is supported on a silica surface (bottom most panel).

GaAs (~1.43 eV) and InGaAs (~1.26 eV) materials. Excitation of the localized surface plasmon resonances of the AuNRs interfaced with the GaAs further enhances the exciting electric field and improves the efficiency of exciton generation. The topographic atomic force microscope (AFM) image in Fig. 1c shows that our molecular beam epitaxy crystal growth procedure produces close-packed self-assembled InAs QDs. The growth of the InGaAs and GaAs layers results in a planar surface as seen in Fig. 1d. The topographic image of the region, where an aqueous solution of gold nanorods is drop-casted on the GaAs surface shows randomly distributed individual AuNRs and some aggregates as shown in Fig. 1e. The distribution of the AuNRs over a larger area is displayed in the diffraction limited dark-field scattering image in Fig. 1f. In agreement with previous observations on silicon substrate<sup>21</sup>, the dark-field images of individual AuNRs on GaAs surface have doughnut shaped structures. Interestingly, the color of the scattering images of the individual AuNRs ranges from red to green (see the inset image in Fig. 1f), which can be sorted as red, orange, yellow and green (ROYG).

Single particle scattering spectra have been recorded from the particles that appear red, orange, yellow and green in the dark-field image, and representative results are presented in Fig. 2a (using the corresponding line color), along with the scattering spectrum of ensemble of the AuNRs (black curve). The plasmon scattering spectra of the red particles have  $666 \pm 17$  nm peak wavelength and  $81 \pm 5$  nm full-width-at-half maximum (FWHM), compared to 628 nm average peak wavelength and 52 nm FWHM for the same size AuNRs on a glass substrate, which have been characterized under the same optical settings. The significant red-shift and broader FWHM of the AuNR resonances on GaAs compared to that on glass, can respectively be attributed to the high refractive index and the dissipative property of the GaAs substrate as can be realized from its dielectric function ( $\epsilon_{\text{GaAs}} = 14.83 + i1.52$  at 632.8 nm excitation wavelength). As seen in Fig. 2a, the spectra are progressively broadened as the color changes from red to orange and to yellow. Finally spectral splitting is observed for the green particles that have very weak overall scattering intensity. The theoretical scattering spectra (Fig. 2b), calculated using finite-difference time domain (FDTD) method of electromagnetic simulation, agree with the measured

spectra (Fig. 2a) of the red particles when there is 0.5 to 1.0 nm gap between the AuNR and GaAs surfaces. The spectra of the green particles is reasonably reproduced in the simulation when the AuNR is in direct contact with the GaAs surface as shown by the green curve in Fig. 2b: the longitudinal plasmon resonance shifts to the red by about 150 nm with respect to that supported on glass surface, and a substrate-induced plasmon resonance<sup>21, 22</sup> appears around 600 nm. Based on this comparison of experimental and theoretical results, the ROYG color can be attributed to different proximity of the AuNRs to the GaAs, R being the furthest from the surface and G the closest. The variation in the separation distances can mainly be attributed to different amounts of the surface ligands (cetyltrimethylammonium bromide) on the colloidal gold nanorods. In our study of plasmon enhanced exciton generation and diffusion, the illumination area is relatively large (~3 mm<sup>2</sup>), and therefore, the enhancement results from ensemble averaging represented by the black spectrum in Fig. 2a.

High resolution electric field imaging using our apertureless near-field scanning optical microscope (ANSOM)<sup>23, 24</sup> shows very weak near-field amplitude on the gold nanorods when supported on GaAs (Fig. 2c), compared to the large near-field amplitude of the dipolar mode for the AuNRs supported on a silica surface (Fig. 2d), which shows orientation dependent near-field optical response in agreement with our previous results<sup>20</sup>. This weaker near-field amplitude for AuNR-GaAs than for AuNR-SiO<sub>2</sub> is in contrast to our observation of a much stronger scattering intensity for AuNRs on GaAs than for those on silica surfaces. The results of the FDTD simulation displayed in Fig. 2e shows that the electric field is tightly localized at the AuNR – GaAs interfacial region. This tight electric field localization is significantly different from that observed when the AuNR are supported on the SiO<sub>2</sub> substrate, where the electric field amplitude at the AuNR-SiO<sub>2</sub> interface is comparable to the amplitude on the top surface (AuNR-air interface). This drastically different field localization results in weaker near-field amplitude in the ANSOM data for the AuNRs on the GaAs because the electric field localized at the AuNR-GaAs interfacial region is about 40 nm (the nominal diameter of the AuNRs) away from the near-field probing tip, and it is inaccessible by the ANSOM imaging technique. However, this electric field localization is advantageous for enhancing exciton generation in the GaAs layer very close to the interface and for studying energy transfer and carrier diffusion as discussed next.

The PL enhancement/quenching as a function of GaAs thickness  $d$  (as defined in Fig. 1a) is studied by comparing the PL intensity ( $I_{\text{InAs/AuNR}}$ ) of the region where the AuNRs are deposited to the intensity ( $I_{\text{InAs}}$ ) of the region where there are no AuNRs. Representative PL spectra of the two regions are compared in Fig. 3a considering a 6 nm GaAs thickness. In each case, 15 to 20 spectra are acquired by irradiating different areas in the respective regions, and the spectra with minimum and maximum peak intensities along with the average data are plotted in Fig. 3a. In the absence of the AuNRs, no significant intensity fluctuation is observed as indicated by a standard deviation that is not much larger than the symbols (black triangle, in Fig. 3a), indicating the uniformity of the InAs QD number density within the irradiation volume. Comparing the red and black curves in Fig. 3a, it can be seen that the weakest PL intensity obtained in the presence of the AuNRs is significantly stronger than the highest PL intensity obtained from the region without the AuNRs. The intensity fluctuation for the regions where there are AuNRs (red lines) is due to the difference in the number density and aggregation of AuNRs at different locations. However, this intensity fluctuation is minor considering the spatial variation of the gold nanorod orientation and number density at the nanoscale as shown in Fig. 1e. The reproducibility of the relative intensity at different locations is due to a large illumination area that provides statistical representation of the distribution of orientation and aggregation.

Similar comparison as presented in Fig. 3a has been repeated for  $d = 1.5$  nm to 196 nm and the results are discussed in terms of an emission enhancement factor ( $EF$ ) as follows. The  $EF$  for the samples with different GaAs thicknesses is evaluated independently by calculating the integrated PL intensity ratio as follows.

$$EF = \frac{I_{\text{InAs/AuNR}}}{I_{\text{InAs}}} \quad (1)$$

Both the average (black circles) and maximum (red triangles)  $EF$  values are plotted in Fig. 3b. As seen in the figure, the enhancement factor first increases exponentially with decreasing distance until  $d = 6$  nm and then decreases rapidly for shorter distances. The general trend is in good agreement with the observation of fluorescence enhancement and quenching by a gold nanosphere reported by Novotny and co-workers<sup>14</sup>. However, unlike in the previous report (where the spacing medium is air), in our study the emitter and the plasmonic nanostructures are separated by GaAs, whose dielectric and absorption property at the excitation wavelength can change the enhancement mechanism fundamentally.

The results presented in Fig. 2e indicates a very short decay length of the plasmon near-field into the GaAs, which results in enhanced electron-hole generation close to the AuNR-GaAs interface. Based on the observation in Fig. 3b and the tight near-field localization at AuNR-GaAs interface, the net emission enhancement is expected to involve the following distance dependent processes: (i) Förster energy transfer – at short distances, excitation energy transfer from the QDs to the metal surfaces of AuNRs can be the dominant process, which results in reduced emission intensity, (ii) near-field enhanced electron-hole generation inside the InGaAs and efficient carrier capture by the QDs, and (iii) enhanced electron-hole generation at the AuNR-GaAs interface, carrier diffusion through the bulk GaAs and capture by InAs/InGaAs. To extract the length scales of these processes from the experimental enhancement factor ( $EF$ ) presented in Fig. 3b, we propose the following equation.

$$EF = a_0 + a_1 \frac{d^6}{d^6 + d_0^6} + a_2 e^{-d/D_1} + a_3 e^{-d/D_2} \quad (2)$$

where  $a_0$  is an arbitrary constant that displaces the theoretical values so that the experimental and theoretical values are plotted on the same scale. The second term is the Förster formula that describes the efficiency of excitation

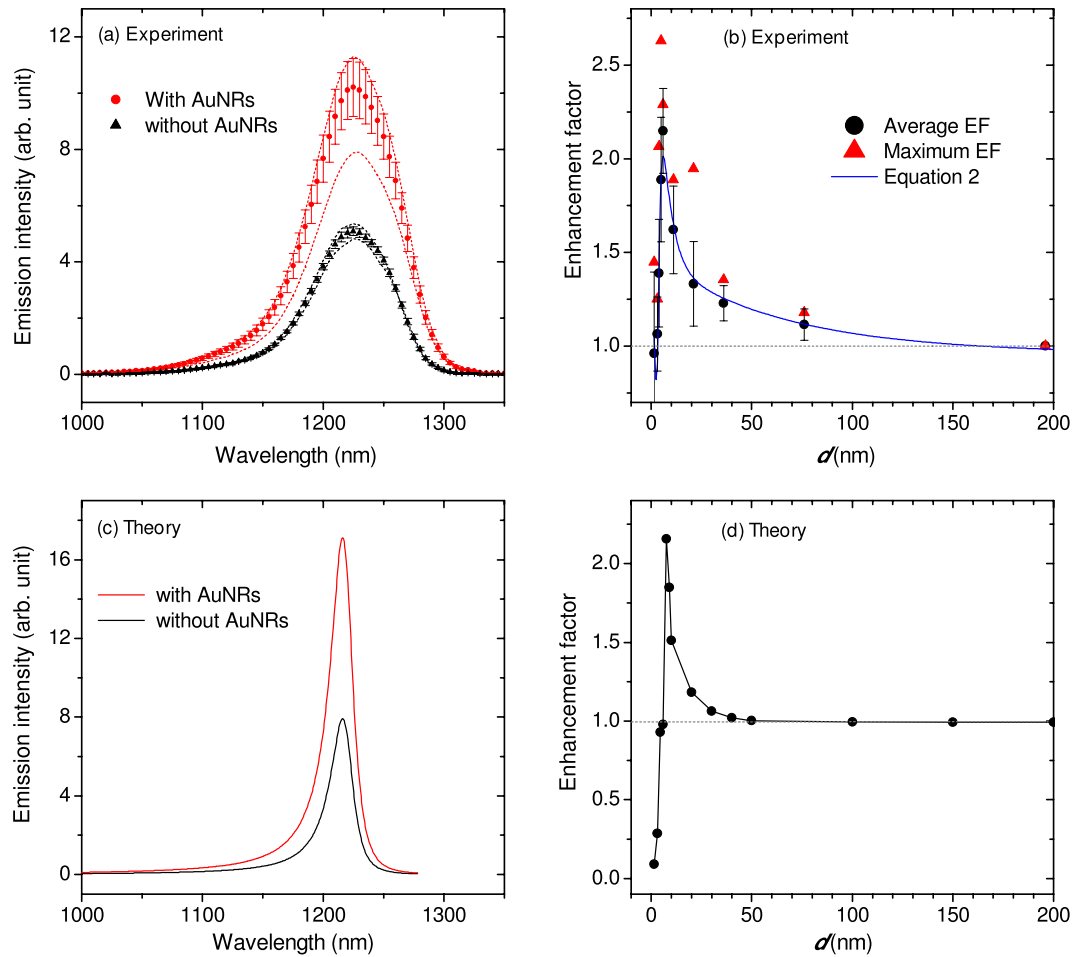


**Figure 3.** Emission enhancement and distance dependence. **(a)** Photoluminescence acquired from different locations where there are no AuNRs (black lines) and where there are AuNRs (red lines) for 6 nm GaAs thickness ( $d$ ) as an example. **(b)** Integrated intensity ratio (enhancement factor) as a function of  $d$ . The error bars on the average data points (black circles) represent one standard deviation. The maximum enhancement factors (red triangles) represent the ratios of the integrated intensities of the highest intensity spectra obtained in the presence and absence of AuNRs for different GaAs thicknesses. The solid blue line is obtained by fitting equation (2) to the average data. **(c)** Calculated emission spectra of InAs QDs for  $d=7.5$  nm in the presence (red line) and absence (black line) of AuNRs. **(d)** Calculated enhancement factor (ratio of emission intensities) plotted as a function of  $d$ .

energy quenching at short distances; the third term accounts for the near-field decay length with distance away from the AuNR-GaAs interface; and the fourth term accounts for the net carrier diffusion length (rate of diffusion in the bulk GaAs and capture by the QD). The coefficients  $a_n$  ( $n=1-3$ ) are amplitude adjustment constants. The parameter values  $d_0=3.9$  nm (Förster radius),  $D_1=4.8$  nm (near-field decay length), and  $D_2=64$  nm (carrier diffusion length) produce a very good fit of Eq. 2 to the average enhancement factor as shown by the blue line in Fig. 3b. It is important to note that the near-field felt by the InGaAs (and hence the electron-hole generation) increases exponentially with decreasing GaAs thickness according to the third term in equation (2). The spacer layer thickness that gives maximum enhancement is determined by the competition between the Förster quenching and the near-field enhancement terms. The physical relevance of the parameters in equation (2) is further justified by reproducing the observed emission spectra theoretically in the absence and presence of the AuNRs, and accounting for the emission enhancement due to direct near-field excitation of the InAs/InGaAs and due to carrier diffusion as discussed next. Further experimental data that confirms the contribution of carrier diffusion is presented.

The net emission rate in the illumination area for all the QDs ( $\tilde{R}$ ) results from the competition between the rates of spontaneous emission ( $R$ ) and excitation energy quenching ( $Q$ ), and can be calculated as  $\tilde{R} = \sigma(R - Q)$ , where  $\sigma$  is the areal density of the quantum dots. The net emission spectrum of the quantum dots in the region where the AuNRs are dispersed can be expressed as

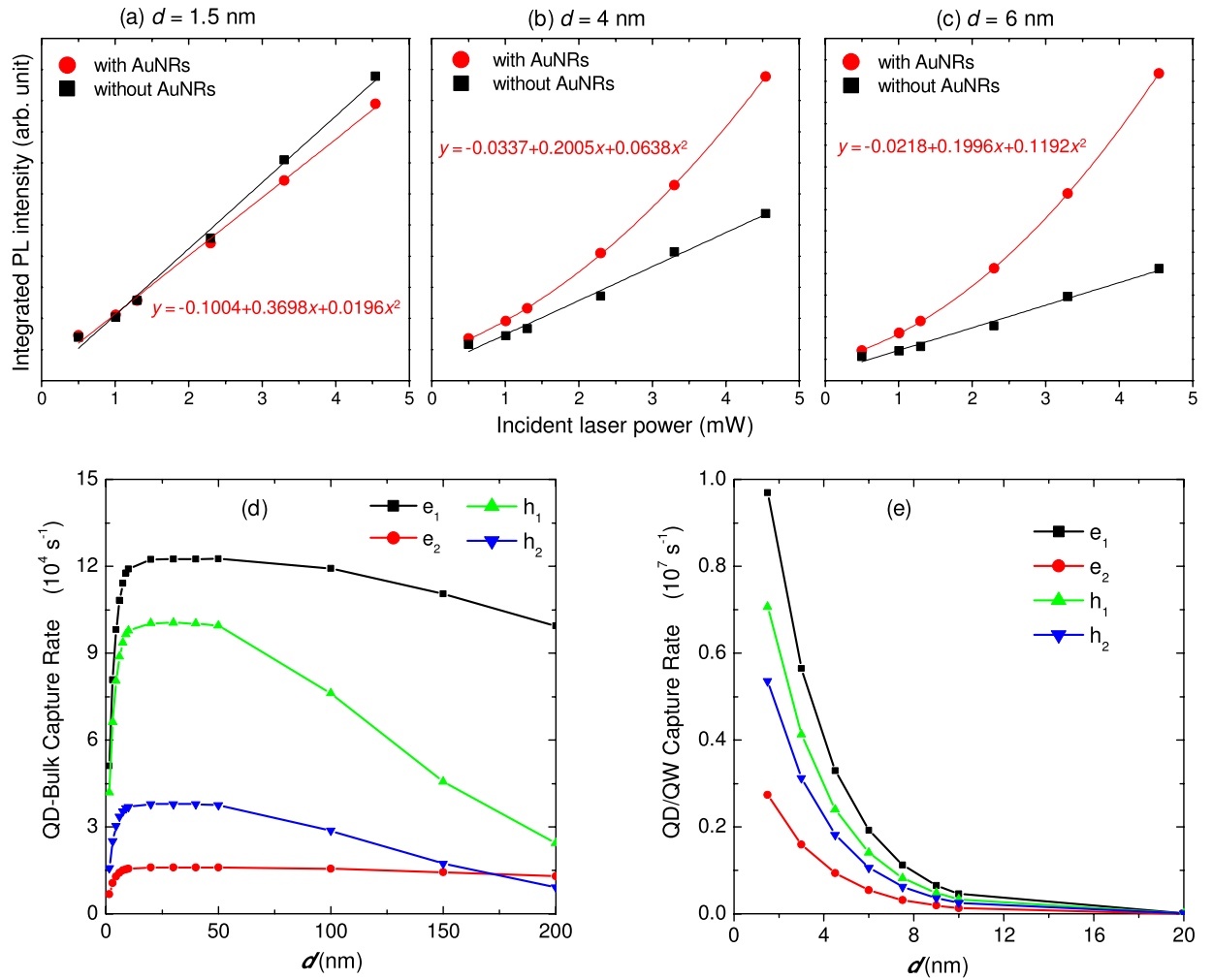


**Figure 4.** Incident laser power dependence and carrier diffusion. PL plotted as a function of laser power for GaAs thicknesses of (a) 1.5 nm, (b) 4 nm, and (c) 6 nm in the presence (red circles) and absence (black squares) of AuNRs. In the absence of the AuNRs, the PL intensity has a linear dependence on the incident power for all GaAs thicknesses. In the presence of the AuNRs, the intensity varies with laser power quadratically, and the degree of nonlinearity increases with the thickness of GaAs as can be seen by comparing the relative values of the coefficients of the linear and the quadratic terms in (a) to (c). (d) Calculated capture rates by two lowest electron (e) and hole (h) energy levels of a QD for electrons and holes generated inside GaAs as a function of  $d$  (GaAs thickness). (e) Calculated distance dependence of capture rates by two lowest QD electron and hole levels generated inside the InGaAs quantum well (the trend shows near-field enhanced electron-hole generation inside InGaAs).

$$\frac{d\tilde{R}(\omega)}{d\omega} = \sigma \left\{ \eta \left[ \frac{dR(\omega)}{d\omega} - \frac{dQ(\omega)}{d\omega} \right] + (1 - \eta) \left[ \frac{dR^0(\omega)}{d\omega} - \frac{dQ^0(\omega)}{d\omega} \right] \right\} \quad (3)$$

where  $\eta$  is the fraction of the area covered by the AuNRs, and  $R^0$  and  $Q^0$  represent the emission and quenching rates, respectively, of the QDs in the absence of the AuNRs. The details of the calculations are provided in the Supplementary Information along with the relevant refs 25, 26. In agreement with the experimental observation, for a certain range of GaAs thickness, the theoretical calculation indicates enhanced emission intensity in the presence of AuNRs as illustrated in Fig. 3c. Plotting the ratio of the peak intensities with respect to the GaAs thickness, the theoretical enhancement factor peaks at  $d = 7.5$  nm as shown in Fig. 3d, which is in good agreement with the experimental result presented in Fig. 3b.

As mentioned above, enhanced electron-hole generation at the AuNR-GaAs interface, carrier diffusion through the bulk GaAs, direct excitation of the InGaAs quantum well and carrier capture by the InAs QDs are suggested as key processes that lead to enhanced photon emission by the QDs. Experimental evidence about the emission enhancement mechanism can be obtained by analyzing the PL intensity dependence on the incident laser power for different thicknesses of GaAs as presented in Fig. 4a–c. For a thickness of 1.5 nm, the intensity is lower in the presence of AuNRs because of the dominance of excitation energy transfer from the QD to the metal

surface that results in reduced QD PL intensity. However, in both cases (in the absence and presence of AuNRs), the PL intensity increases linearly with the incident laser power as shown in Fig. 4a. When the thickness of the GaAs is increased to 4 nm (Fig. 4b) and 6 nm (Fig. 4c), the PL intensity in the presence of the AuNR increases with laser power quadratically, while in the absence of the AuNRs, the trend remains linear for all thicknesses. Fitting a second order polynomial equation to the data, it can be seen that the quadratic character increases with increasing GaAs thickness as can be quantified from the relative values of the coefficients shown on the corresponding figures. The high degree of nonlinear dependence of the PL intensity on laser power for thicker GaAs capping layer clearly indicates that the observed emission enhancement can be attributed to near-field enhanced exciton generation at the AuNR-GaAs interfaces, and the GaAs capping layer is mediating the exciton-plasmon coupling between the AuNR and InAs QDs through carrier diffusion, capture and recombination processes.

The carrier diffusion and capture processes have been theoretically investigated by describing the temporal evolution of the electron-hole occupation number ( $N$ ) of the QD excited states using a dynamical equation and including the plasmon near-field effect on the absorption and emission property of the QDs<sup>25, 27</sup>. For the first excited state of a QD, the temporal evolution of the occupation number ( $N_1$ ) is described as

$$\frac{dN_1^\alpha}{dt} = \frac{\beta_1(\Omega, t)I_0(\Omega, d)}{\hbar\Omega} - \mathcal{R}_1(t) + [1 - N_1^\alpha(t)]\left[\gamma_1^\alpha(t) + \kappa_1^\alpha(t) + \sum_{m=2}^M \frac{N_m^\alpha(t)}{\tau_0}\right] \quad (4)$$

where  $\alpha$  represents electrons or holes,  $\Omega$  is the angular frequency of the incident photons,  $I_0(\Omega, d)$  is the electric field intensity experienced by the QD at thickness  $d$ ,  $\hbar = \frac{h}{2\pi}$  (where  $h$  is Planck's constant),  $\beta$  is the absorption coefficient of the QD,  $\mathcal{R}$  is the rate of spontaneous emission,  $\gamma$  and  $\kappa$  are the rate of capturing carriers from the bulk GaAs and the InGaAs well by the QD, respectively, and  $m = 1, 2, \dots, M$  are quantum numbers of all the bound energy states. The details of the calculation, including, the dynamical equation for the second and higher excited states are provided in the Supplementary Information. The capture rates of the carriers by the QD from the bulk GaAs and InGaAs well are plotted as a function of GaAs thickness in Fig. 4d and e, respectively. As shown in Fig. 4d, the carrier capture rate from the bulk GaAs decreases rapidly for  $d < 10$  nm because for this thickness, the contribution of carrier diffusion is insignificant. The electron-hole (e-h) capture rates remain high up to 50 nm and decreases slowly as the thickness increases further, which is in agreement with the experimentally observed broad carrier diffusion profile in GaAs<sup>28</sup>. In contrast, the direct near-field excitation of InGaAs and the electron and hole capture rates increases exponentially as the GaAs thickness decreases as seen in Fig. 4e. The theoretically calculated result (the trend in Fig. 4e) justifies the physical relevance of the near-field decay length ( $D_1$ ) defined in equation (2). Comparing the scales on the y-axes in Fig. 4d and e, it can be seen that the magnitude of the capture rate from the InGaAs layer is significantly higher than that from the bulk GaAs, suggesting that the apparent emission enhancement trend is mainly determined by the carrier capture rate from the immediate capping layer. However, as shown in Fig. 3d, the decay length of the emission enhancement is longer than that of the carrier capture rate from the InGaAs layer (Fig. 4d), indicating that the net enhancement effect results from the contribution of the capture rates from the InGaAs and GaAs layers. Overall, the trend obtained from the theoretical calculations is in accordance with the parameterized equation (2), and further confirms the importance of the carrier capture rates from the InGaAs and GaAs in determining the observed enhanced photon emission by the InAs QDs. We note that the experimental decay length of the emission enhancement (Fig. 3b) is longer than that of the theoretical decay length (Fig. 3d). Our theoretical modeling neglects the capture of carriers by the InGaAs quantum well from the GaAs layer, which becomes significant when direct excitation of the InGaAs quantum well is not dominant. This could enhance the diffusion current in the GaAs layer and slow down the rapid decay of the theoretical EF presented in Fig. 3d.

## Conclusion

In summary, we have presented the first systematic study of enhanced localized exciton generation, carrier diffusion and recombination experimentally and theoretically. Using GaAs as an active mediator of the interaction between plasmonic nanostructures and quantum dots embedded in an InGaAs capping layer, we have observed a distance dependent emission enhancement that is attributed to enhanced exciton generation at the metal-semiconductor interfacial regions. The experimental observations are reproduced theoretically describing the temporal evolution of charge carriers in the first and second excited states. The length scales of the near-field enhanced exciton generation, the Förster energy transfer that leads to excitation energy transfer to the metal surface at short distances, the electron and hole capture rates by the quantum dots from the bulk GaAs and InGaAs capping layers are determined. The result presented here has a potential for opening new research directions and may lead to improved detection efficiency using the optical properties of near-field enhancement effect of plasmonic nanoparticle.

## Methods

**Fabrication and integration of materials.** The InAs/InGaAs/GaAs semiconductor materials are grown using a molecular beam epitaxy (MBE) reactor on GaAs (001) substrates. First, the GaAs substrate is thermally treated at 630 °C for 20 min to remove the native oxide. The surface is then smoothed by growing a 150 nm thick GaAs at 580 °C. Subsequent growth of InGaAs, InAs and 1.5 nm GaAs at 475 °C results in the InAs QDs confined in the higher band gap InGaAs and GaAs materials. An additional GaAs layer of different thickness is grown (at 580 °C) for studying the distance dependence of the charge carrier generation and diffusion. After removing the excess surfactant from the commercially obtained gold nanorod solution (Nanopartz Inc.) through centrifugation and re-suspension in water, the plasmonic gold nanorods (AuNRs) are dispersed on the GaAs surface by drop-casting and drying the aqueous solution. The AuNRs are applied only on a smaller portion of the sample

so that the emission intensity can be compared by recording the photoluminescence (PL) spectra from the two regions (with and without AuNRs).

**Far-field and near-field optical characterizations.** The photoluminescence (PL) spectra of the InAs/InGaAs/GaAs quantum dot-in-a-well are acquired at room temperature using a conventional lock-in technique and a modulated HeNe laser ( $\lambda = 632.8$  nm, average power of 5 mW) for excitation. Emission from the sample was dispersed by a 0.3 m grating monochromator and detected using a near-infrared detector. The dark-field scattering images of the gold nanorods are obtained using a GX51 Olympus microscope. After the dark-field images are obtained, single particle scattering spectra are recorded by centering the individual gold nanorods in the focus of the collection objective and directing the scattered light into a spectrometer (Isoplan Spectrograph of Princeton Instruments) that is equipped with a thermoelectrically cooled ( $-75^\circ\text{C}$ ) deep depleted CCD camera.

**Topographic and near-field optical characterizations.** The topographic and near-field optical images are obtained using an integrated AFM/Near-field system (Neaspec, GmbH). To avoid distortion of the plasmon mode profiles of the samples, the near-field optical images of the gold nanorods are obtained implementing an orthogonal excitation and detection scheme. That is, the sample is excited with an incident laser ( $\lambda = 632.8$  nm) that is polarized perpendicular to the AFM tip (Arrow-NCPT) and vertically polarized scattered light is selectively detected as described in ref. 20.

**Electromagnetic simulation.** The scattering and near-field experimental results are reproduced in electro-magnetic simulation. The electromagnetic simulation is carried out using finite-difference time domain (FDTD) method, which is implemented using a commercial software package (Lumerical Solutions, Inc.). A total-field scattered field source scheme is used to introduce light energy into the simulation region, where the grid size is 0.5 nm for all x-, y- and z-axes.

**Theory.** Theoretical formalisms that describe the carrier dynamics in the InAs quantum dots and the photon emission enhancement mechanism are presented in the Supplementary Materials.

## References

- Curto, A. G. *et al.* Unidirectional emission of a quantum dot coupled to a nanoantenna. *Science* **329**, 930–933 (2010).
- Fedutik, Y., Temnov, V. V., Schops, O., Woggon, U. & Artemyev, M. V. Exciton-plasmon-photon conversion in plasmonic nanostructures. *Phys. Rev. Lett.* **99**, 136802 (2007).
- Akimov, A. V. *et al.* Generation of single optical plasmons in metallic nanowires coupled to quantum dots. *Nature* **450**, 402–406 (2007).
- Zhang, W., Govorov, A. O. & Bryant, G. W. Semiconductor-metal nanoparticle molecules: hybrid excitons and the nonlinear Fano effect. *Phys. Rev. Lett.* **97**, 146804 (2006).
- Torma, P. & Barnes, W. L. Strong coupling between surface plasmon polaritons and emitters: a review. *Rep. Prog. Phys.* **78**, 013901 (2015).
- Atwater, H. A. & Polman, A. Plasmonics for improved photovoltaic devices. *Nat Mater* **9**, 205–213 (2010).
- Pillai, S. & Green, M. A. Plasmonics for photovoltaic applications. *Sol. Energ. Mat. Sol. Cells* **94**, 1481–1486 (2010).
- Arinze, E. S., Qiu, B. T., Nyirjesy, G. & Thon, S. M. Plasmonic nanoparticle enhancement of solution-processed solar cells: practical limits and opportunities. *ACS Photonics* **3**, 158–173 (2016).
- Chang, C.-C. *et al.* A surface plasmon enhanced infrared photodetector based on InAs quantum dots. *Nano Lett.* **10**, 1704–1709 (2010).
- Miao, J. S. *et al.* Surface plasmon-enhanced photodetection in few layer MoS<sub>2</sub> phototransistors with Au nanostructure arrays. *Small* **11**, 2392–2398 (2015).
- Zhou, N. *et al.* Plasmon-enhanced light harvesting: applications in enhanced photocatalysis, photodynamic therapy and photovoltaics. *RSC Adv.* **5**, 29076–29097 (2015).
- Fei, J. B. & Li, J. B. Controlled preparation of porous TiO<sub>2</sub>-Ag nanostructures through supramolecular assembly for plasmon-enhanced photocatalysis. *Adv. Mater.* **27**, 314–319 (2015).
- Pompa, P. P. *et al.* Metal-enhanced fluorescence of colloidal nanocrystals with nanoscale control. *Nat. Nanotechnol.* **1**, 126–130 (2006).
- Anger, P., Bharadwaj, P. & Novotny, L. Enhancement and quenching of single-molecule fluorescence. *Phys. Rev. Lett.* **96**, 113002 (2006).
- Liu, R. Y., Vasinajindakaw, P., Gu, G. R., Vaillancourt, J. & Lu, X. J. Optimizing light absorption in quantum dot infrared photodetectors by tuning surface confinement of surface plasmonic waves. *J. Phys. D-Appl. Phys.* **46**, 015102 (2013).
- Ebbesen, T. W., Lezec, H. J., Ghaemi, H. F., Thio, T. & Wolff, P. A. Extraordinary optical transmission through sub-wavelength hole arrays. *Nature* **391**, 667–669 (1998).
- Jayavel, P. *et al.* Control of optical polarization anisotropy in edge emitting luminescence of InAs/GaAs self-assembled quantum dots. *Appl. Phys. Lett.* **84**, 1820–1822 (2004).
- Ridha, P. *et al.* Polarization dependence study of electroluminescence and absorption from InAs/GaAs columnar quantum dots. *Appl. Phys. Lett.* **91**, 191123 (2007).
- Yasuoka, N. *et al.* Demonstration of transverse-magnetic dominant gain in quantum dot semiconductor optical amplifiers. *Appl. Phys. Lett.* **92**, 101108 (2008).
- Habteyes, T. G. Direct near-field observation of orientation-dependent optical response of gold nanorods. *J. Phys. Chem. C* **118**, 9119–9127 (2014).
- Chen, H. *et al.* Observation of the Fano resonance in gold nanorods supported on high-dielectric-constant substrates. *ACS Nano* **5**, 6754–6763 (2011).
- Wu, Y. P. & Nordlander, P. Finite-difference time-domain modeling of the optical properties of nanoparticles near dielectric substrates. *J. Phys. Chem. C* **114**, 7302–7307 (2010).
- Kiesow, K. I., Dhuey, S. & Habteyes, T. G. Mapping near-field localization in plasmonic optical nanoantennas with 10 nm spatial resolution. *Appl. Phys. Lett.* **105**, 053105 (2014).
- Habteyes, T. G., Dhuey, S., Kiesow, K. I. & Vold, A. Probe-sample optical interaction: size and wavelength dependence in localized plasmon near-field imaging. *Opt. Express* **21**, 21607 (2013).
- Huang, D. & Alsing, P. M. Many-body effects on optical carrier cooling in intrinsic semiconductors at low lattice temperatures. *Phys. Rev. B* **78**, 035206 (2008).

26. Andrews, D. L. In *Tutorials in Complex Photonic Media* (eds Mikhail A., Noginov, Graeme, Dewar, Martin W., McCall & Nikolay I., Zheludev) 439–478 (Spie Press, 2009).
27. Huang, D. H. *et al.* Controlling quantum-dot light absorption and emission by a surface-plasmon field. *Opt. Express* **22**, 27576–27605 (2014).
28. Bieker, S., Kiessling, T., Ossau, W. & Molenkamp, L. W. Correct determination of low-temperature free-exciton diffusion profiles in GaAs. *Phys. Rev. B* **92**, 121201 (2015).

## Acknowledgements

This research has been supported by the U.S. Air Force Office of Scientific Research, Award No. FA9550-15-1-0305, and the Air Force Research Laboratory, Award No. FA9453-15-1-0078. The project was initiated while T.G.H. was participating in the Air Force Summer Faculty Fellowship in Kirtland Air Force Base under the supervision of Dr. David Cardimona.

## Author Contributions

T.G.H. conceived and designed the experiments and prepared the manuscript; S.H. performed the gold nanorod sample preparation, photoluminescence measurement and electromagnetic simulation and other characterizations; S.A. and G.B. performed the fabrication of the semiconductors; S.H. and B.K. carried out the dark-field scattering measurement; and D.H. calculated the quantum dot emission spectra and the rates of charge carrier diffusion.

## Additional Information

**Supplementary information** accompanies this paper at doi:[10.1038/s41598-017-00964-5](https://doi.org/10.1038/s41598-017-00964-5)

**Competing Interests:** The authors declare that they have no competing interests.

**Publisher's note:** Springer Nature remains neutral with regard to jurisdictional claims in published maps and institutional affiliations.



**Open Access** This article is licensed under a Creative Commons Attribution 4.0 International License, which permits use, sharing, adaptation, distribution and reproduction in any medium or format, as long as you give appropriate credit to the original author(s) and the source, provide a link to the Creative Commons license, and indicate if changes were made. The images or other third party material in this article are included in the article's Creative Commons license, unless indicated otherwise in a credit line to the material. If material is not included in the article's Creative Commons license and your intended use is not permitted by statutory regulation or exceeds the permitted use, you will need to obtain permission directly from the copyright holder. To view a copy of this license, visit <http://creativecommons.org/licenses/by/4.0/>.

© The Author(s) 2017

## List of Abbreviations

|       |   |
|-------|---|
| LA    | laser ablation                                      |
| LIBS  | laser-induced breakdown spectroscopy                |
| MALDI | matrix-assisted laser desorption and ionization     |
| CW    | continuous wave                                     |
| SERS  | surface enhanced Raman scattering                   |
| ANSOM | apertureless near-field scanning optical microscope |
| MB    | methylene blue                                      |
| AFM   | atomic force microscope                             |
| BS    | beam splitter,                                      |
| P     | polarizer   |
| HWP   | half waveplate                                      |
| QWP   | half waveplate                                      |
| QCL   | quantum cascade laser                               |
| PMMA  | poly(methyl methacrylate)                           |
| AuNR  | gold nanorod  |
| AuNS  | gold nanosphere                                     |
| CCD   | charge coupled device                               |
| NA    | numerical aperture                                  |

## **DISTRIBUTION LIST**

|  |       |
|--|-------|
| DTIC/OCP<br>8725 John J. Kingman Rd, Suite 0944 Ft<br>Belvoir, VA 22060-6218 | 1 cy  |
| AFRL/RVIL<br>Kirtland AFB, NM 87117-5776                                     | 2 cys |
| Official Record Copy<br>AFRL/RVBYC/Dr. Christopher Annesley                  | 1 cy  |